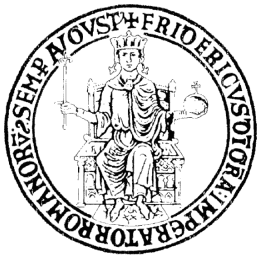

University of Studies of Naples "Federico II"

DEPARTMENT OF AEROSPACE ENGINEERING

Ph.D. In Aerospace Engineering

Experimental and numerical studies on low velocity impacts detection and damage identification in metal and composite structures using ultrasonic waves propagation (Lamb waves)

The Chairman of the Ph.D. School:

Prof. Antonio Moccia

Research Supervisor:

Prof. Fabrizio Ricci

Candidate:

Eng. Simone Tancredi

November 2011

Introduction.

Structural Health Monitoring (SHM) has become, in recent years, one of the most important area of investigation, not only in the Aeronautical and Aerospace environments, but in a wide area of engineering fields, such as the Civil one [5] [27].

Quality, Reliability and Safety are the main features that every artifact or service shall carry not only because of the norms by the Aviation Authority, but also for making it the most attractive as possible for the buyers. SHM is the answer to the new globalized market that asks, more than any other thing: "Optimization"!

Optimization does not only mean maximizing the performances of a manufact with the lowest price as possible at the time of purchase, but also taking into account the whole operational life. The maintenance of a modern civilian aircraft absorbs about 20-25% of its entire operational cost, thus playing a definitely crucial part. SHM aims to improve dramatically the parameters of Quality, Reliability and Safety, thus also reducing the maintenance costs. This can be achieved through a different design process that reduces the required number of scheduled both light and heavy maintenances. Flight schedules basically depend on the efficiency of maintenance since the productivity of an aircraft depends on the time of employment. From this arises the need of reducing maintenance times as much as possible, of course without compromising or rather increasing safety, since aviation has always aimed in achieving high standards of safety, far beyond those of other types of transport.

The major causes of aircraft accidents are due to:

1. Human error
2. Adverse weather conditions
3. Acts of terrorism
4. Structural failure / inadequate maintenance

Accidents due to structural failure or inadequacy of the maintenance are relatively low compared to other causes, nevertheless the task of the aviation industry is to focus on the elements of danger and try to minimize them all. In the case of aircraft accidents, the manufacturing industries are the parts that are most affected by economic impact because, in addition to any compensation, suffer a boycott by the airline companies.

Regarding the operational life, an aircraft structure is typically subject to the action of time-varying loads. These, in the case of defects or damage in materials, can induce an intensification of stresses within the structure, thus producing cracks (barely visible damage) due to fatigue. In turn, cracks, propagating over time, weaken the structure and could even lead to rupture. During the history of aviation, various design criteria have been developed to ensure the resistance of the structure when it is subject to multiple load cycles, that we can refer, essentially, to two philosophies:

- Safe Life;
- Damage Tolerance

The first one is designed to ensure, for a given design life, the resistance to workloads without the generation of fatigue cracks, whereas the second, contemplating the eventual presence of damage in some points of the structure, continuously monitors and checks the propagation path of the cracks. The Damage Tolerance design philosophy allows us to subdivide the structures in:

- ‘Fail-Safe’ Structures (made up with redundant elements, the rupture of one of them has no catastrophic effect since the load is distributed on the intact ones);
- ‘Slow Crack Growth’ Structures (made up with elements that present a long period for crack propagation).

Regarding the typologies of damage, the structure of an aircraft is subject to the following main sources:

1. Environmental deterioration
2. Accidental damage
3. Fatigue damage

Environmental deterioration (typically corrosion) of a mechanical component refers to the structural deterioration caused by the chemical interaction with the weathering and in general with the surrounding environment. In the field of aircraft constructions, for reasons of weight, the structures must have high efficiency, thus the presence of corrosion is a problem of considerable importance.
An accidental damage is the physical damage of a mechanical component caused by contact, by impact with an object or even by a human error attributable to manufacturer, to flight operations or to a wrong way of proceeding during maintenance. Inspection intervals within which an accidental damage can be detected are related to the type of damage and likely to the consequences caused by it. Therefore, we cannot establish thresholds as damage occurs randomly, and in some cases they are found during a routine inspection.
Fatigue damage refer to the physical deterioration of the material due to fatigue stresses caused by repeated or even randomly varying in time loads; the stresses induced in the aircraft’s structure during flight, takeoff and landing operations are all critical load conditions. A fatigue damage typically begins with a small fracture, initially very difficult to detect with common methods: liquid penetrant inspection, X-rays, etc.; as the crack increases in dimensions because of load cycles, the effects of stress concentration becomes higher, and the speed of propagation of the crack also becomes even greater. Through this mechanism the cross section area of the structure decreases and the stresses increase until they reach the collapse level. For several reasons composites are some of the most critical type of materials with respect to fatigue.
In recent years composite materials have been increasingly introduced in both the Aeronautical and Aerospace environments thus becoming the most important materials to be adapted for aviation since the use of aluminum in the 1920s. They are materials that are combinations of two or more organic or inorganic components: one material serves as a "matrix", which is the material that holds everything together, while the other material serves as a reinforcement, in the form of fibers embedded in the matrix. The most common matrix materials are "thermosetting" materials such as epoxy, bismaleimide, or polyimide; whereas the reinforcing materials can be glass fiber, boron fiber, carbon fiber, or other more exotic mixtures. Unfortunately composites, for reasons inherent in their internal structure, suffer much more than any other conventional metallic material of problems related to damage. Typical damage for composites are matrix cracking, delaminations, fiber fractures, interfacial debondings, etc., and all these kind of damage, especially the ones involving fatigue problems, are very critical. The most problematic aspect of damage in composites is that they can be produced by events involving very small values of energies; as an example delaminations might occur, at interfaces between different

oriented adjacent plies, as a result of impacts with external objects involving energies of the order of some Joules. Typically these low velocity impacts produce so small damage within the material that they can't be detected through a simple visual inspection. New methods of investigation have been thus developed, in the last decades, especially for composites, such as Structural Health Monitoring techniques involving Lamb waves [5] [7] [16].

Lamb waves are elastic guided waves that travel in thin-wall structures along directions parallel to plate's middle plane, at frequencies of the order of kHz, or even MHz. A feature that makes Lamb waves so interesting and advantageous for damage detection is that they present wavelengths of the order of centimeters or even millimeters (depending on frequency) which makes them able to interact with obstacles, e.g. through thickness damage in plates, of the same order of magnitude; low energy impacts on composites might induce damage of such dimensions, so hardly identified with other techniques. Moreover Lamb waves can be both excited and sensed through the use of small, lightweight and inexpensive transducers such as Piezoelectric Wafer Active Sensors (PWAS). PWAS transducers can be produced in different geometries and dimensions so that they can be adapted for the various cases, furthermore they can be directly bonded onto the structure under inspection thus becoming one piece with it.

A tool capable to detect small damage inside structures from their very early stage of development, hence when damage dimensions are of the order of millimeters, could eventually lead to a different design philosophy in which the Safety Factors could be significantly lowered.

1. LAMB WAVES

1.1 Theory elements.

Lamb waves are elastic waves, propagating in solid plates, whose particle motion lies in the plane that contains the direction of wave propagation and the direction perpendicular to the plate. In 1917 the English mathematician Sir. Horace Lamb published his classic analysis and description of acoustic waves of this type [1], thus these waves are called Lamb waves. An infinite medium supports just two wave modes traveling at unique velocities, namely pressure and shear waves, whereas plates support two infinite sets of Lamb waves modes whose properties depend on various parameters such as plate's elastic properties and thickness, frequency, etc., so their properties turn out to be quite complex. A comprehensive mathematical description of the problem of Lamb waves propagation in solids can be found in various publications by Viktorov [2] (1967), Achenbach [3] (1973), Rose [4] (1999), Giurgiutiu [5] (2008). We are not going here to present the whole mathematical formulation of the problem of Lamb waves propagation in plates, but only the logical path that brings to the relations between frequency and velocity of propagation for the various modes.
Lamb waves can exist in two basic types: symmetric and antisymmetric (Fig. 1.1), and, for each of these types, various modes appear as solutions of the Rayleigh-Lamb equations <1.8>.

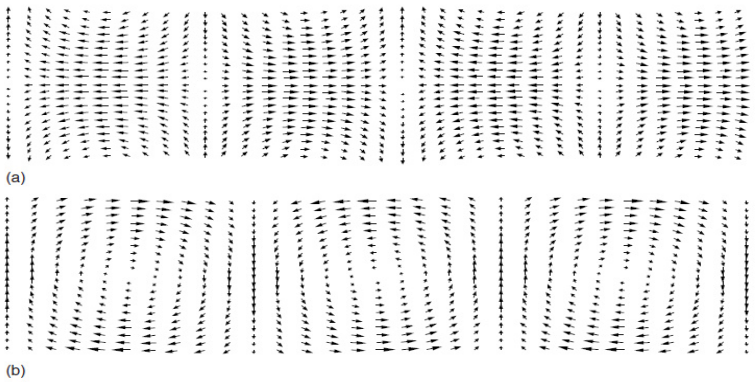

Fig. 1.1 – Zero order symmetric and antisymmetric Lamb waves modes.

In general, elastic waves in solid materials are guided by the boundaries of the media in which they propagate. An approach to guided wave propagation, widely used in physical acoustics, is to seek sinusoidal solutions to the wave equation for linear elastic waves subject to boundary conditions representing the structural geometry: this is a classic eigenvalue problem.

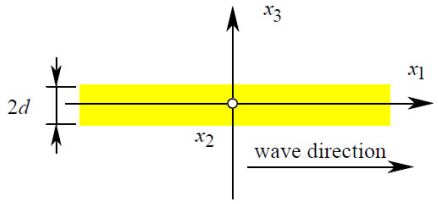

Let's consider the three dimensional wave equation describing the propagation of elastic waves in an isotropic solid media without external forces:

$$\langle 1.1 \rangle \quad (\lambda+\mu)\underline{\nabla}(\underline{\nabla}\cdot\underline{u})+\mu\nabla^2\underline{u}=\rho\underline{\ddot{u}}$$

with $\underline{\boldsymbol{u}}$ displacements vector, $\boldsymbol{\lambda}$ and $\boldsymbol{\mu}$ Lamé constants, and $\boldsymbol{\rho}$ density of the isotropic material. Through the Helmoltz theorem the vector $\underline{\boldsymbol{u}}$ can be decomposed using two potentials, one scalar $\boldsymbol{\varphi}$ and one vectorial $\underline{\boldsymbol{\psi}}$:

$$\langle 1.2 \rangle \quad \underline{u}=\underline{\nabla}\varphi+\underline{\nabla}\times\underline{\psi}$$

By combining <1.1> and <1.2> we obtain the two equations:

$$\langle 1.3 \rangle \quad \begin{cases} c_P^2\nabla^2\varphi=\ddot{\varphi} \\ c_S\nabla^2\underline{\psi}=\underline{\ddot{\psi}} \end{cases} \quad ; \quad c_P=\sqrt{\frac{\lambda+2\mu}{\rho}} \ , \ c_S=\sqrt{\frac{\mu}{\rho}}$$

with $\boldsymbol{c_P}$ and $\boldsymbol{c_S}$ respectively pressure and shear waves speeds.
For harmonic-wave propagation in the $\boldsymbol{x_1}$ direction, $\boldsymbol{e^{i(\xi x_1-\omega t)}}$, the equations <1.3> become:

$$<1.4> \quad \begin{cases} \dfrac{d^2\phi}{dx_3^2}+p^2\phi=0 \\ \dfrac{d^2\psi}{dx_3^2}+q^2\psi=0 \end{cases} ; p^2=\frac{\omega^2}{c_P^2}-\xi^2; \ q^2=\frac{\omega^2}{c_S^2}-\xi^2; \ \xi=\frac{\omega}{c}$$

with $\boldsymbol{\omega}$ circular frequency and $\boldsymbol{\xi}$ wave number, having general solution:

$$\langle 1.5 \rangle \quad \begin{cases} \phi=A_1\sin(px_3)+A_2\cos(px_3) \\ \psi=B_1\sin(qx_3)+B_2\cos(qx_3) \end{cases}$$

From <1.4> and <1.5>, by assuming zero displacement in the x_2 direction ($u_2 = 0$), the general form of components of the displacement vector can be derived, grouped into symmetric and antisymmetric components:

$$\langle 1.6 \rangle \quad \begin{cases} u_1 = \left(A_2 i\xi \cos\left(px_3\right) + B_1 q \cos\left(qx_3\right)\right) + \left(A_1 i\xi \cos\left(px_3\right) - B_2 q \cos\left(qx_3\right)\right) \\ u_3 = -\left(A_2 p \cos\left(px_3\right) + B_1 i\xi \cos\left(qx_3\right)\right) + \left(A_1 p \cos\left(px_3\right) - B_2 i\xi \cos\left(qx_3\right)\right) \end{cases}$$

We then can write the stresses in terms of both the scalar and vectorial potentials, and, by applying the conditions of free surfaces on the plate's top and bottom, we obtain the system of equations:

$$\langle 1.7 \rangle \begin{cases} \tau_{33}\big|_{x_3=d} = \tau_{33}\left(\varphi, \underline{\psi}\right)\Big|_{x_3=d} = 0 \\ \tau_{33}\big|_{x_3=-d} = \tau_{33}\left(\varphi, \underline{\psi}\right)\Big|_{x_3=-d} = 0 \\ \tau_{13}\big|_{x_3=d} = \tau_{13}\left(\varphi, \underline{\psi}\right)\Big|_{x_3=d} = 0 \\ \tau_{13}\big|_{x_3=-d} = \tau_{13}\left(\varphi, \underline{\psi}\right)\Big|_{x_3=-d} = 0 \end{cases}$$

By requiring the system <1.7> to have non-trivial solutions (determinant equal to zero), we obtain two transcendental implicit equations, one for symmetric modes and one for antisymmetric ones, called Rayleigh-Lamb equations (d is the plate half-thickness, c_{ph} is the wave speed, $\xi = \omega / c_{ph}$ is the wave number):

$$\langle 1.8 \rangle \quad \begin{cases} \dfrac{\tanh\left(pd\right)}{\tanh\left(qd\right)} = -\dfrac{\left(\xi^2 - q^2\right)^2}{4\xi^2 pq} & \text{symmetric modes (S)} \\ \dfrac{\tanh\left(pd\right)}{\tanh\left(qd\right)} = -\dfrac{4\xi^2 pq}{\left(\xi^2 - q^2\right)^2} & \text{antisymmetric modes (A)} \end{cases}$$

The solutions of the two equations <1.8> represent the phase velocities c_{ph} of the various Lamb waves modes: these curves do not exist in a closed form, so numerical algorithms are needed in this case. Each one of the two Rayleigh-Lamb equations presents a number of solution curves defining more than one relation between wave number and frequency, or even wave velocity and frequency: several orders are present for both symmetric and antisymmetric modes.

By considering the velocity of Lamb waves packets traveling in the plate, we introduce the group velocity $\boldsymbol{c_g}$ which is linked to phase velocity through the relation:

$$\langle 1.9 \rangle \quad c_g = \frac{\partial \omega}{\partial c_{ph}} \quad \text{or even} \quad c_g = \frac{c_{ph}}{1 - \frac{\omega}{c_{ph}} \frac{\partial c_{ph}}{\partial \omega}}$$

In Fig 1.2 the frequency-velocity dispersion curves (from <1.8> and <1.9>) are presented.

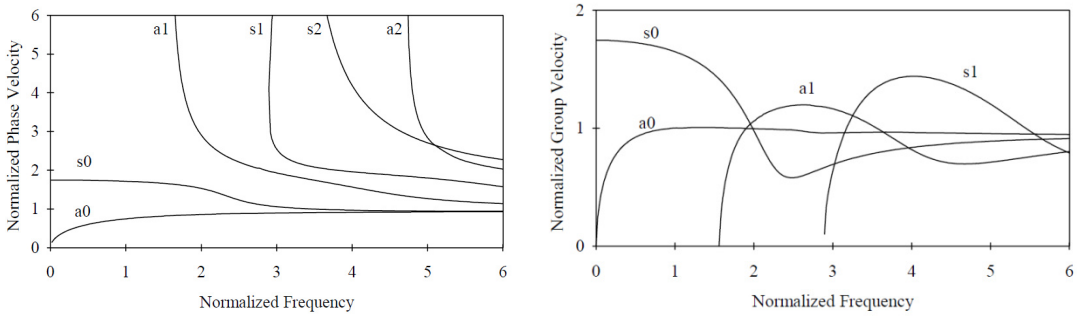

Fig. 1.2 - Dispersion curves for an aluminum plate, lowest order solutions. Normalizing velocity: shear velocity $\boldsymbol{c_S}$; normalizing frequency: $\boldsymbol{\xi_S \cdot d}$, with $\boldsymbol{\xi_S = \omega / c_S}$.

In Fig. 1.2 we can see the strong dependence of the wave speeds with frequency, showing the typical dispersive behavior. The zero order modes are present at all frequencies, while the higher orders appear at certain cut-off frequencies. Since, by definition, Lamb waves have no particle motion in the $\boldsymbol{x_2}$ direction, the displacement vector $\underline{\boldsymbol{u}}$ lies inside the plane defined by axes $\boldsymbol{x_1}$ and $\boldsymbol{x_3}$. Motion in the $\boldsymbol{x_2}$ direction is found, for plates, in the so-called SH or shear-horizontal wave modes. For these kind of waves particles have no motion in the $\boldsymbol{x_1}$ or $\boldsymbol{x_3}$ directions, and they are thus complementary to the Lamb waves modes.
Dispersion curves, the graphs that show relationships between wave velocity (or wave number) and frequency in dispersive systems, can be presented in various forms. The form that gives the greatest insight into the underlying physics has $\boldsymbol{\omega}$ (angular frequency) on the y-axis and $\boldsymbol{\xi}$ (wave number) on the x-axis. The form used by Viktorov, that brought Lamb waves into practical use, has wave velocity on the y-axis and $\boldsymbol{d/\lambda}$, the thickness/wavelength ratio, on the x-axis. The most practical form of all has wave velocity on the y-axis and $\boldsymbol{f \cdot d}$, the frequency-thickness product, on the x-axis.
For values of frequency that tends to zero the problem can be simplified and there are formulas for the velocities:

For the S_0 mode: $\langle 1.10 \rangle \quad \lim_{\omega \to 0} \left(c_{ph} \right) = \sqrt{\frac{E}{\rho \left(1 - \nu^2 \right)}} \quad ; \quad c_g = c_{ph}$

For the A_0 mode: $\langle 1.11 \rangle$ $\lim_{\omega \to 0}\left(c_{ph}\right) = \sqrt[4]{\dfrac{E}{3\rho\left(1-\nu^2\right)}}$; $c_g = 2c_{ph}$

with $\boldsymbol{E}$ and $\boldsymbol{\nu}$ Young modulus and Poisson's ratio of the material; $\boldsymbol{\rho}$ is the density.
The phenomenon of velocity dispersion leads to a rich variety of experimentally observable waveforms when acoustic waves propagate in plates. The zero order symmetric (S_0) and antisymmetric (A_0) modes are relatively easy, in thin plates, to generate and recognize so they are the most involved in nondestructive testing.

1.2 Lamb waves tuning.

In recent years an increasing number of investigators use, in their Structural Health Monitoring (SHM) analysis with Lamb waves, Piezoelectric Wafer Active Sensors (PWAS) for ultrasonic waves generation and sensing [6] [5] [7] [20]. The successful experiments performed in nondestructive tests, combined with their minimal invasiveness and inexpensiveness have positioned PWAS as an enabling technology for the development and implementation of active SHM systems. PWAS transducers (Fig. 1.3a) can be surface mounted or inserted inside layered materials such as composites, thus becoming one piece with the structure where they are bonded on. On the contrary conventional ultrasonic transducers are expensive and present more difficulties of using (Fig. 1.3b).

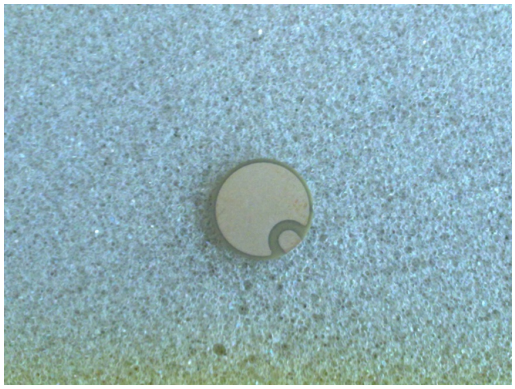

Fig. 1.3a - PWAS disk transducer.

Fig 1.3b - Conventional ultrasonic transducers

Although the considerable advantages in using PWAS, there are some difficulties to be faced with. Their characteristic behavior is strongly non linear and involve coupling of electrical and mechanical variables; plus PWAS transducers form a unique body with the structure they are bonded on, thus greatly complicating the study. The interaction between

piezoelectric transducers and structures is crucial and a number of studies have been conducted [9], [10].
The constitutive equations of a piezoelectric material are in the form:

$$\langle 1.12 \rangle \quad \begin{cases} S_{ij} = s^{E}_{ijkl} T_{kl} + d_{kij} E_k \\ D_j = d_{jkl} T_{kl} + \varepsilon^{T}_{jk} E_k \end{cases}$$

with $\boldsymbol{S_{ij}}$ mechanical strain, $\boldsymbol{T_{kl}}$ mechanical stress, $\boldsymbol{E_k}$ electrical field, $\boldsymbol{D_j}$ electrical displacement, $\boldsymbol{s^{E}_{ijkl}}$ mechanical compliance of the material measured at zero electric field ($\boldsymbol{E}$ = 0), $\boldsymbol{\varepsilon^{T}_{jk}}$ dielectric permittivity measured at zero mechanical stress ($\boldsymbol{T}$ = 0), $\boldsymbol{d_{jkl}}$ piezoelectric coupling effect parameter. These equations show that a voltage applied to two points of a piezoelectric material, which produces an electric field, induces a strain in the material, i.e. a contraction or an expansion. Thus an oscillatory voltage produces and oscillatory mechanical behavior. Vice versa an oscillatory expansion and contraction produces an oscillatory electric field, and so an alternating voltage at PWAS terminals. The solution of the dynamic response of a PWAS transducer is greatly complicated by the boundary conditions, since when it is bonded onto a structure it becomes one piece with it: a coupling is present.
Some of the most important results on tuned Lamb waves excitation and detection with PWAS have been achieved by Giurgiutiu (University of South Carolina, Columbia SC, USA) and presented in various publications [8] [5]. The central concept of these studies is the characterization of the stresses, especially shear, induced by PWAS transducers inside the plate during their operating modes. By combining the solutions of Lamb waves governing equations for displacements <1.6> and the boundary conditions, i.e. the stresses induced by a PWAS on the surface where it is bonded on, both the plate displacements and strains can be derived as functions of various parameters including frequency. Basically there is a strong dependence of Lamb waves amplitudes with frequency (for both symmetric and antisymmetric modes), thus making frequency the most important factor for Lamb waves tuning with PWAS. We can so excite the various Lamb waves modes, i.e. S_0 and A_0, simply by tuning the frequency, very easy parameter to control.
The function linking waves amplitude with frequency presents some maxima and minima respectively corresponding to the two conditions:

$$\langle 1.13 \rangle \quad \begin{cases} l_a = (2n-1)\dfrac{\lambda(f)}{2} & \text{maximum amplitude} \\ l_a = 2n\dfrac{\lambda(f)}{2} & \text{minumum amplitude} \end{cases}$$

l_a is the PWAS dimension, λ is the wavelength function of frequency, n is a natural number including zero. Since different Lamb wave modes propagate with different speeds, the various conditions of maxima and minima happen at different frequencies for the different modes. A typical analytical graph linking amplitudes of S_0 and A_0 modes with frequency is shown in Fig. 1.4.

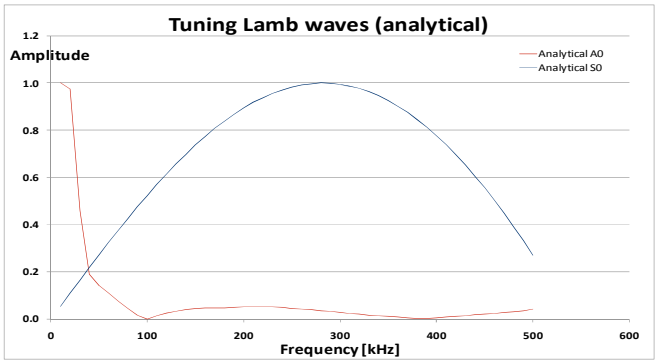

Fig 1.4 - Lamb waves response for an aluminum plate of thickness 1mm, using a PWAS disk of diameter 10mm; the amplitudes are normalized.

As we can see in Fig. 1.4, Lamb waves tuning can be achieved by controlling frequency. In detail, from theory, for an aluminum plate of thickness 1mm using PWAS disks of diameter 10mm, by exciting frequencies around 30 kHz only A_0 mode will be present since it presents the maximum amplitude ('sweet spot'), whereas S_0 presents a minimum. On the contrary by exciting frequencies around 290 kHz almost only S_0 mode will be present.
The analytical solution of the Lamb waves amplitudes, in Fig. 1.4, has been confirmed by experimental acquisitions performed on an aluminum plate of 1mm thickness, using two 10mm diameter PWAS disks (PI Ceramic, PIC-255): #1 used as actuator and #4, at a distance of 20cm, as sensor (Fig 1.5b); the signals to PWAS were generated through a signal generator HP/Agilent 33120A, while the acquisitions were performed by using an oscilloscope Agilent InfiniiVision DSO7104A (Fig. 1.5a).

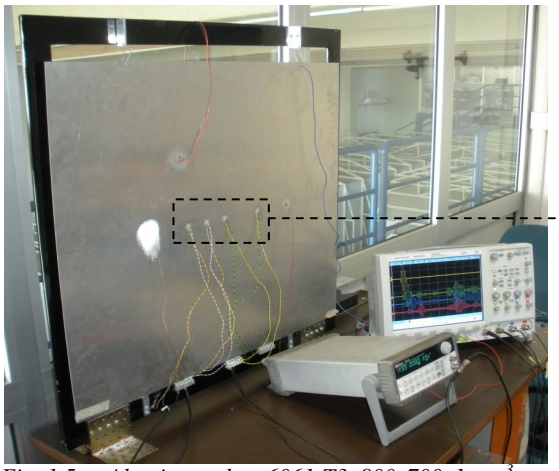

Fig. 1.5a - Aluminum plate 6061-T3, 800x700x1 mm[3]

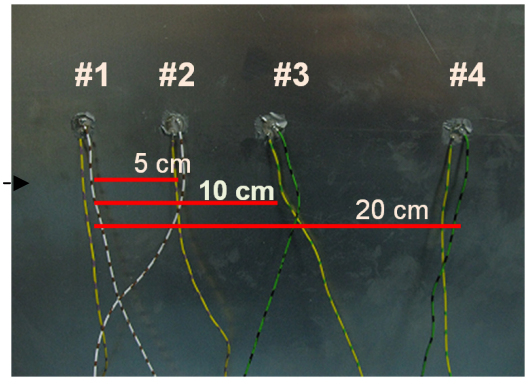

Fig. 1.5b - PWAS disks, PI-Ceramic PIC-255, 10mmx0.2mm

As excitation a 4.5 sine cycles curve with a Hanning window was used, in order to obtain a narrow-band bell curve in the frequency domain (Fig. 1.6). Narrow-band excitations are needed in order to limit the problem of dispersiveness of Lamb waves, strongly dependent on frequency.

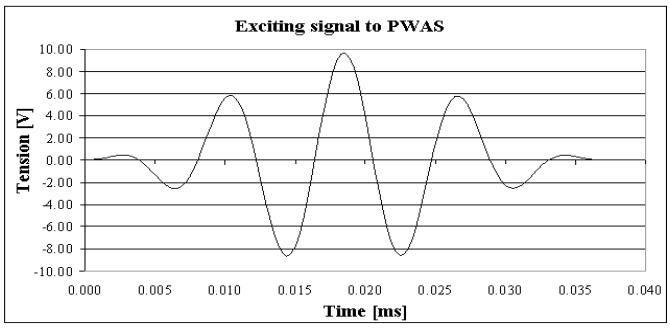

Fig 1.6a – Excitation curve, 4.5 sine cycles with Hanning window

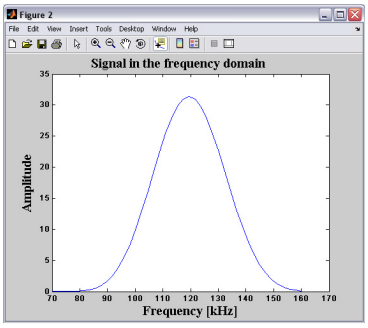

Fig. 1.6b – Curve in frequency domain

The test involved frequencies from 10 to 110 kHz, step 10 kHz, for A_0 mode, while from 10 to 500 kHz, step 10 kHz, for S_0. Amplitudes of both A_0 and S_0 were evaluated from output signals registered through PWAS #4, positioned at 20mm from source (#1). The reason we did not analyze A_0 mode beyond 110 kHz was due to the presence of S_0 reflections from plate edges, overlapping the first incoming A_0 waves packet at sensor's location. In Fig. 1.7 some experimental acquisitions, for various frequencies, and relative tuning curves are presented.

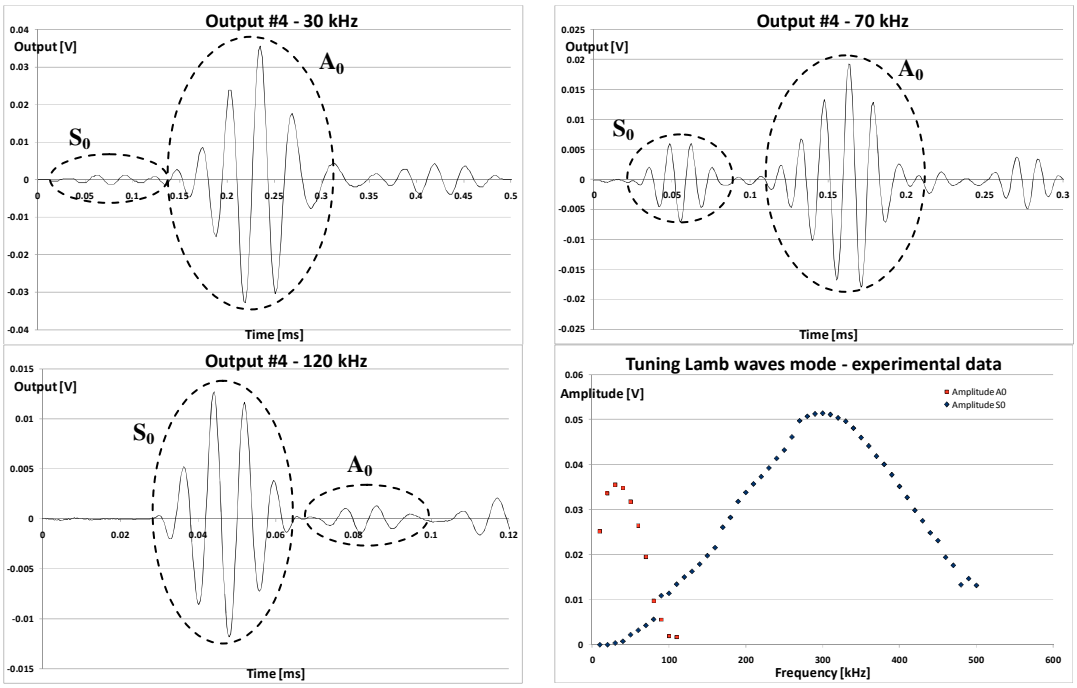

Fig 1.7 – Lamb waves responses at a distance of 20cm from actuator, for various frequencies.

Lamb waves modes can be easily recognized from speeds of propagation, and hence from the arrival times. For an aluminum plate, of thickness 1mm, the group velocity of S_0 substantially remains constant for a range of frequencies between zero and 500 kHz and is about 5300m/s. A_0 are more dispersive in the low frequency range and, for frequencies of 30, 70 and 120 kHz the group velocities are, respectively, 1040, 1500 and 1900 m/s. Hence S_0, in Fig. 1.7, are represented by the first wave packet arriving at the PWAS location; after S_0, A_0 are present and then reflections from edges.

The comparison between the experiment and theory is presented in Fig. 1.8: a general good agreement can be seen. There is only a little frequency shift on maximum amplitudes both for A_0 and S_0, probably due to the bonding layer between PWAS and aluminum panel, not considered in the analytical solution involving ideal bonding.

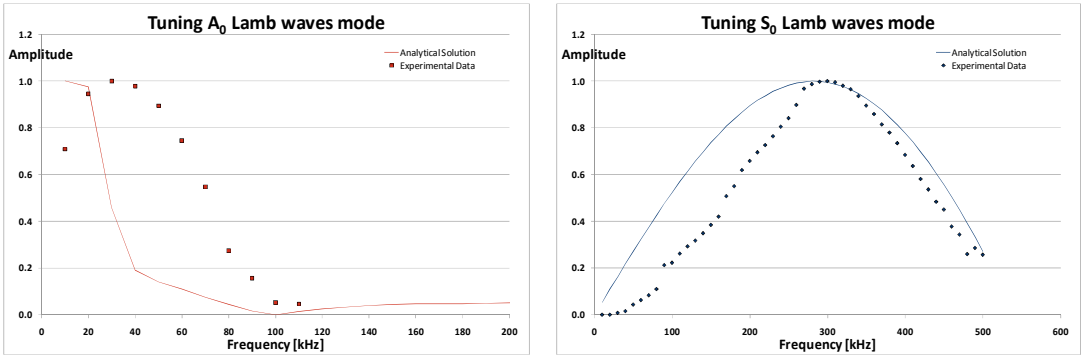

Fig. 1.8 – Comparison between experiments and theory for Lamb waves amplitudes

1.3 Lamb waves in experiments and in FEM.

1.3.1 Introduction

The solution for the problem of Lamb waves propagation in thin structures is, in recent years, available and various numerical codes have been written. Professors Ajit Mal (University of California, Los Angeles, USA) and Sauvik Banerjee (Indian Institute of Technology Bombay, India) developed various codes, using various plate theories, that give the displacements or stress/strains at various locations on both isotropic and composite plates, for a given excitation force curve [11] [12] [13] [14]. Generally these codes assume that the plate is infinite and that there are no obstacles on the propagation path of the guided waves. Unfortunately for complicated geometries that involve interaction of Lamb waves with holes, cracks, rivets, or even other structural elements bonded on the plate, the problem is hardly modeled using a numerical code that involves only equations: a FEM code is needed in this case.

FEM codes are able to solve the equations of structural dynamics in both frequency and time domain for a given geometry, as complex as it is. The real structure is modeled as a set of geometrical elements that can have various shapes (1D, 2D or 3D elements), and the solution function is approximated as a combination of a limited number of so called "shape functions". Definitely the differential equations system is substituted with an ordinary differential equations system or with an algebraic equations system.

Lamb waves propagation is an unsteady problem that can be directly simulated in time domain, using FEM, through the use of a direct transient analysis. Since Lamb waves speeds are typically of the order of thousands of meters per second, and the structures dimensions are of the order of meters, the time of propagation is typically of the order of milliseconds: very fast dynamics! This allows us to use explicit FEM codes that give very accurate solutions for short time dynamics, with relatively small solution times (order of hours).

The very challenging problem, dealing with FEM codes, is the modeling of Lamb waves actuators and sensors, that typically are piezoelectric transducers. The interaction of these devices with the structure is a non linear problem that involves electromechanical coupling effects. FEM codes that are able to simulate the physics of piezoelectric materials are unfortunately implicit and this means that the time for calculation of the dynamic response strongly increases, achieving the order of days or even weeks.

A greatly advantageous different approach, presented in this work, is the substitution of the piezoelectric devices, in the FEM model, with the dynamic action they typically exert on the structure when operating as actuators. Regarding sensor operating mode they have been modeled by taking into account only geometrical variables in FEM, substantially neglecting the coupling of their electrical properties with the mechanical ones. Of course this induced an error on the solution but, as it will be clear from comparisons with experimental acquisitions, this error affected the solution in a minor way.

1.3.2 Test on an aluminum plate (experiment).

In our first analyses of Lamb waves modeling we considered a 6061-T6 aluminum plate having dimensions 800x700x1 mm^3, and piezoelectric disks (PWAS) of diameter 10mm and thickness 0.2mm from PI Ceramic (PIC-255). Four PWAS transducers were bonded on the plate for experimental acquisitions (Fig. 1.9): the actuator (#1) was positioned close to plate center, while other three PWAS, operating as sensors, were placed on the horizontal axis of the aluminum plate, at distances from actuator 5cm (#2), 10cm (#3) and 20cm (#4). As exciting signal we considered a 4.5 sine cycles curve with Hanning window, and a number of experimental acquisitions were performed for frequencies from 10 to 500 kHz, step 10 kHz: both A_0 and S_0 modes were excited.

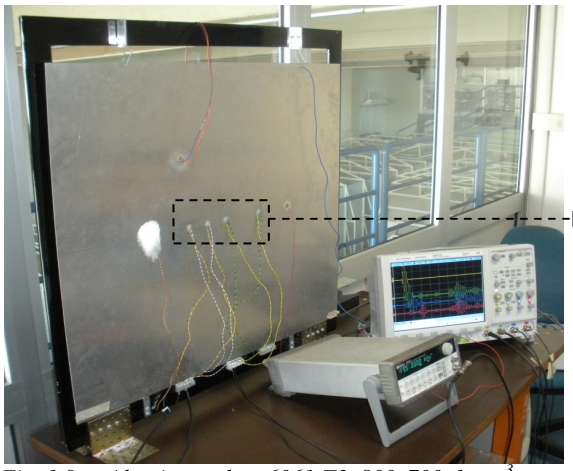

Fig. 1.9a - Aluminum plate 6061-T3, 800x700x1 mm^3

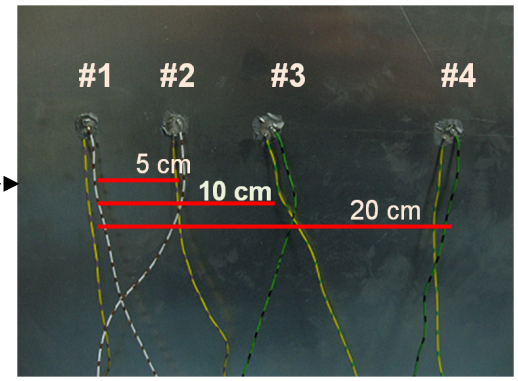

Fig. 1.9b - PWAS disks, PI-Ceramic PIC-255

In Fig. 1.10 and 1.11 experimental acquisitions for frequencies 70 and 200 kHz are shown.

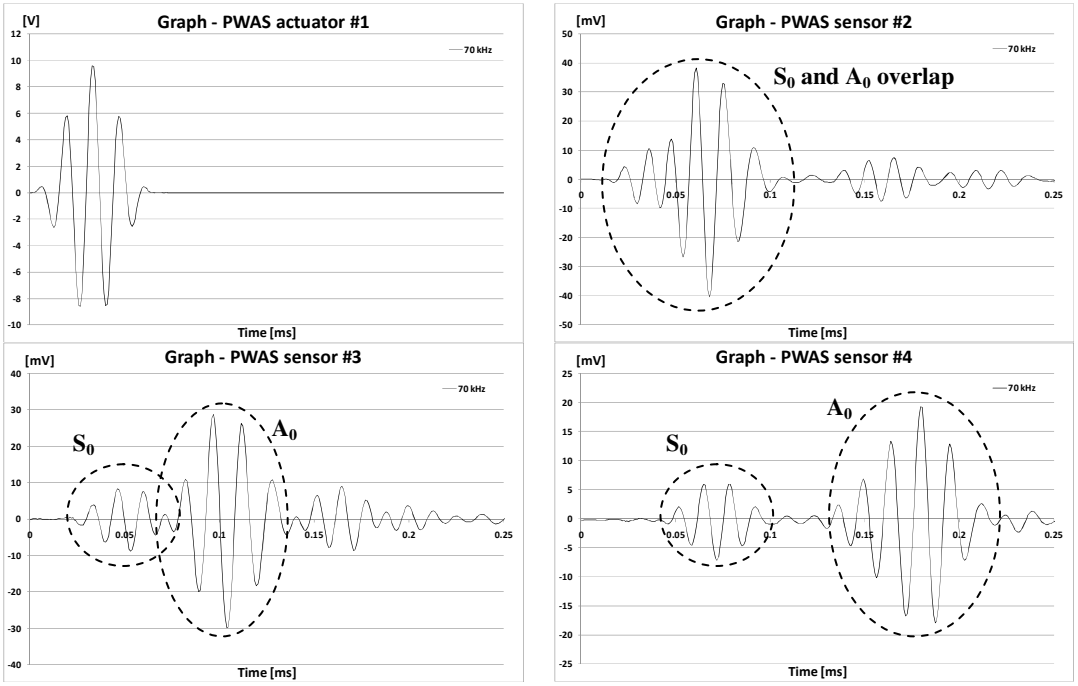

Fig. 1.10 – Experimental acquisitions of Lamb waves for frequency 70kHz

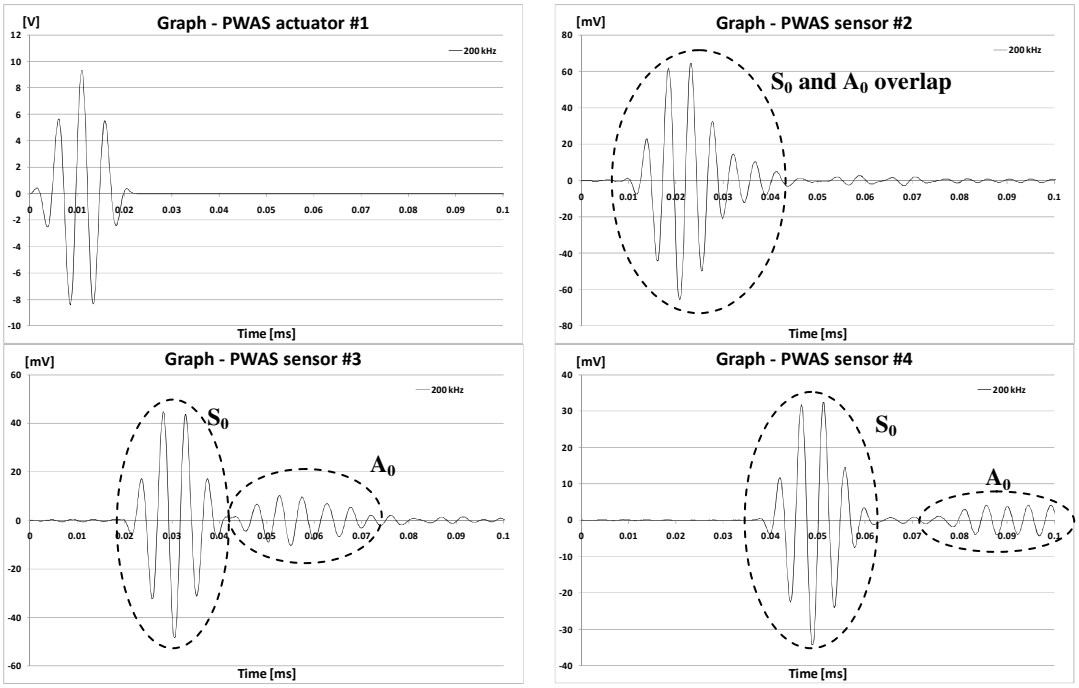

Fig. 1.11 – Experimental acquisitions of Lamb waves for frequency 200kHz

As shown in Fig. 1.10 and 1.11, for both frequencies of 70 and 200 kHz, A_0 and S_0 modes overlap on PWAS #2. At frequency 70kHz, S_0 velocities were found to be, from theory

(solutions of <1.8> and <1.9>), $c_g^{S_0} = c_{ph}^{S_0}$ = 5350 m/s, while for A_0: $c_g^{A_0}$ = 1539 m/s and $c_{ph}^{S_0}$ = 808 m/s; for frequency 200 kHz, S_0 present $c_g^{S_0}$ = 5342 m/s and $c_{ph}^{S_0}$ = 5348 m/s, while A_0: $c_g^{A_0}$ = 2285 m/s and $c_{ph}^{A_0}$ = 1295 m/s (Vallen Dispersion - Vallen Systeme GmbH, Germany).

An important property of Lamb waves, linked also to their dispersiveness, is that: if, in the range of frequency content of the exciting signal, phase and group velocities are very close, $c_{ph} \approx c_g$, with group velocity almost constant, then the shape of the Lamb waves packet, for a single mode, remains substantially the same during propagation. This is the case of S_0 mode, visible in both Fig. 1.10 and 1.11: S_0 signals received at the various sensors locations are very similar to the exciting signal. On the contrary A_0 mode presents different phase and group velocities and, for frequencies up to 2 MHz, it is highly dispersive (Fig. 1.2). This induces a variation of the waveform as far as the wave packet travels through the plate (i.e. in the space domain) as indicated in Fig. 1.10 and 1.11.

1.3.3 Test on an aluminum plate (numerical simulations).

After performing experimental acquisitions we considered both the 'exact' analytical (Mal and Lih code [13]) and FEM solutions of the same experiment.

In a first step a point load was used as excitation, lying on the top surface of the plate and acting along the horizontal X-axis. This was a preliminary analysis that did not take into account the actual PWAS behavior, acting as a radial excitation, as it will be showed later on. As excitation we used the same curve as in Lamb waves tuning experiments: a 4.5 sine cycles curve with Hanning window (Fig. 1.6), with maximum amplitude 1 Newton and frequency 200 kHz, thus generating both A_0 and S_0 waves. Then we considered, as output from both 'exact' and FEM codes, the in-plane X component of displacement, evaluated at sensor's location: PWAS #3 at 100mm distance from source (#1).

The aluminum plate, dimensions 800x700x1 mm^3, was modeled, in FEM, with 3D bricks having dimensions 0.5x0.5x0.5 mm^3, thus obtaining, for the entire model, 1600x1400x2 elements for a total of 4.48 million elements. Element dimension was derived from wavelength, by modeling at least ten elements per wavelength. Since both S_0 and A_0 waves were present, two wavelengths were considered, λ^{A_0} and λ^{S_0}:

$\lambda^{A_0} = c_{ph}^{A_0} / f$ = (1295m/s) / (200kHz) = 6.48mm

$\lambda^{S_0} = c_{ph}^{S_0} / f$ = (5348m/s) / (200kHz) = 26.74mm

thus obtaining, by using a 0.5mm mesh dimension along X and Y axes, 13 elements for the A_0 wavelength and 53 for the S_0 one.

Regarding number of elements along the thickness, FEM analyses were performed, for comparing the results, using 5, 4, 3, 2 and 1 elements: minor differences in the solutions were found from 5 to 2 elements, therefore 2 elements through the thickness were used. The time for calculating the 'exact' solution was about 1 day with a 4 cores 2.4GHz computer, whereas the time for solution using FEM was about 1 hour and 20 minutes with a 8 cores 2GHz computer.

In Fig. 1.12 the comparison of the three curves, relative to an experimental acquisition, 'exact' solution and FEM solution, at PWAS #3 location, are shown (normalized curves).

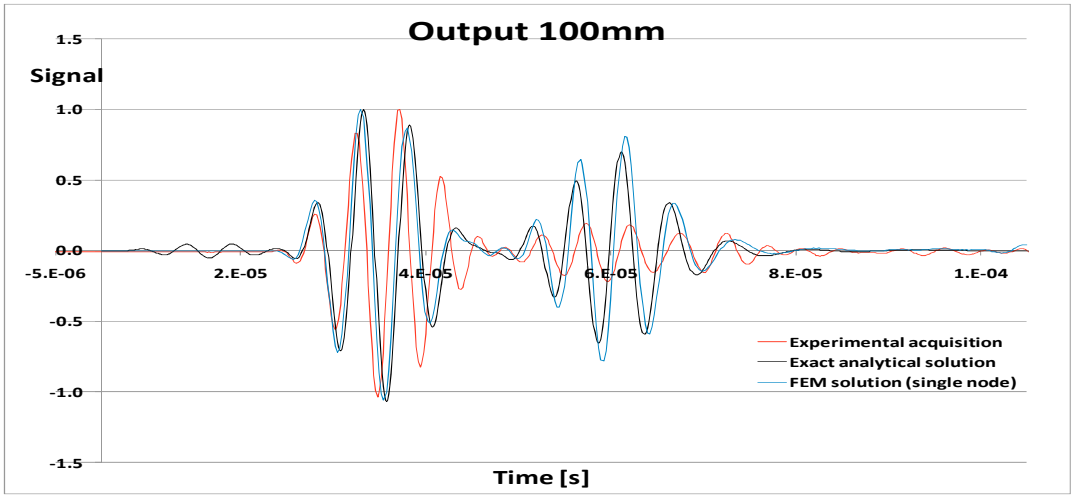

Fig. 1.12 – Comparison between the experiment, the 'exact' solution and the FEM solutions, for Lamb waves propagation in an aluminum plate

As we can see from Fig. 1.12, both 'exact' and FEM solutions showed the same trend, although these curves did not overlap the experimental acquisition. This was to be expected because of the too simple modeling of excitation load on the plate. Nevertheless we can notice that S_0 wave is quite well modeled, whereas A_0 presents different amplitudes and a little shift between the numerical solutions and the experimental acquisition.
Therefore in the second step we considered a different, more structured, load configuration: a circular set of 8 in-plane loads located in correspondence of PWAS actuator's ideal ends (Fig. 1.13a).

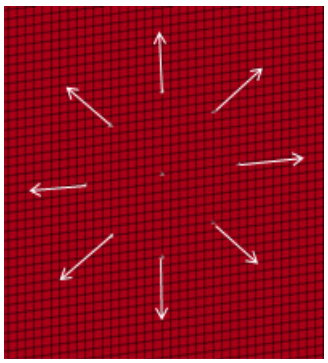

Fig. 1.13a – modeling of PWAS actuators

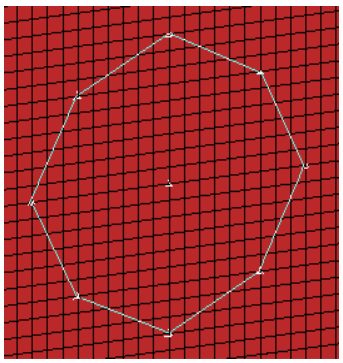

Fig. 1.13b – modeling of PWAS sensors

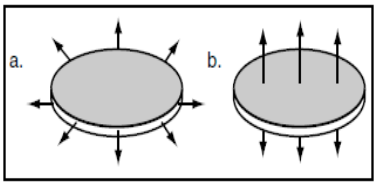

Fig. 1.13c – deformation modes of a PWAS disk

Regarding the output, in FEM, we modeled the PWAS sensor disks using a zero-order technique: the PWAS outputs (Volts) were obtained by considering the time variation of

the area of octagons, approximating PWAS disks, with vertices coincident with mesh nodes (Fig. 1.13b). Actually we linked the time history of this variation to the output voltage of PWAS through the electro-mechanical parameters provided by the PWAS manufacturer. For better understanding the way we modeled PWAS disks let's consider their working principle during the passive operating mode (sensors). A piezoelectric material is a material whose main feature is the generation of an electric field when a stress/strain field is present: also the opposite occurs. This means that when a piezoelectric material is deformed we can measure a potential difference (Volts) between two electrodes soldered onto two of its faces. By considering a piezoelectric disk we can figure out two modes of deformation: an in-plane mode and an out-of-plane mode (Fig 1.13c). The in-plane deformation can be defined through the variation of the diameter ($\boldsymbol{d_{PWAS}}$) of the disk, while the out-of-plane deformation through the variation of its thickness ($\boldsymbol{th}$). If we consider the potential difference measured between the upper and lower surfaces of the piezoelectric disk, we have that this voltage is directly linked to the geometrical deformations of the disk through the relation:

$$\langle 1.14\rangle \; \Delta V_{U-L} = \left[\Delta V_{in-plane}\right] + \left[\Delta V_{out-of-plane}\right] = \left[\frac{\Delta d_{PWAS}\cdot th}{\mathrm{d}_{31}\cdot d_{PWAS}}\right] + \left[\frac{\Delta th}{\mathrm{d}_{33}}\right]$$

with $\mathbf{d_{31}}$ and $\mathbf{d_{33}}$ piezoelectric constants defining the ratio between deformation and tension. Since the in-plane deformation of a PWAS is mostly elliptical rather than circular we can define the surface variation instead of the diameter variation, for then linking this variable to voltage (the diameter variation $\overline{\Delta d}_{PWAS}$ is averaged along two perpendicular axes):

$$A = \pi\left(\frac{d_{PWAS}}{2}\right)^2 = \frac{\pi d_{PWAS}^2}{4} \Rightarrow \Delta A \simeq \frac{\pi d_{PWAS}\cdot \overline{\Delta d}_{PWAS}}{2} \Rightarrow \frac{\Delta A}{A} \simeq \frac{\pi d_{PWAS}\cdot \overline{\Delta d}_{PWAS}}{2}\cdot\frac{4}{\pi d_{PWAS}^2} \Rightarrow \langle 1.15\rangle \frac{\Delta A}{A} \simeq 2\frac{\overline{\Delta d}_{PWAS}}{d_{PWAS}}$$

If we assume that only the in-plane deformation is present we obtain:

$$\Delta V \simeq \frac{\overline{\Delta d}_{PWAS}\cdot th}{\mathrm{d}_{31}\cdot d_{PWAS}} = \left(2\frac{\overline{\Delta d}_{PWAS}}{d_{PWAS}}\right)\frac{th}{2\cdot \mathrm{d}_{31}} \simeq \frac{\Delta A}{A}\cdot\frac{th}{2\cdot \mathrm{d}_{31}} \Rightarrow \langle 1.16\rangle \; \Delta V \simeq \frac{th}{2\cdot \mathrm{d}_{31}}\cdot\frac{\Delta A}{A}$$

This last relation <1.16> allows us to estimate, with a very good quality, the output voltage from PWAS using the time histories of the node displacements at the sensors locations:

$$\langle 1.16\rangle \; \Delta V(t_i) \simeq \frac{th}{2\cdot \mathrm{d}_{31}}\cdot\frac{\Delta A(t_i)}{A_0}$$

The great advantage of this solution is that we can link the outputs from the piezoelectric sensors, in the FEM code, to the time histories of only geometrical variables, without the need to use coupled electro-mechanical elements: the output voltage from a PWAS is simply the result of a post-processing phase of the FEM solution. This is of great advantage since the direct transient analysis, for fast dynamics, can be solved through the use of explicit FEM codes: explicit FEM codes are much faster than implicit ones when there is the need of having small time-steps in the solution. This was our case since we had the need to have solutions for problems presenting time durations of the order of few milliseconds, with time-steps for solution of the order of microseconds, or even less.
Electro-mechanical coupling is a non-linear problem and unfortunately only implicit codes are available for this cases. The disadvantage of using an implicit code for Lamb waves simulations, involving coupled electro-mechanical elements, is that the time for solution, even using a very fast computer, easily achieves the order of weeks! Moreover the problem in this case can't be easily solved through the use of parallel processing. On the contrary explicit algorithms are easily suitable for massive parallel processing.
The result of this new modeling, for PWAS #3, is shown in Fig 1.14.

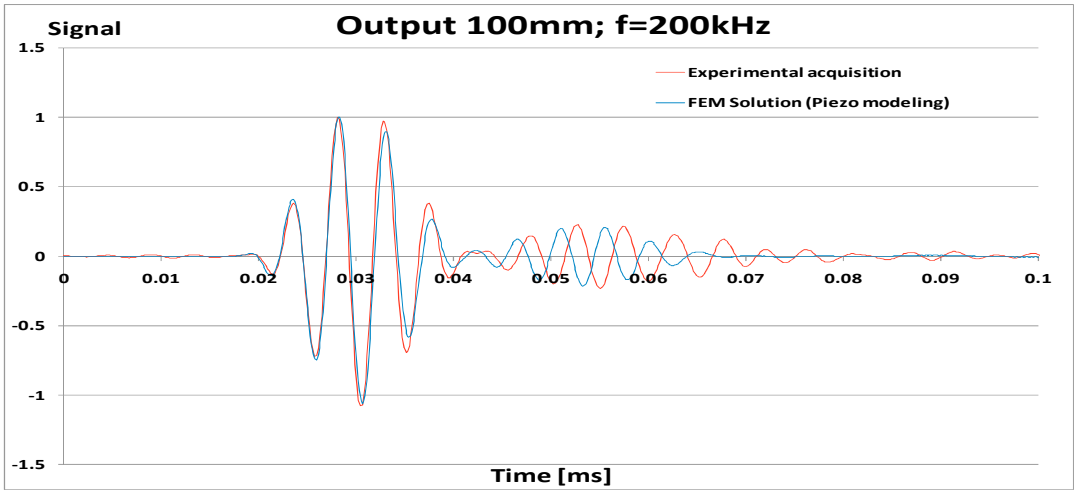

Fig. 1.14 – Comparison between experiment and FEM solution, for Lamb waves propagation in an aluminum plate

As shown in Fig. 1.14, both A_0 and S_0 waves were well modeled both in amplitude and shape, though a little shift still remained for A_0 waves. From Fig. 1.15 to 1.17 the contour plots of the stresses are shown, and from Fig. 1.18 to 1.20 the comparisons for frequencies 70, 200 and 320 kHz, for all PWAS sensors, are presented.

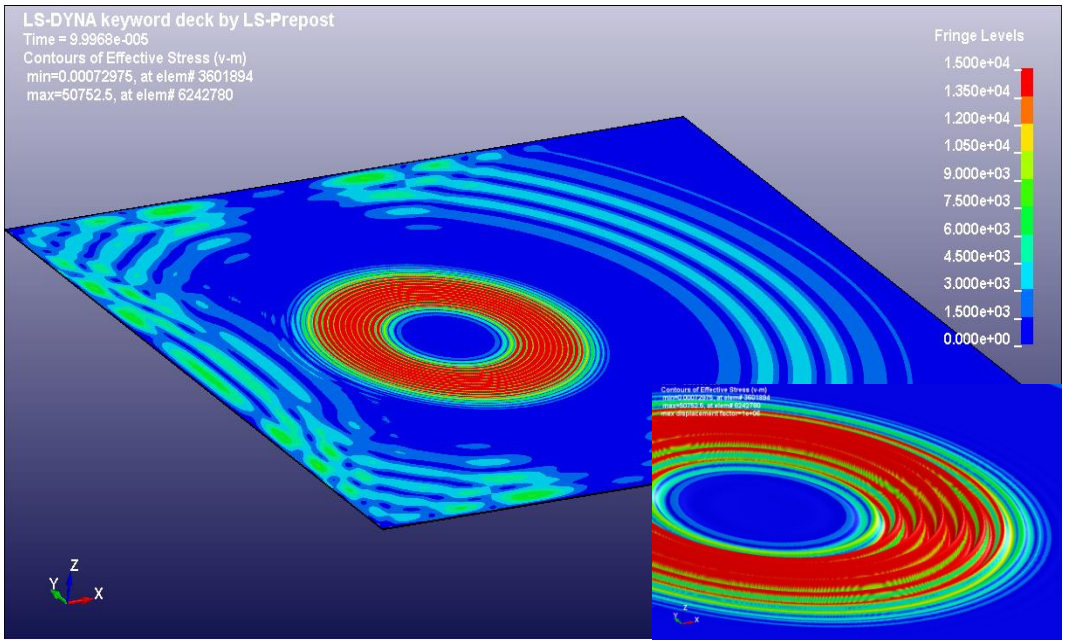

Fig. 1.15 – Contour plot of Von Mises stresses, for the aluminum plate, at 70kHz

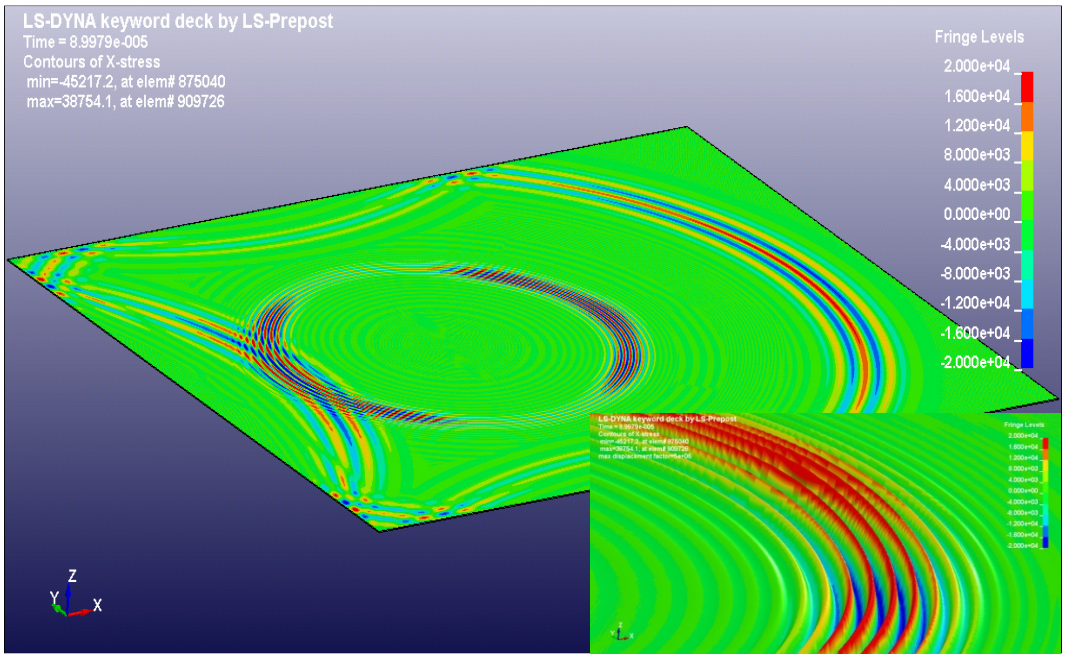

Fig. 1.16 – Contour plot of X stresses, for the aluminum plate, at 200kHz

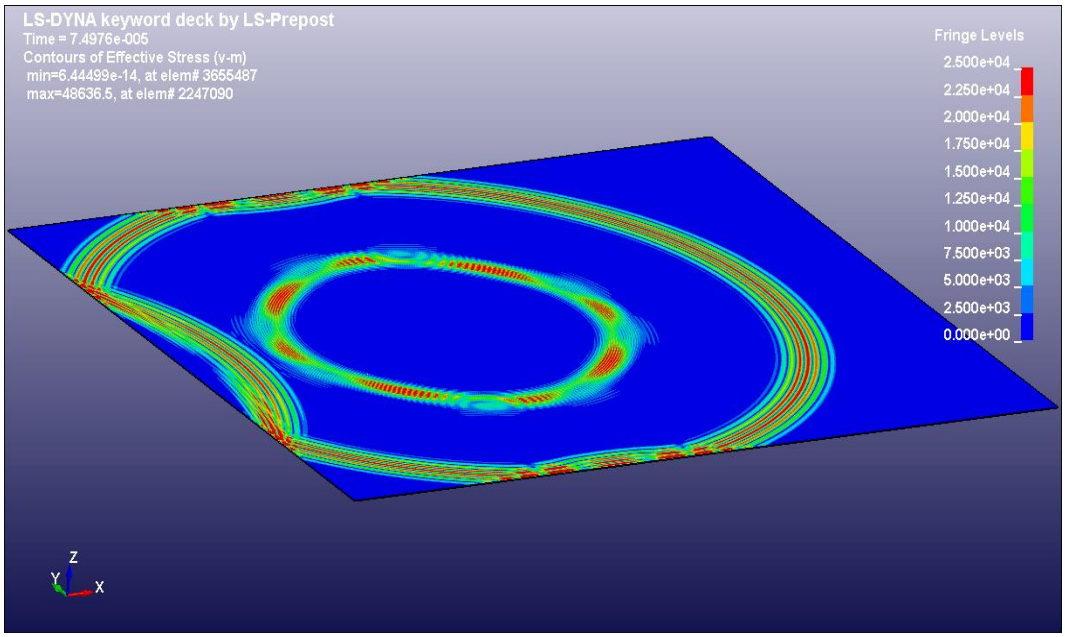

Fig. 1.17 – Contour plot of Von Mises stresses, for the aluminum plate, at 320kHz

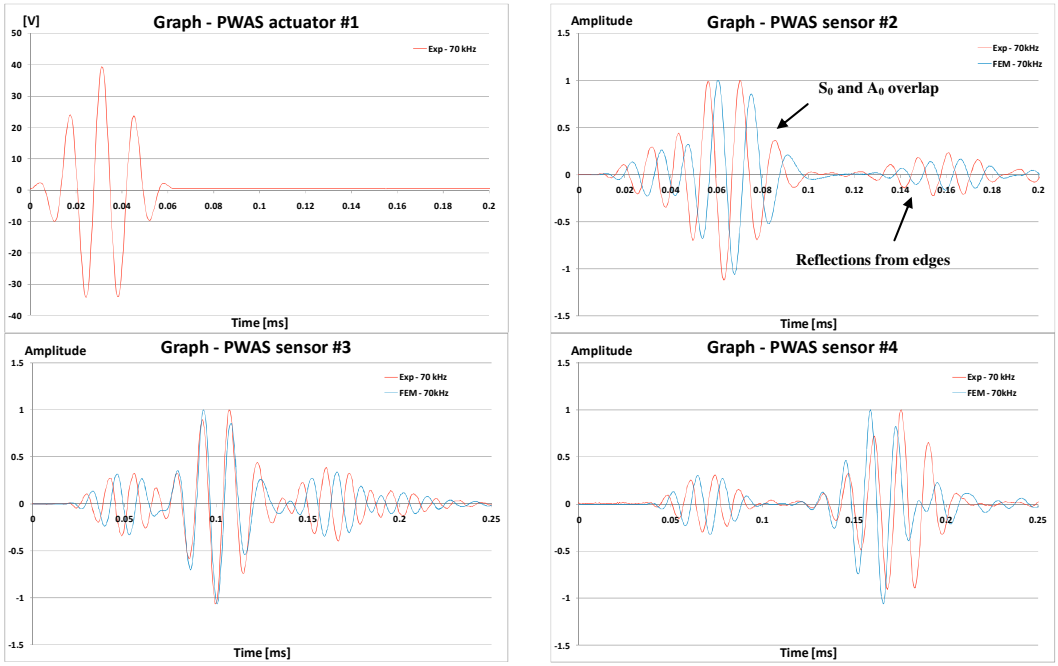

Fig 1.18 – Comparison Exp-FEM of Lamb waves propagation for frequency 70kHz.

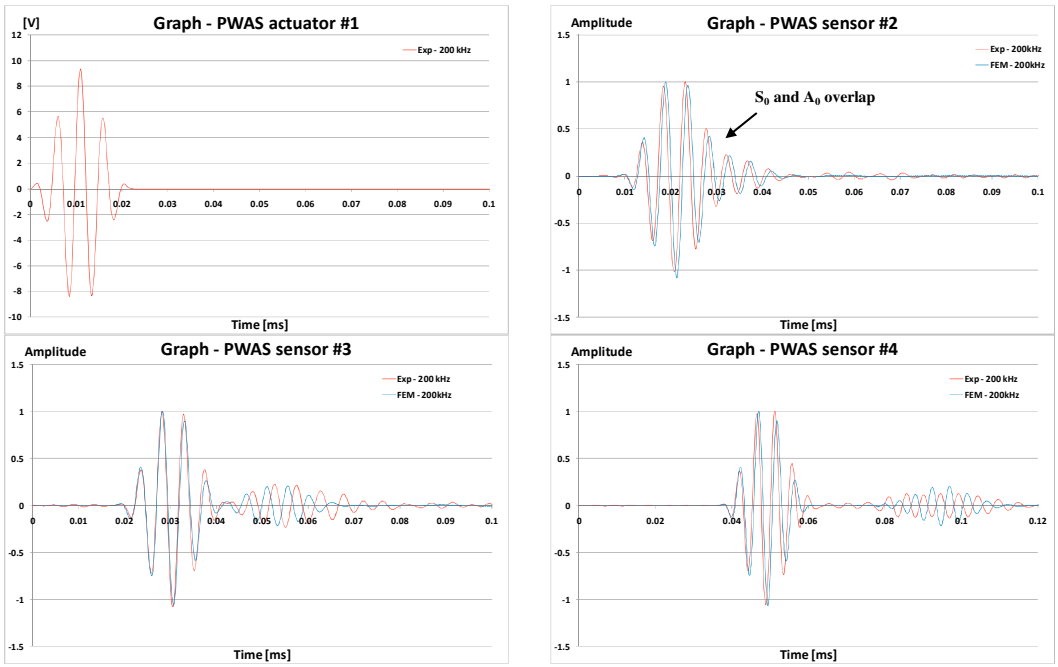

Fig 1.19 – Comparison Exp-FEM of Lamb waves propagation for frequency 200kHz.

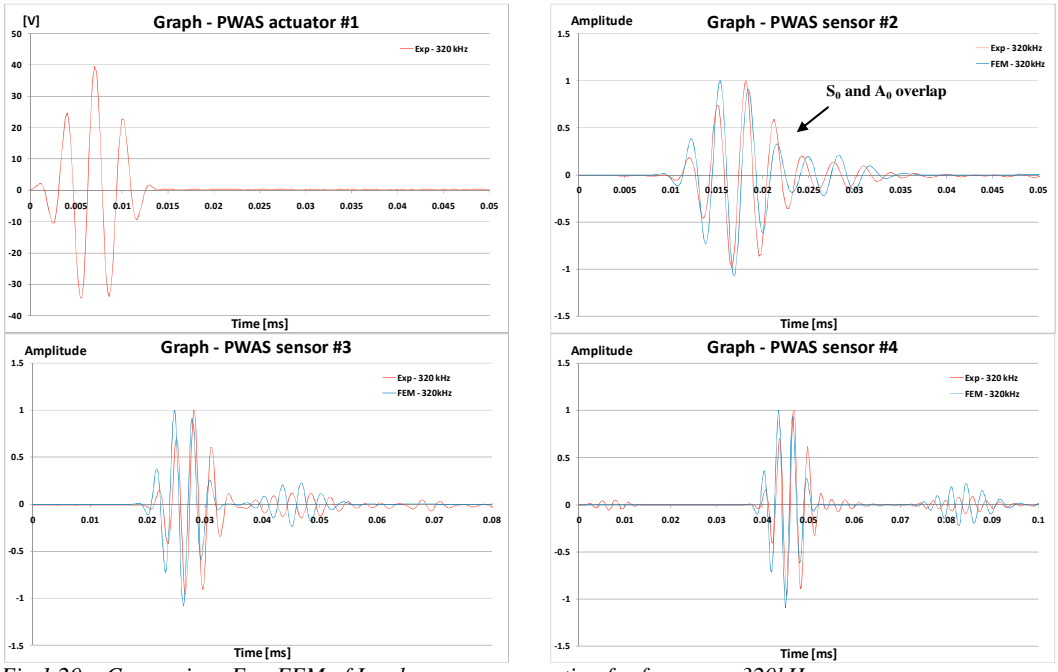

Fig 1.20 – Comparison Exp-FEM of Lamb waves propagation for frequency 320kHz.

As showed in Fig. 1.18, 1.19 and 1.20, all Lamb waves modes, for all frequencies and for all PWAS sensors, were correctly modeled with respect to the shape. Regarding positions only little shifts were present, for both A_0 and S_0, at 70kHz; while regarding amplitudes

there was a little difference, at 320kHz, between the FEM and the experimental waveforms, probably because the mesh size, for A_0, was not appropriate for that case: $\lambda^{A_0}_{320kHz} = 4.94$ mm: the model had less than 10 elements per wavelength. Nevertheless we can conclude that the physics of Lamb waves propagation and interaction with PWAS devices was correctly modeled [27]. A note on absolute amplitudes of signals: we presented all normalized curves since, in this analysis, we focused on correct modeling of the general physics of the problem. A quantitative analysis can be carried out by correlating the applied voltage with the real forces transferred to structure by PWAS actuators. A similar but not identical analysis has been performed during FEM modeling of low velocity impact events involving PWAS sensors (Chapter 2).
The crucial advantage of this FEM modeling technique is that we simulated Lamb waves propagation involving PWAS devices with very simple models and very low computational costs for solution: for the presented aluminum plate, at the various involved frequencies, solution times varied from 2 hours (320kHz solution) to 5 hours (70kHz) with a 8 cores (AMD Opteron 2GHz) computer. Solution time in explicit FEM codes is approximately a linear function with the termination time of the analysis and with the number of elements of the model, whereas for implicit schemes it increases dramatically with termination time and size of the finite element model.

1.3.4 Test on a composite plate (experiment).

After obtaining a good modeling of Lamb waves propagation for an isotropic material, we considered, in our analyses, a fiberglass/epoxy composite plate. The case of orthotropic or transversely isotropic, or even anisotropic materials in general [Appendix], with respect to FEM modeling, did not introduce any additional complication since it was sufficient, during the pre-processing phase, to use the specific material model instead of the isotropic one. The only problem, always to be faced when dealing with composites, was the difficulty to have correct values of the material elastic properties. In the case of an orthotropic material it is characterized by nine elastic material constants: three Young modules (E_1, E_2, E_3), three shear modules (G_{12}, G_{13}, G_{23}), three Poisson's ratios (ν_{12}, ν_{13}, ν_{23}). Typically the two in-plane Young modules are easier to measure through a simple tensile test, while the other ones are more difficult to estimate. Anyway we found, facing this problem, that Lamb waves propagation also suggests a method for estimating some.
The structure under investigation was a Norplex-Micarta 'NP130' fiberglass plate, provided by Prof. Victor Giurgiutiu, Director of Laboratory for Active Materials and Smart Structures (LAMSS, Department of Mechanical Engineering, University of South Carolina, Columbia SC, USA). The NP130 (NEMA FR-4) consists of a woven glass fabric substrate combined with a halogenated epoxy resin system. All the plies are oriented in the same direction, so the resulting laminate is symmetric and presents two main directions with very similar elastic properties: at 0° (LW - Lengthwise direction) and 90° (CW - Crosswise direction).

In order to model correctly the material, all the elastic constants needed to be determined; for this reason a tensile test was preliminarily performed for estimating the two in-plane Young modules. A number of rectangular specimens, both at 0° and 90°, were cut from a big NP130 plate by using a water-jet cutting machine (Department of Civil Engineering, USC), according to ASTM D-3039 (Standard Test Method for Tensile Properties of Polymer Matrix Composite Materials) (Fig. 1.21 and 1.22).

Fig. 1.21 – Water-jet cutting machine present at Department of Civil Engineering, University of South Carolina, Columbia SC, USA.

Fig. 1.22 – Specimens from NP130 according with Standard Tensile Test Method ASTM D-3039

The tensile test was performed at Mechanical and Aerospace Engineering Department, University of California, Los Angeles, USA (UCLA) by courtesy of Prof. Ajit Mal, Director of UCLA Nondestructive Evaluation Research Group.
The results of the tensile test are shown in Fig. 1.23.

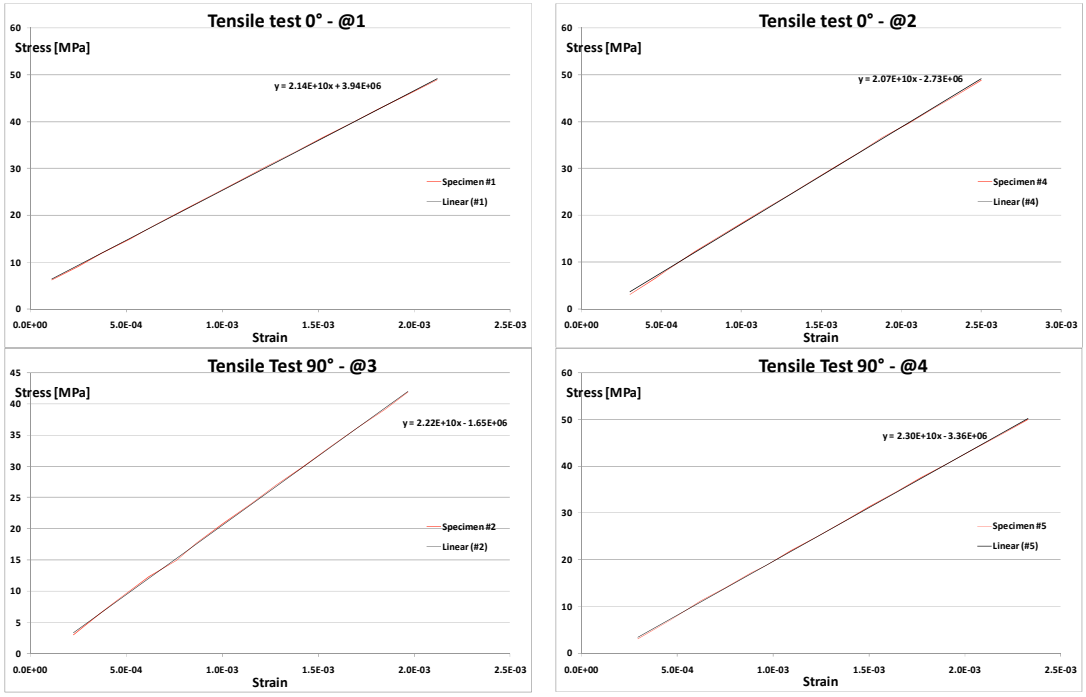

Fig. 1.23 – Results of tensile test for NP130 material

The average of the two tests, both for LW and CW directions, gave the values for Young modules:

$E_{0^\circ} = E_1 = (E_1^{@1} + E_1^{@2}) / 2 = (21.4 + 20.7) /2 = 21.05$ GPa

$E_{90^\circ} = E_2 = (E_2^{@3} + E_2^{@4}) / 2 = (22.2 + 23.0) /2 = 22.6$ GPa

In a first step we used, for the other elastic constants, the values available from other tests:

$E_3 = 4.32$ GPa (manufacturer)

$G_{12} = 5.6$GPa (test for shear modulus performed at USC by Patrick Pollock and Siming Guo, for a different thickness NP130 plate)

$G_{13} = 5.9$ GPa (typical value for fabric fiberglass/epoxy)

$G_{23} = 6$ GPa (typical value for fabric fiberglass/epoxy)

$\nu_{12} = 0.15$ (test for Poisson's ratio by Pollock and Guo, USC)

$\nu_{13} = 0.38$ (typical value for fiberglass/epoxy)

$\nu_{23} = 0.4$ (typical value for fiberglass/epoxy)

The plate dimensions were 925x925x3.2 mm^3, and a large number of PWAS disks (Steminc SM412, 7mm diameter disks) were used for Lamb waves propagation analysis, involving various angular directions. The PWAS actuator (#0) was placed at 300mm distance from two of the plate edges (Fig 1.24). For 0° direction three sensors were placed at distances from PWAS #0: 150mm (#1), 225mm (#2), 300mm (#3); for 45° direction four sensors were placed at distances from source: 150mm (#4), 225mm (#5), 300mm (#6),

450mm (#6+); other 19 PWAS sensors were bonded at the various angular directions, from 0° to 90° step 5°, all at a distances of 300mm from PWAS actuator (Fig. 1.24).

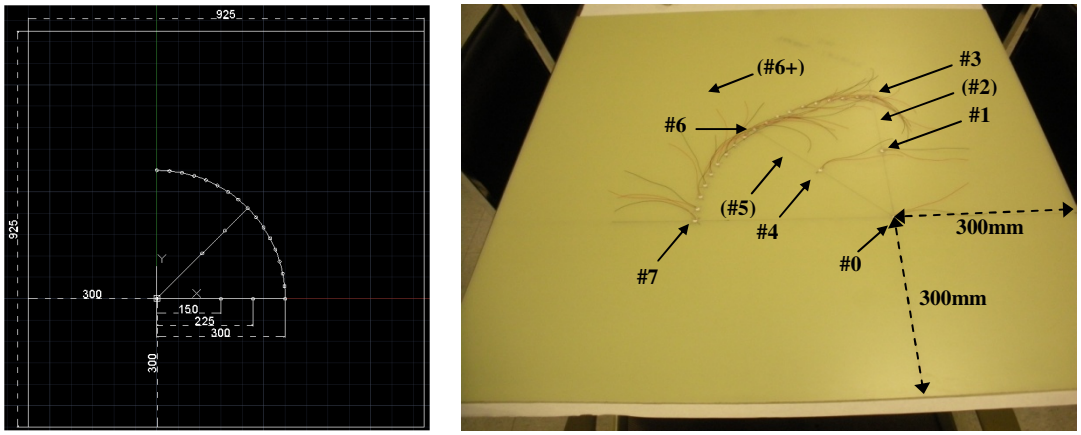

Fig. 1.24 – NP130 plate used for Lamb waves propagation tests

We performed the experimental acquisitions, from 1 to 500 kHz step 1 kHz, using PWAS #0 as actuator, and the other PWAS disks as sensors. As exciting signal we used 3 sine cycles with Hanning window, having maximum amplitude 10 Volts (Fig. 1.25). In Fig 1.26 some Lamb waves acquisitions are presented for both 0° and 45°.

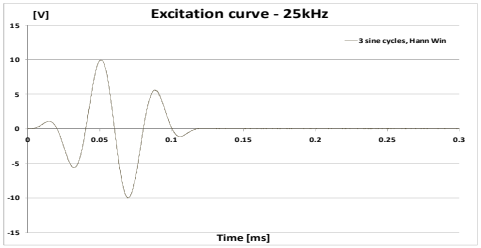

Fig. 1.25 – 3 sine cycles curve with Hanning window

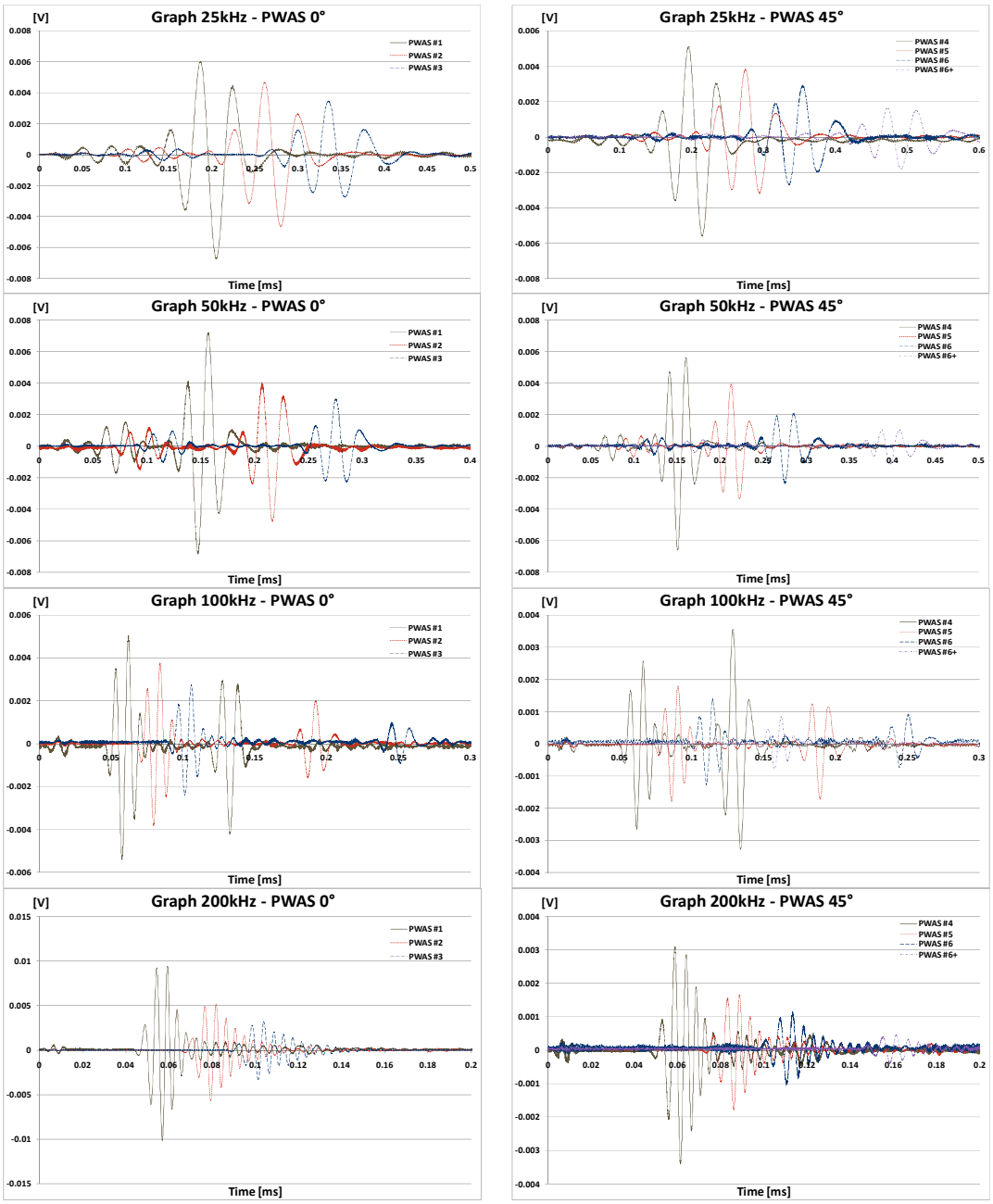

Fig. 1.26 – Experimental results of Lamb waves propagation for NP130 plate

From acquisitions presented in Fig. 1.26 we can clearly notice the tuning effect of PWAS since, from 25 to 200 kHz, S_0 mode continuously increase in amplitude, whereas A_0 mode increases from 25 to 50 kHz for then decreasing from 50 to 200 kHz. Group velocities were measured from experimental curves through the aid of the 'AGU-Vallen Wavelet' software (Vallen Systeme GmbH, Germany) (Tab 1.1 and Fig. 1.27).

Tab 1.1				
(0°, 45°) [m/s]	25 kHz	50 kHz	100 kHz	200 kHz
S_0	(3492, 3308)	(3458, 3135)	(3376, 3070)	(3058, 2768)
A_0	(1076, 1048)	(1232, 1227)	(1274, 1301)	(n.p., n.p.)

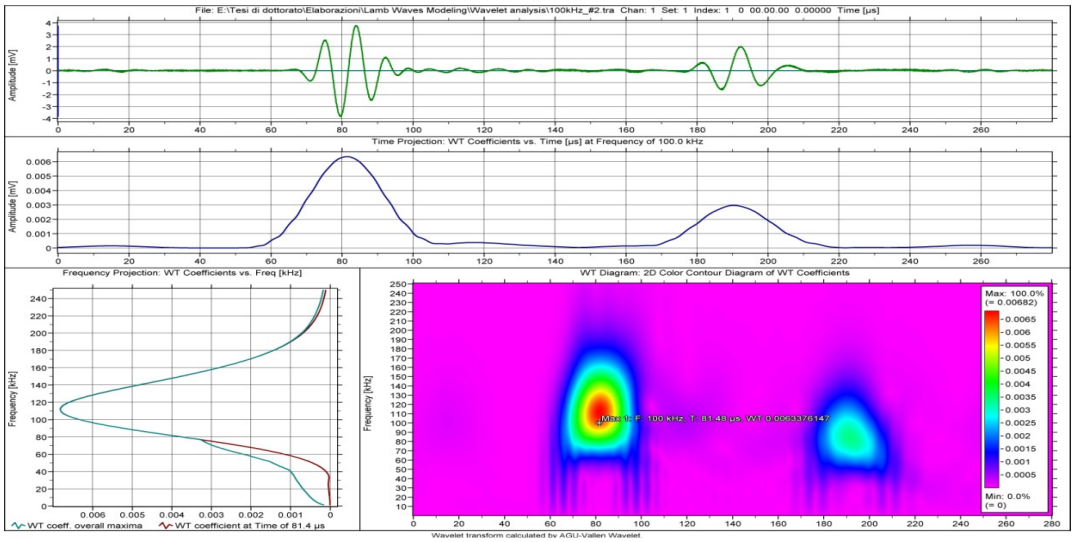

Fig. 1.27 – Results of the Wavelet analysis for a signal at 100kHz

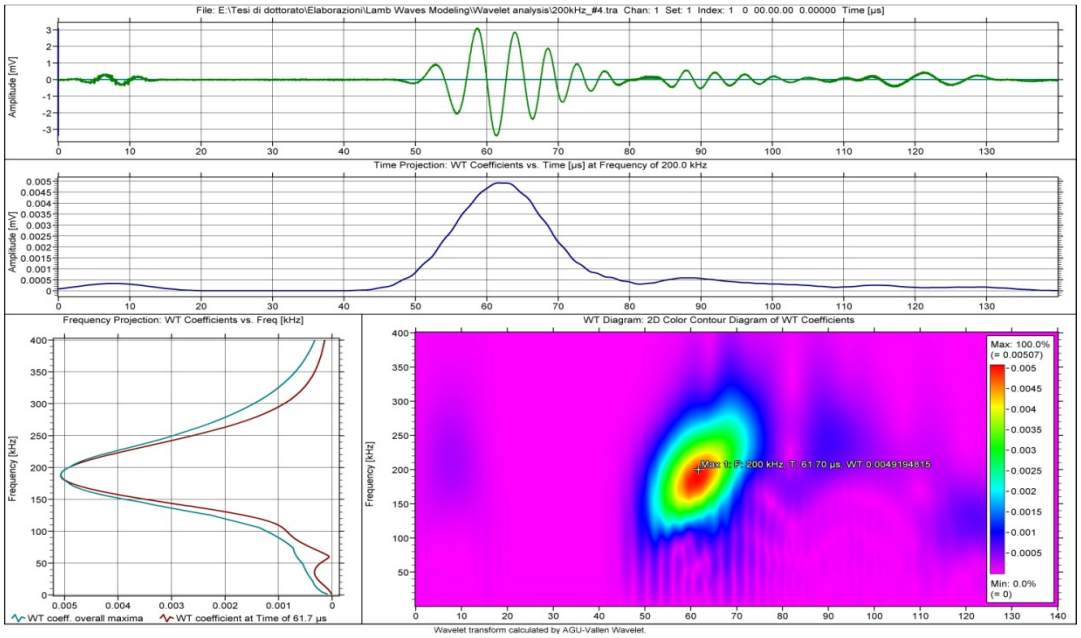

Fig. 1.28 – Results of the Wavelet analysis for a signal at 200kHz

It can be clearly noticed, from Fig. 1.27, that, for frequency 100kHz and 0° direction, we are on an ascending part of the S_0 tuning curve: this because the signal registered at PWAS #2 (0°, 225mm) presents, for the S_0 wave packet, a frequency content centered around 110kHz, and thus higher than the exciting signal (100kHz). On the contrary (Fig. 1.28), for

200kHz and 45°, we are on a descending part of the S_0 tuning curve: the wave packet at PWAS #4 (45°, 0.255mm) presents a downward shift of about 10kHz.

1.3.5 Test on a composite plate (FEM).

After performing Lamb waves experimental analyses for the NP130 plate we considered the FEM modeling of the same fiberglass/epoxy plate: a direct transient analysis was carried out through the use of the explicit FEM code LS-Dyna. For modeling the plate we used 3D brick elements with dimensions 1x1x1.07 mm^3; non-reflecting conditions were also used at the boundaries in order to model just a more limited region of the entire plate, instead of the entire one. Therefore the real plate had dimensions 925x920x3.2 mm^3 while the FEM model had dimensions 600x600x3.2 mm^3, thus obtaining 600x600x3 = 1080000 total number of elements (Fig. 1.29).

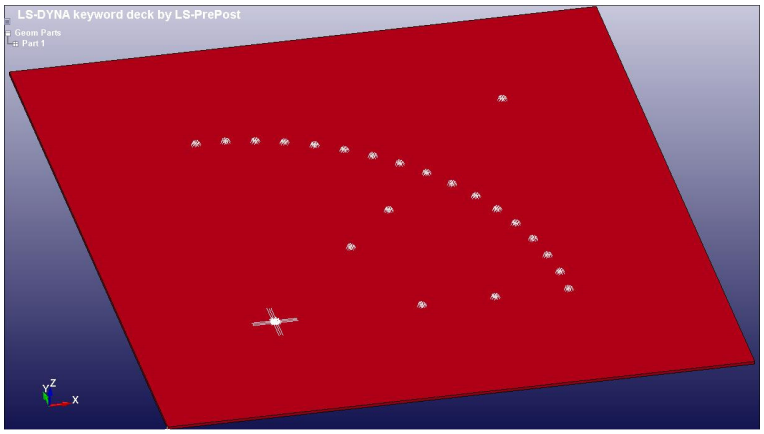

Fig. 1.29 – FEM model of the NP130 plate for Lamb waves propagation

For modeling PWAS transducers in FEM we used the same technique presented in Par. 1.3.3, for the aluminum plate. As exciting curve we used the same as the experimental acquisitions on NP130 (3 sine cycles with Hanning, Fig. 1.25), involving two frequencies: 65kHz and 165kHz. From theory (LAMSS 'Guided waves' code for composites) the smallest phase velocity between S_0 and A_0, at 65kHz, was found $c_{ph}^{A_0}$ = 830m/s, so obtaining $\lambda^{A_0}_{65kHz}$ = 12.77mm. For frequency 165kHz only S_0 mode was present in the experimental acquisitions, having a higher value for the wavelength: $\lambda^{S_0}_{165kHz}$ > 12.77mm. For these reasons we concluded that the smallest number of elements per wavelength, nevertheless considered enough, was relative to A_0 modeling at 65kHz: 13 elements.
In a first step of FEM modeling we considered the material elastic properties presented in Tab. 1.2 (some of that were estimated by us while some others were provided by manufacturer).

Tab 1.2		
E_1 = 21.05 GPa	E_2 = 22.6 GPa	E_3 = 4.32 GPa
G_{12} = 5.6GPa	G_{13} = 5.9 GPa	G_{23} = 6 GPa
ν_{12} = 0.15	ν_{13} = 0.38	ν_{23} = 0.4

The FEM solution time on a 8 cores computer (AMD Opteron 2GHz) was about 45 minutes, and the comparison between the experimental acquisition and the numerical solution, for PWAS #2 (0°, 225mm), is shown in Fig. 1.30.

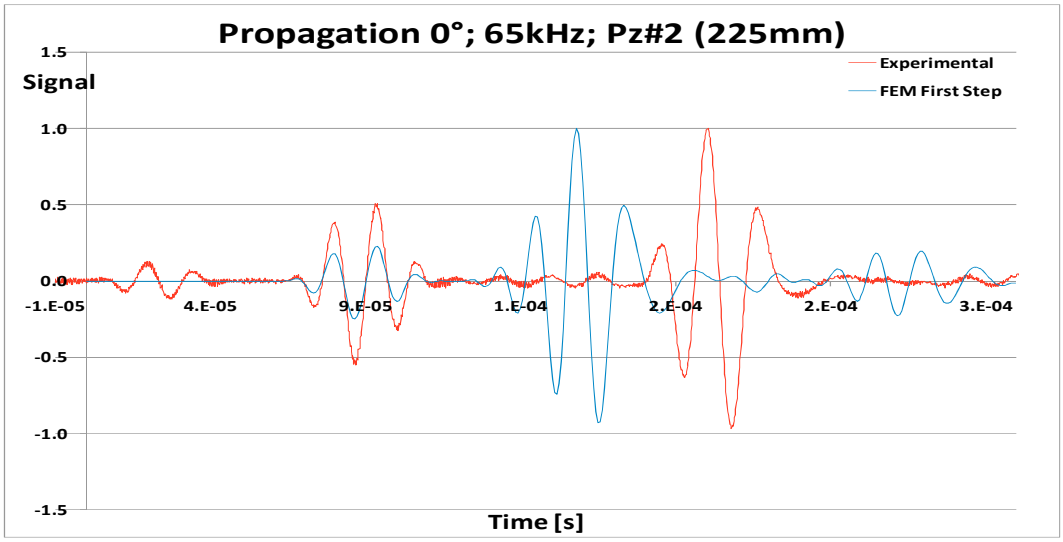

Fig. 1.30 – Comparison between the experimental acquisition and FEM solution for NP130, at a distance of 225mm and frequency 65kHz.

From the numerical-experimental comparison, reported in Fig. 1.30, it turned out that the S_0 wave was correctly modeled, whereas the experimental A_0 wave was found to be slower than the numerical one. Furthermore we found, during the simulations, that at 0° the S_0 wave mainly depends on the Young modulus in that direction E_1, while the A_0 wave on both E_1 and the out-of-plane shear modulus in that direction G_{13}. Since E_1 was determined experimentally (tensile test), we tried with various values of G_{13}, trying to correctly model the A_0 at 0°. We performed the simulations with various values of the shear modulus (Fig. 1.31): G_{13} [GPa] = {5.9; 4.9; 3.9; 2.9; 2.8; 2.7; 2.5;2.3}.

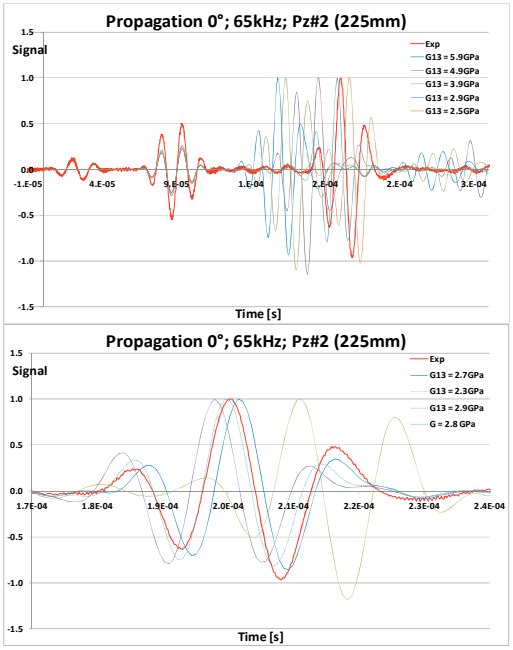

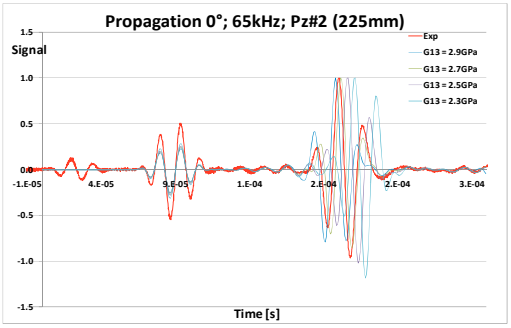

Three steps for obtaining G_{13}:

(a) G_{13} [GPa] ={5.9; 4.9; 3.9; 2.9; 2.5}

(b) G_{13} [GPa] ={2.9; 2.7; 2.5; 2.3}

(c) G_{13} [GPa] = {2.9; 2.8; 2.7; 2.3}

Fig. 1.31 – Test for estimation of elastic constant G_{13} for NP130

As clear from Fig. 1.31, S_0 waves at 0° were almost not affected by G_{13}, whose correct value was found to be G_{13} = 2.8 GPa: using this value in the FEM model, we obtained a good agreement between the numerical and experimental A_0 waves. We performed the same analysis for the direction 2 (PWAS #7) and we found G_{23} = 2.95GPa.

Through the simulations we also found that propagation of both the A_0 and S_0 modes, for 0° and 90°, were not significantly affected by in-plane shear modulus G_{12}, as clear from Fig 1.32.

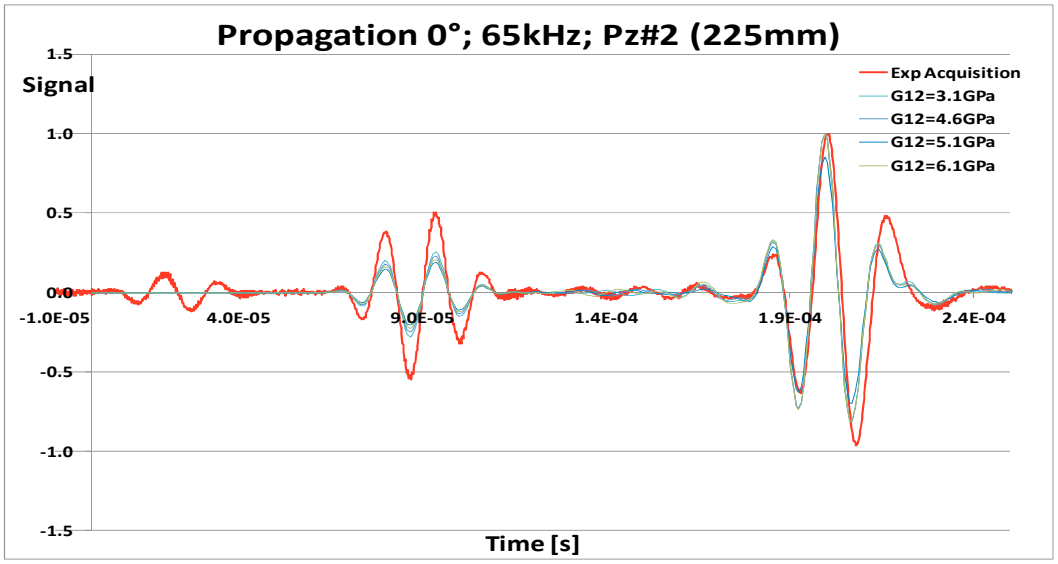

Fig. 1.32 – Results of Lamb waves propagation for NP130 plate at 0°, for various values of G_{12}

On the contrary we found that propagation at 45°, of both A_0 and S_0, was strongly affected by $\boldsymbol{G_{12}}$, hence we tried to estimate the in-plane shear modulus $\boldsymbol{G_{12}}$ from Lamb waves propagation at 45°: we tried to model correctly S_0 wave packet at 45° (PWAS #5) in shape and position by varying $\boldsymbol{G_{12}}$ [GPa] = {6.1; 5.6; 5.1; 4.6; 3.1} (Fig. 1.33).

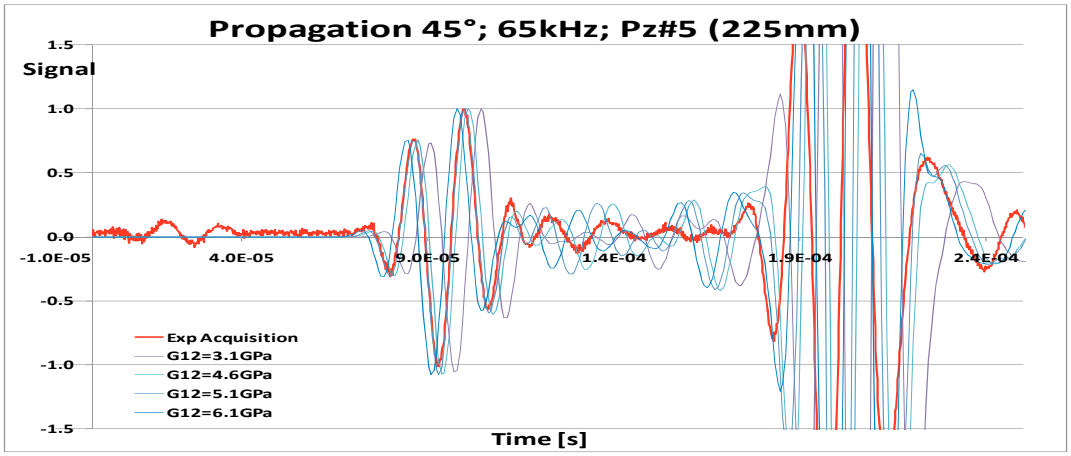

Fig. 1.33 – Results of Lamb waves propagation for NP130 plate at 45°, for various values of $\boldsymbol{G_{12}}$

The correct value was found to be $\boldsymbol{G_{12}}$ = 5.1GPa; in Fig. 1.33 is clear the dependence of both the S_0 and A_0 waves by the value of $\boldsymbol{G_{12}}$.

So, with Lamb waves propagation, we correctly estimated the material elastic constants: $\boldsymbol{G_{12}}$, $\boldsymbol{G_{13}}$, $\boldsymbol{G_{23}}$. Regarding $\boldsymbol{E_1}$ and $\boldsymbol{E_2}$, before evaluating the correct shear modules, we performed a number tests at both 0° and 90° for correctly modeling S_0 waves; from these tests we obtained values for the in-plane Young modules with an error of about 1GPa with respect to the ones from the tensile tests. The other material constants unfortunately (or fortunately) do not affect significantly Lamb waves propagation, as clear from Fig. 1.34; by changing all the three Poisson's ratios we found the same results as for $\boldsymbol{E_3}$: no changes in Lamb Waves both at 0° and 45°.

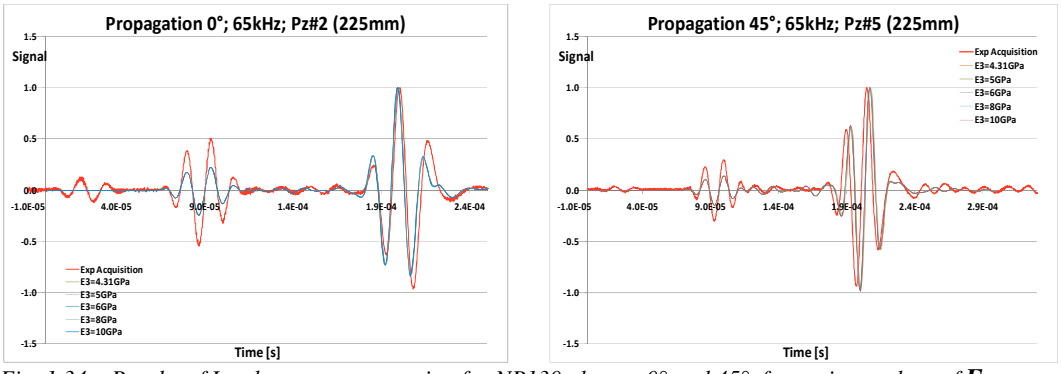

Fig. 1.34 – Results of Lamb waves propagation for NP130 plate at 0° and 45°, for various values of $\boldsymbol{E_3}$

Finally we present the results for Lamb waves modeling in composites, shown in Fig 1.35, using the material properties in Tab 1.3 (values with † were obtained through our tests):

Tab 1.3		
$E_1^{\dagger}$= 21.05 GPa	$E_2^{\dagger}$ = 22.6 GPa	E_3 = 4.32 GPa
$G_{12}^{\dagger}$ = 5.1GPa	$G_{13}^{\dagger}$ = 2.8 GPa	$G_{23}^{\dagger}$ = 2.95 GPa
ν_{12} = 0.15	ν_{13} = 0.38	ν_{23} = 0.4

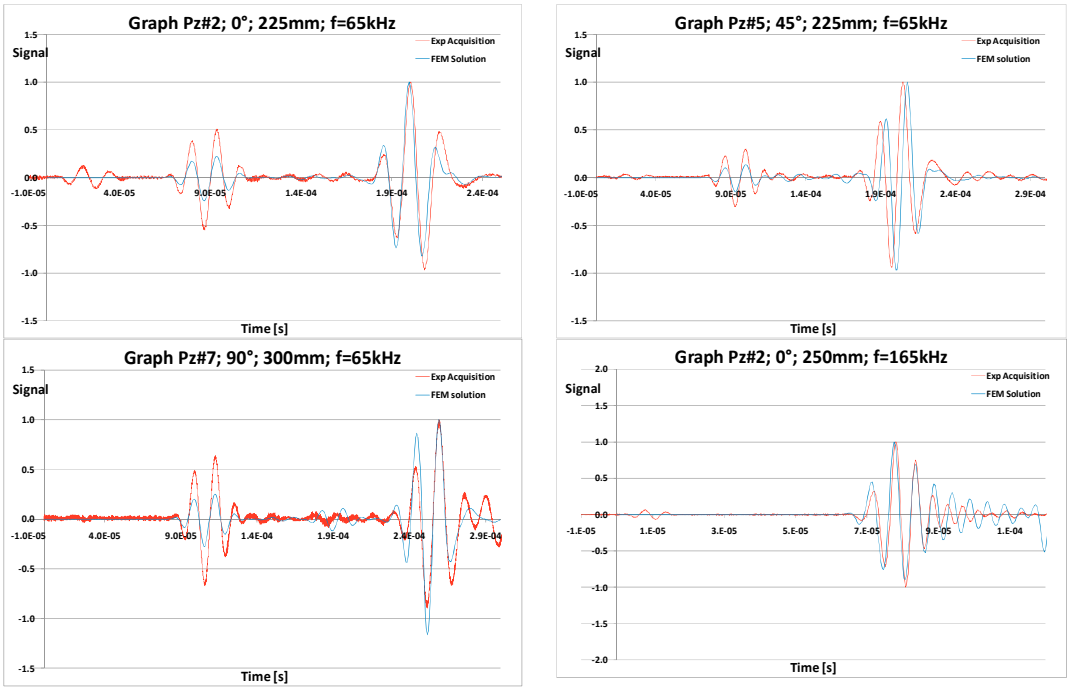

Fig. 1.35 – Results of Lamb waves propagation for NP130 plate, for frequencies 65kHz and 165kHz

In Fig 1.35 we can see that both the S_0 and A_0 modes were well modeled in shape and position for both 0° and 90°; for 45°, the S_0 was correctly captured while the A_0 presented correct shape with a very little shift. Also the result for a different frequency (165kHz) is shown, where, in the experimental acquisitions, the sole S_0 wave was present.

At the end of our analysis we can conclude that we were able to model correctly the propagation of Lamb Waves in composites using FEM, with a very low computational cost: order of hours; moreover this analysis gave us a tool for estimating the most important elastic material properties of a woven fabric composite.

2. IMPACTS

2.1 Introduction

Laminated composite materials are used extensively in aerospace and other applications. With their high specific modulus, high specific strength, and the capability of being tailored for a specific application, these materials offer definite advantages compared to more traditional materials. However, their behavior under impact is a concern, since impacts do occur during manufacture, normal operations, or maintenance. The situation is critical for impacts which induce significant internal damage, undetectable by visual inspection, that cause large drops in the strength and stability of the structure. Impact dynamics, including the motion of both the impactor and the target and the force developed at the interface, can be predicted accurately using a number of models. The state of stress in the vicinity of the impact is very complex and requires detailed analyses. Accurate criteria for predicting initial failure are generally not available, and analyses after initial failure are questionable. For these reasons, it can be said that a general method for estimating the type and size of impact damage is not available at this time. However, a large amount of experimental data has been published, and several important features of impact damage have been identified. In particular, interply delaminations are known to occur at the interface between plies with different fiber orientation. Their shape is generally elongated in the direction of the fibers in the lower ply at that interface. The delaminated area is known to increase linearly with the kinetic energy of the impactor after a certain threshold value has been reached. The effect of impact damage on the properties of the laminate has obvious implications for design and inspection of actual structures. Experimental results concerning the residual strength of impact damaged specimens subjected to tension, compression, shear, bending, and both static and fatigue loading are available. Analyses concentrate primarily on predicting residual tensile and compressive strength. In order to fully understand the effect of foreign object impact damage, one should understand impact dynamics and be able to predict the location, type, and size of the damage induced and the residual properties of the laminate. [Serge Abrate, "Impact on Composite Structures", Cambridge University Press, 1998].

From a certain point of view the most critical type of impacts for composites are low velocity impacts [22] [25]. These impacts, even if do not induce immediately significant damage, they can produce internal and not visible small damage. These damage, typically matrix cracking and delaminations between plies, might reduce the stiffness and strength below the sizing limit loads (especially in compression) and propagate dramatically during normal operations of structures threatening the integrity of the whole structure. A low velocity impact is an impact whose energy does not allow to generate penetration, and typically the speeds involved are of the order of tens of meters per second, and the energies of the order of tens of Joules. Moreover, during a low velocity impact event the strain rates

can be neglected, and quasi-static failure criteria can be adopted to estimate the extension of damage [25]. To understand what happens to the structure after an impact let's consider the Fig 2.1.

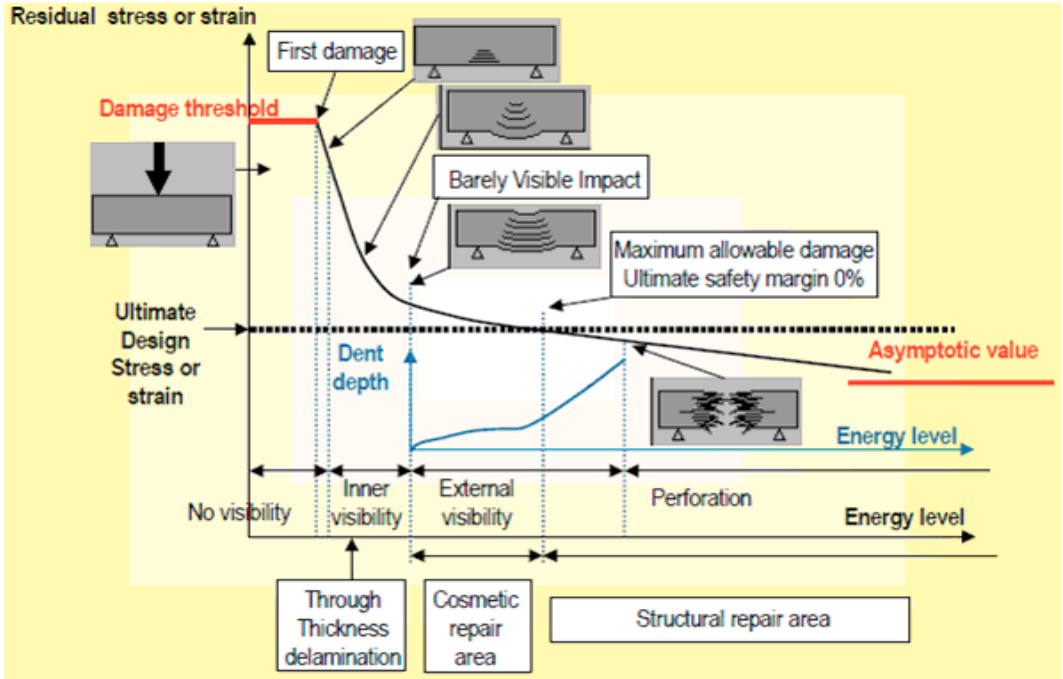

Fig. 2.1 – Impacts on composite structures

On the x-axis we can see the energy involved in the impact, while on the y-axis the residual stress/strain of the thin-walled structure subject to the impact. There is an elastic range, from zero to the "First damage" point, where the response of the structure is elastic thus without any permanent damage. Above the "First damage" energy value a damage occur and, within the range of "Inner visibility", the damage can't be noticed through an external visual inspection: no external permanent indentation is present. For increasing values of energy a permanent indentation appears on the top surface at the impact location, and for high values of impact energy even perforation can occur.

For low velocity impacts we are generally in the range of energies between Inner and External visibility: delaminations occur. A delamination, induced by an impact or even by something else, generally is not very dangerous at the precise moment when it's produced. Structures are designed using Safety Factors that allow them to carry loads beyond the expected or actual ones, so a delamination, if it's not very large, does not bring the residual stress below the Ultimate Design Stress (Fig 2.1). The very challenging problem of delaminations is that they usually propagate when the structure is subject to load cycles, so their dimensions increase during time. After an impact, even if the damage dimension is not alarming, a deep inspection must be performed since small and even negligible

damage, with high probability, will grow during lifetime of the structure bringing the Residual Stress under the minimum required.
Maintenance and inspection in the aerospace environment are very costly and, for civil aircrafts, absorb about 20-25% of the entire operational costs. If we also consider that a small delamination is a barely visible damage, hence very difficult to identify with a simple visual inspection, we conclude that an impact and delamination detecting tool is strongly required: a tool that is able to detect an impact event in time, to localize it in space, to estimate its energy, and finally to give precise information on the consequences in terms of type and extension of damage, induced at the impact point. Such a damage detecting tool would reduce the risk of unexpected failures and the cost of scheduled but unneeded maintenance.
By considering an aircraft (Fig 2.2), there are some specific areas interested in low velocity impacts. While the aircraft's cockpit, wing leading edges and tail are interested much more in impacts involving high speeds and energies, eventually with penetration (bird impact), the upper and lower shells of both the fuselage and wings are subject to debris impacts, during the takeoff and landing maneuvers, and to tool drop impacts during maintenance, hence mostly by events that involve small energies and speeds.

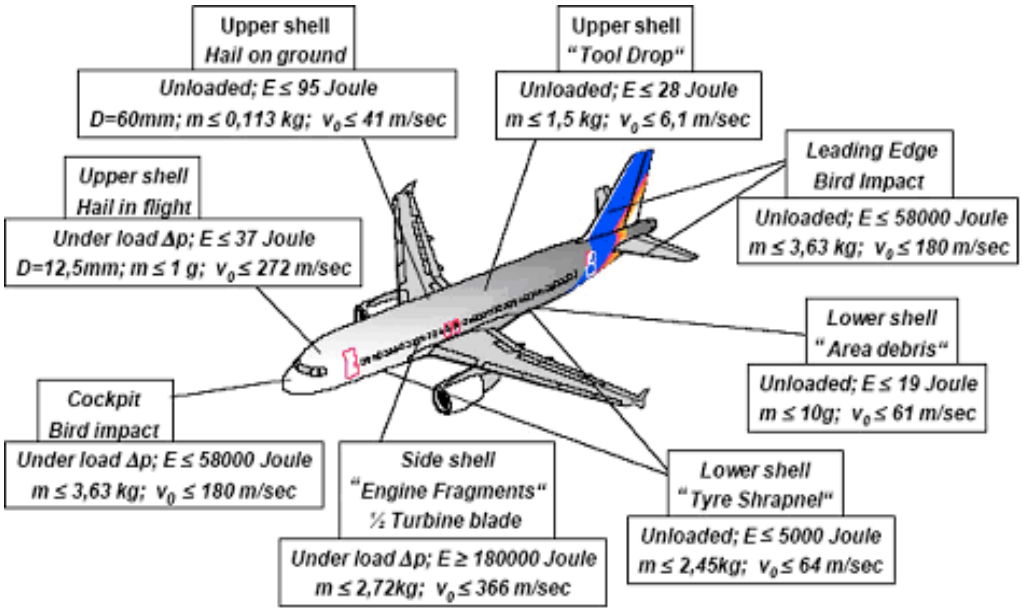

Fig. 2.2 – Aircraft subject to impacts

Regarding impacts detection in time, localization in space and estimation in terms of energy, this is generally achieved by using an array of sensors anchored on the structure that constantly "sense" and, in case of impact, record the signals of the elastic waves generated by the event. In figure 2.3 we can see an example of a grid of sensors. From the

knowledge of the speed of the elastic wave generated by impact and traveling in the plate, from theory and/or experiments, and by considering the precise instants when each sensor acquires the signal, through a triangulation technique, we can locate in time and in space the impact. Regarding the energy involved in the impact it can be directly linked to the amplitude of the elastic wave acquired by sensors.

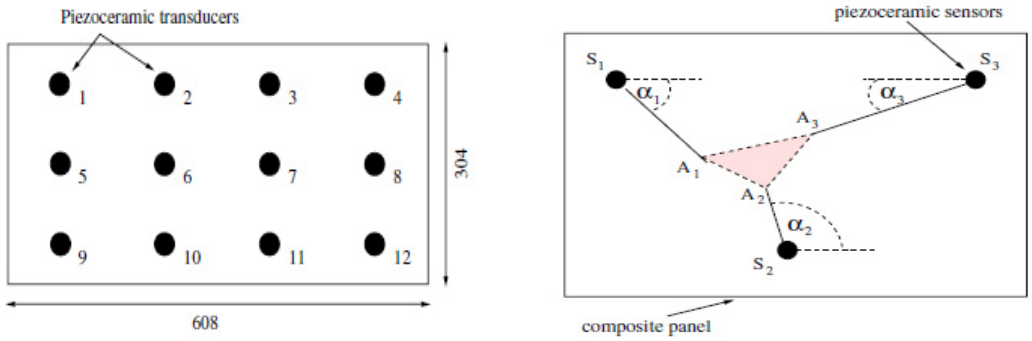

Fig. 2.3 – Grid of sensors for impact point identification

One of the most advantageous technique for impact sensing involve piezoelectric transducers directly bonded onto the structure [20] [23], for their capability to be used also for damage detection, after impacts, using Lamb waves.

2.2 Generalities on impacts.

Regarding the mechanism of damage induced by impacts on composites, we shall distinguish between low and high velocities. For high velocities damage is originated from high contact stresses on the top of the impacted surface (Fig 2.4a): this induces a conical damage just below impact point; let's notice that this behavior is also typical for thick plates subject to impacts [21]. On the contrary, for low velocity impacts, the bending of the structure causes high values of stresses at the bottom part of the impacted surface: this induces matrix cracking which are deflected at the lowest interface to form a delamination, then this mechanism is also transferred in the layers above [24] (Fig 2.4b).

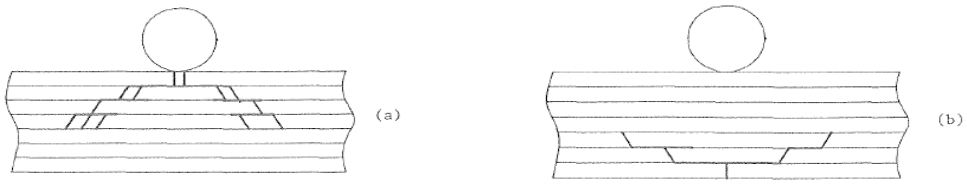

Fig 2.4 – Damage development in (a) rigid and (b) flexible targets

Regarding the severity of the damage that an impact can induce into a structure, it is function of the impactor properties such as mass, speed, geometry, angle of impact, etc.,

and of the properties of the impacted structure such as material, geometry, boundary conditions, etc. [21]. The problem is very complex and involves the analysis of the induced stresses inside the material nearby the impact position; simple formulas taking into account all the parameters involved in phenomenon are not easily available. In this case a direct transient FEM analysis is required for the application of failure criteria that usually involve both laminar and interlaminar stresses. Choi and Chang presented a quasi-static delamination criterion for estimating the damage caused by a low velocity impact event on a layered composite made up of differently oriented unidirectional laminas [25]. The criterion assumes that a delamination can occur only after a matrix-cracking event: if the matrix cracking propagates along the thickness and meets layers with different fiber orientations, the delamination occurs. The criterion is formalized by the conditions:

$$\langle 2.1 \rangle \quad \begin{cases} \left(\dfrac{{}^{n}\bar{\sigma}_{yy}}{{}^{n}Y} \right)^2 + \left(\dfrac{{}^{n}\bar{\sigma}_{yz}}{{}^{n}S} \right)^2 = e_m^2 & \text{Matrix cracking } (e_m \geq 1) \\ D_a \left[\left(\dfrac{{}^{n}\bar{\sigma}_{yz}}{{}^{n}S} \right)^2 + \left(\dfrac{{}^{n+1}\bar{\sigma}_{xz}}{{}^{n+1}S} \right)^2 + \left(\dfrac{{}^{n+1}\bar{\sigma}_{yy}}{{}^{n+1}Y} \right)^2 \right] = e_D^2 & \text{Delamination } (e_D \geq 1) \end{cases}$$

The criterion presents D_a as an experimental parameter, while ${}^{n}Y$ and ${}^{n}S$ are the in situ transverse strength (traction or compression) and the interlaminar shear strength of the n-th lamina, respectively; the stresses are calculated as averages within the lamina.
Although it is not easy to estimate with simple formulas the stresses inside the material, a simple relation between the contact force and the geometrical and structural properties of both the impactor and the structure was proposed by Hertz [26]:

$$\langle 2.2 \rangle \; F_c = k_H \cdot \alpha^{1.5} \quad ; \quad k_H = \frac{4}{3}\sqrt{r}\,\frac{1}{\left[\left(1-\nu_s^2\right)/E_s + 1/E_{yy} \right]}$$

with α indentation depth during impact, r radius of the impactor, E_s and ν_s material properties of the impactor, E_{yy} transverse modulus normal to the fiber direction in the uppermost composite layer. Anyhow through a FEM simulation the contact force can be obtained for each time step.

2.3 Numerical analysis of damage due to low velocity impacts.

In order to evaluate a numerical tool that is able to predict the damage size produced by a low velocity impact on a composite plate, we now present the numerical simulations, performed using the explicit FEM code LS-Dyna, compared with the experimental results

of the test case considered in the paper by Choi and Chang [25]. For predicting matrix cracking and delaminations after impact we used the Choi-Chang criterion <2.1>.
The test case consisted in a carbon/epoxy T300/976 composite plate subject to low velocity impact whose geometry and material specifications are presented in Tab. 2.1.

Tab. 2.1

Ply orientation	Thickness [mm]	Span length [mm]	Width [mm]
$[0_3/90_3/0_3/90_3/0_3]$	2.16	100	76

Elastic properties of T300/976 used in calculations		
In-plane longitudinal modulus	$\boldsymbol{E_{xx}}$ [GPa]	156
In-plane transverse modulus	$\boldsymbol{E_{yy}}$ [GPa]	9.09
In-plane shear modulus	$\boldsymbol{G_{xy}}$ [GPa]	6.96
Out-of-plane shear modulus	$\boldsymbol{G_{yz}}$ [GPa]	3.24
In-plane Poisson's ratio	$\boldsymbol{v_{xy}}$	0.228
Out-of-plane Poisson's ratio	$\boldsymbol{v_{yz}}$	0.4
Density	$\boldsymbol{\rho}$ [kg/m^3]	1540
Strength properties of T300/976 used in calculations		
Longitudinal tension	$\boldsymbol{X_T}$ [MPa]	1520
Longitudinal compression	$\boldsymbol{X_C}$ [MPa]	1590
Transverse tension	$\boldsymbol{^0Y_T}$ [MPa]	45
Transverse compression	$\boldsymbol{Y_C}$ [MPa]	252
Ply longitudinal shear	$\boldsymbol{^0S}$ [MPa]	105
Impactor properties (steel)		
Elastic modulus	$\boldsymbol{E}$ [GPa]	207
Poisson's ratio	$\boldsymbol{v}$	0.3
Total mass	$\boldsymbol{m}$ [kg]	0.16
Nose radius	$\boldsymbol{r}$ [mm]	6.35
Parameters		
Strength parameter	$\boldsymbol{A}$	1.3
Strength parameter	$\boldsymbol{B}$	0.7
Strength parameter	$\boldsymbol{C}$	2.0
Strength parameter	$\boldsymbol{D}$	1.0
Delamination growth parameter	$\boldsymbol{D_a}$	1.8
Adjacent plies with same orientation	$\boldsymbol{M}$	3
Angle between differently oriented plies	$\boldsymbol{\Delta\theta}$	90°

The strength parameters $\boldsymbol{A}$, $\boldsymbol{B}$, $\boldsymbol{C}$, $\boldsymbol{D}$ and $\boldsymbol{D_a}$ are empirical and are used, for evaluating the in situ strengths, in the formulas:

$$\langle 2.3 \rangle \; {}^{n}Y_T = {}^{0}Y_T \left(1 + A \frac{\sin(\Delta\theta)}{M^B} \right) \quad ; \quad \langle 2.4 \rangle \; {}^{n}S = {}^{0}S \left(1 + C \frac{\sin(\Delta\theta)}{M^D} \right)$$

The FEM model of the experiment consisted in a plate made up of 3D brick elements, with impactor modeled as a rigid sphere made up of shell elements. Since delamination, according to the damage criterion <2.1>, does not occur between adjacent plies having same orientation, each group of plies with the same orientation (0_3 and 90_3) was modeled with a single brick element: the resultant plate had five elements along the thickness. (Fig 2.5)

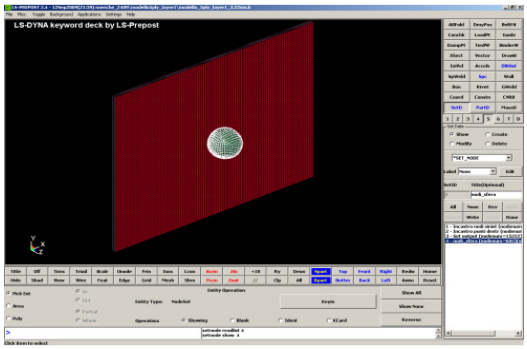

Fig 2.5a – FEM model of impact

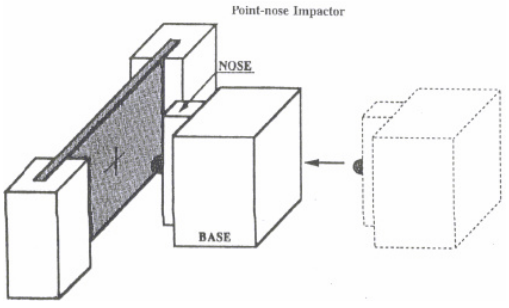

Fig 2.5b – Experimental impact test

The various parameters of the FEM model are presented in Tab 2.2. Let's notice that we used a finer mesh dimension with respect to the numerical study presented in the Choi-Chang paper.

Tab 2.2		
Plate elements size (bricks) [mm^3]	Number of elements of the plate	Sphere elements size (shell) [mm^3]
1.45 x 1.33 x 0.432	74 x 57 x 5	1.2 x 1.2 x 0.5

The plate was clamped on two opposite edges (as showed in the above Fig. 2.5b) and the impacts were performed at the velocities of: 2.9 m/s, 3.22 m/s, 4.00 m/s, 6.70 m/s.
In Fig. 2.6 we can see, for each value of the impactor speed, the extension of the matrix cracking and subsequent delaminations in the plate (the layers are considered to be five since we modeled every 3 adjacent plies with the same orientation as a single layer).

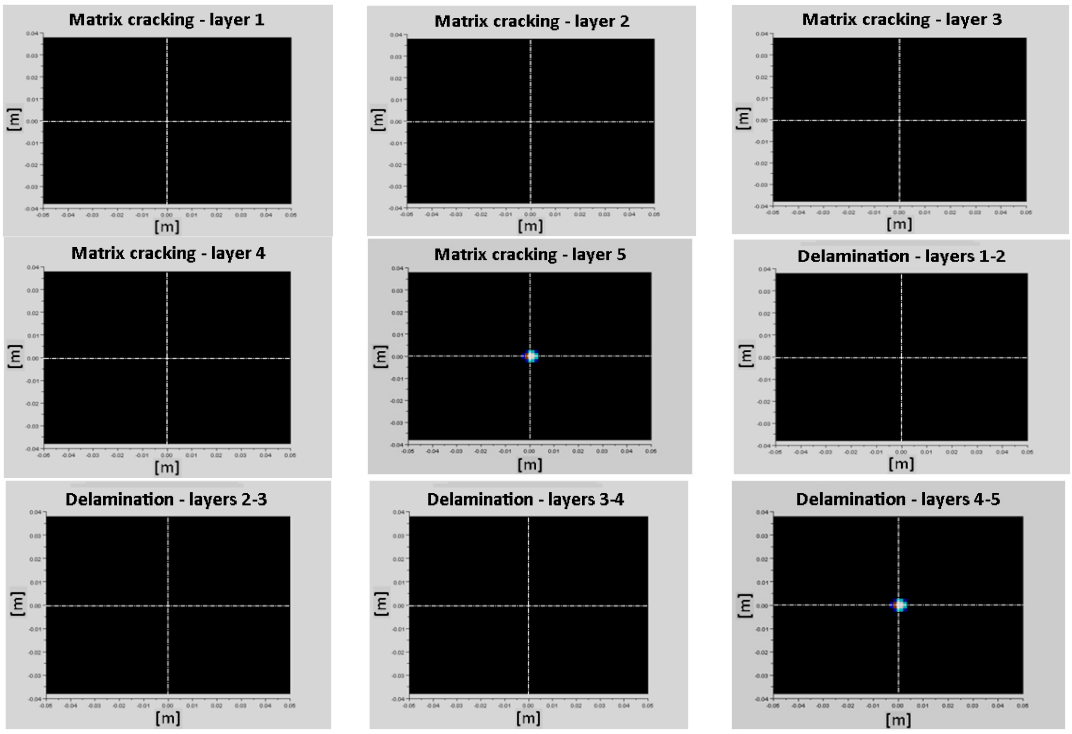

Fig 2.6a – Speed of impactor: 2.90 m/s

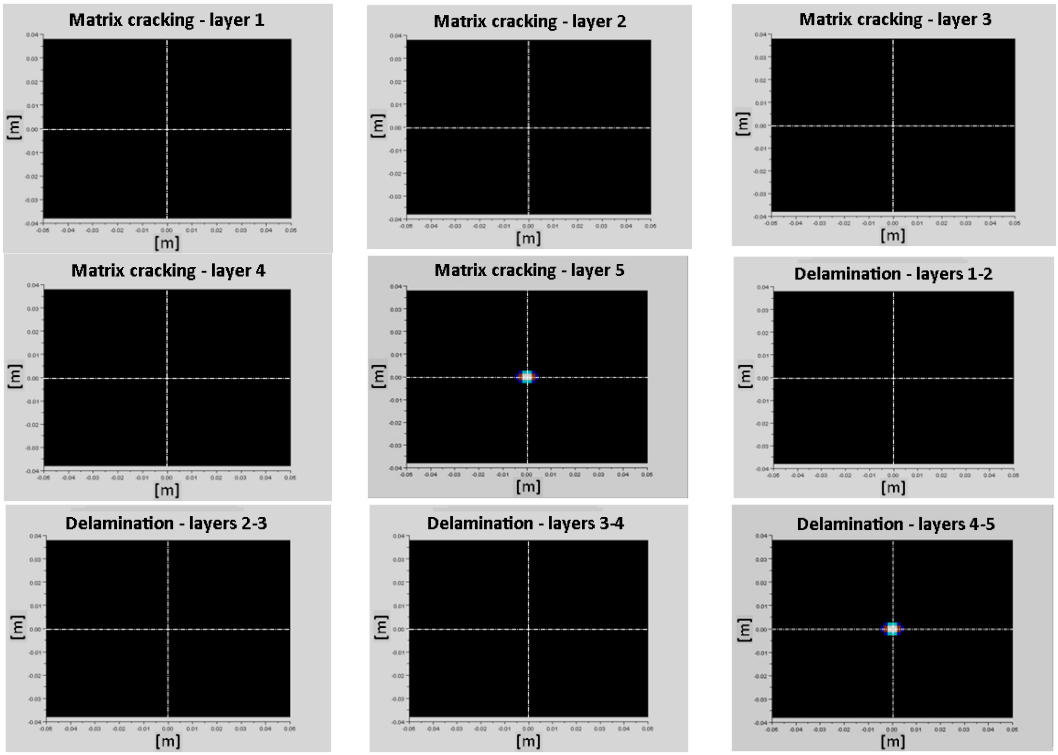

Fig 2.6b – Speed of impactor: 3.22 m/s

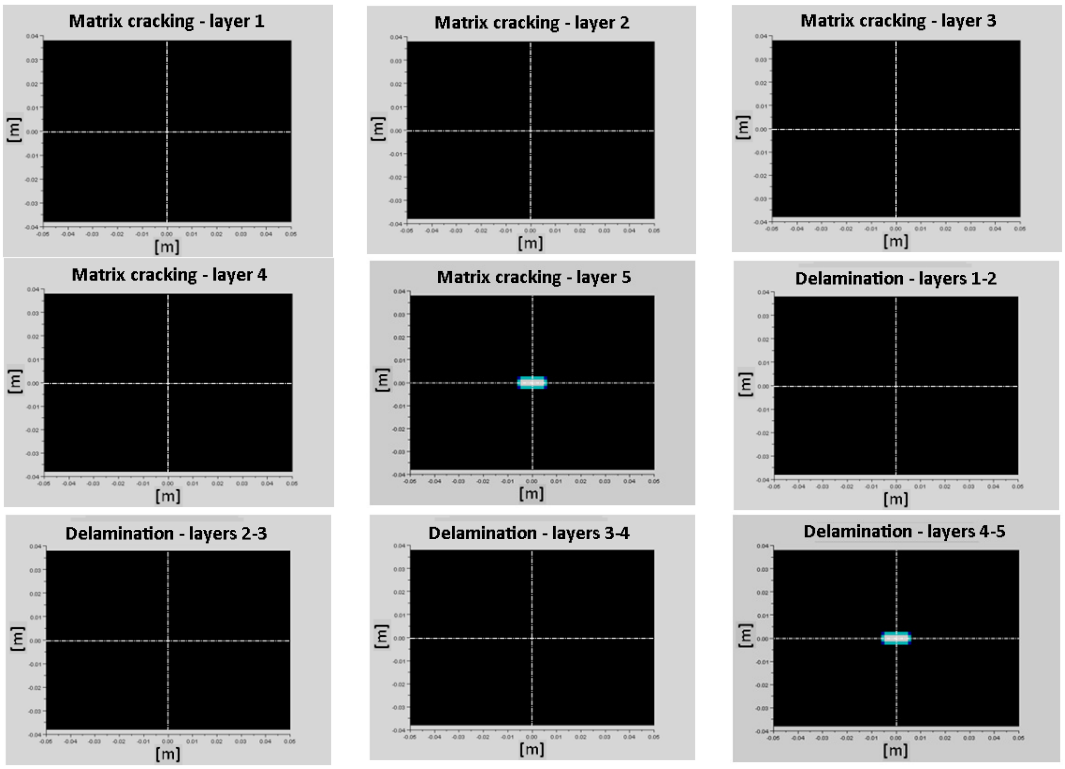

Fig 2.6c – Speed of impactor: 4.00 m/s

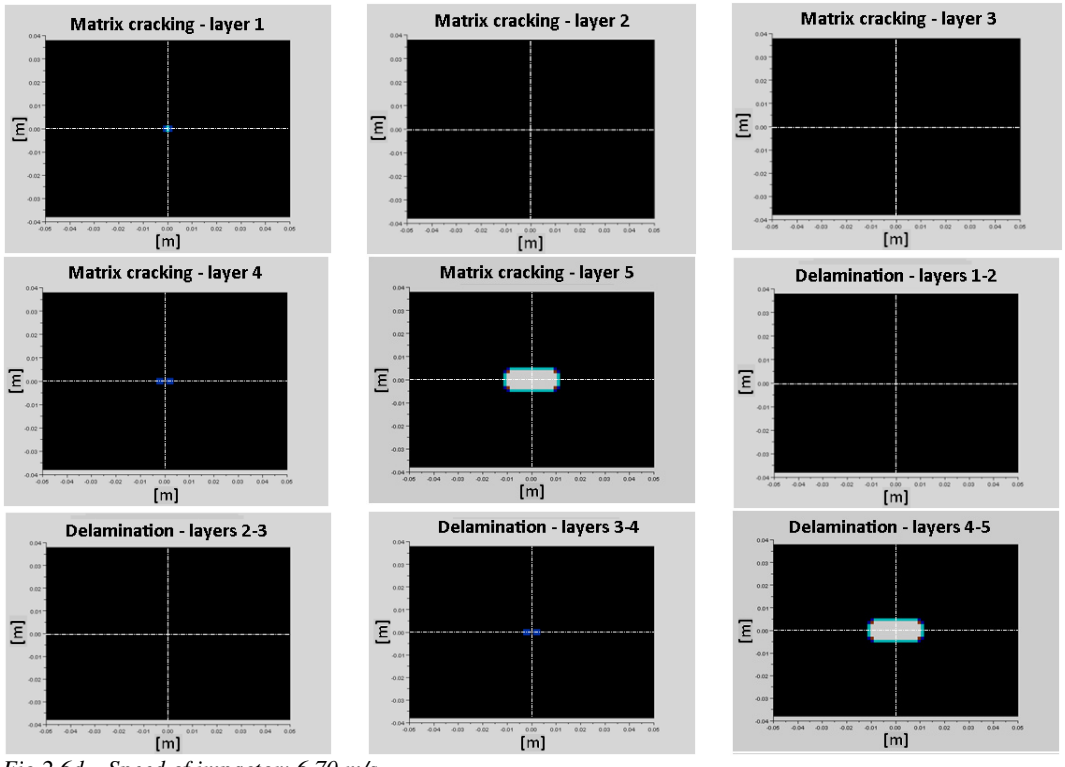

Fig 2.6d – Speed of impactor: 6.70 m/s

The resultant forces at the interface are presented in Fig. 2.7.

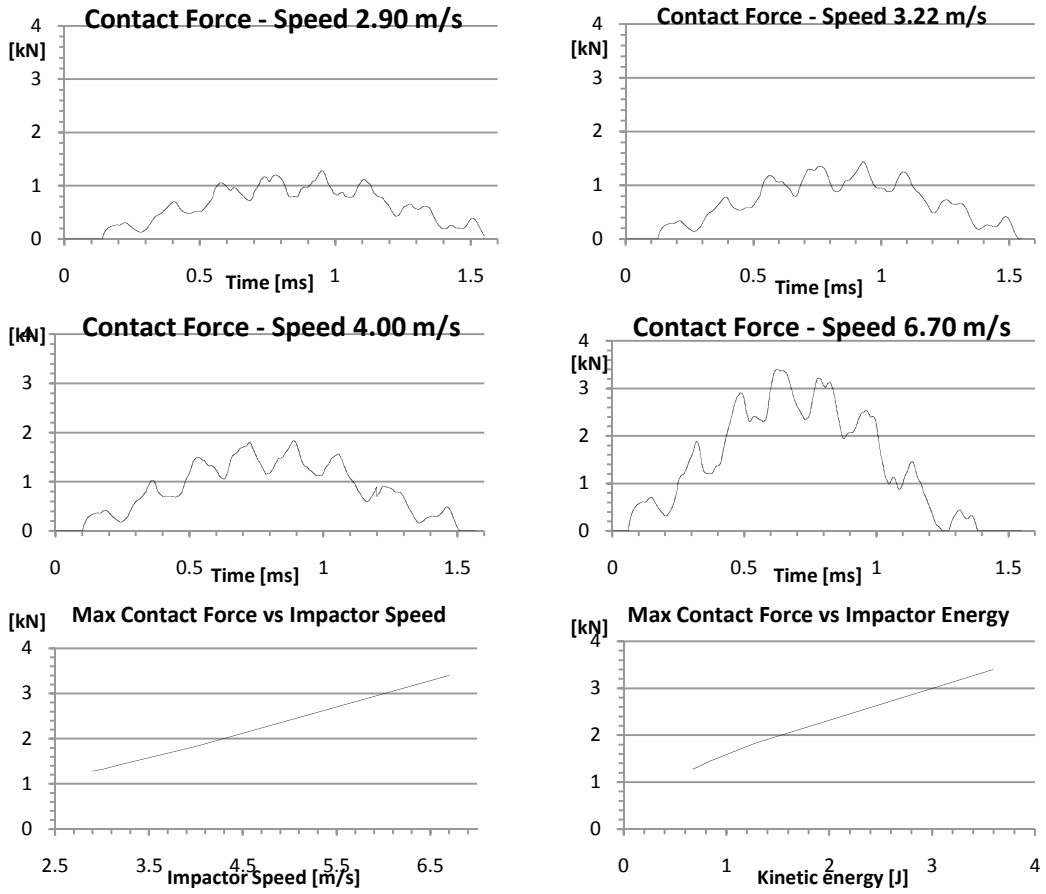

Fig 2.7 – Contact forces during the impact events

As we can see in Fig. 2.6, from 2.90 to 6.70 m/s both matrix cracking and delaminations occurred at layer 5 and interply 4/5, with an extension that increased with the impactor speed. For a speed of 6.70 m/s small matrix cracking were also present in layers 1 and 4 and this induced a small delamination at interply 3/4, but no delamination appeared at interply 1/2. In Fig 2.8 we can see the trend of the damage dimensions with impactor speed.

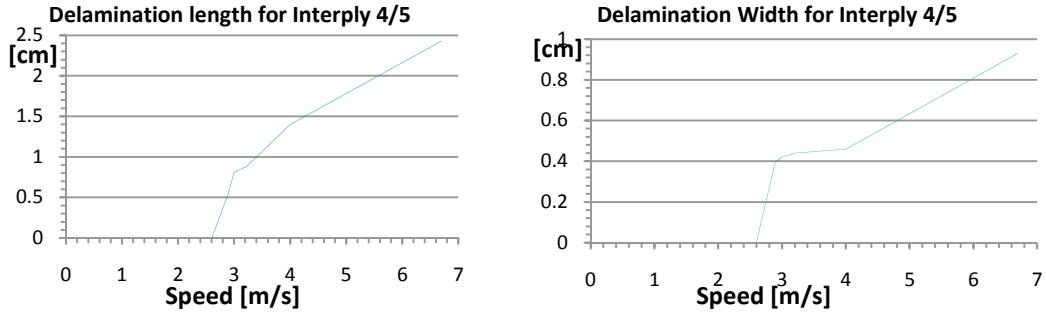

Fig 2.8 – Delaminations subsequent to impacts

We then compared our numerical results with both numerical and experimental results obtained by Choi and Chang and presented in their paper (Fig. 2.9).

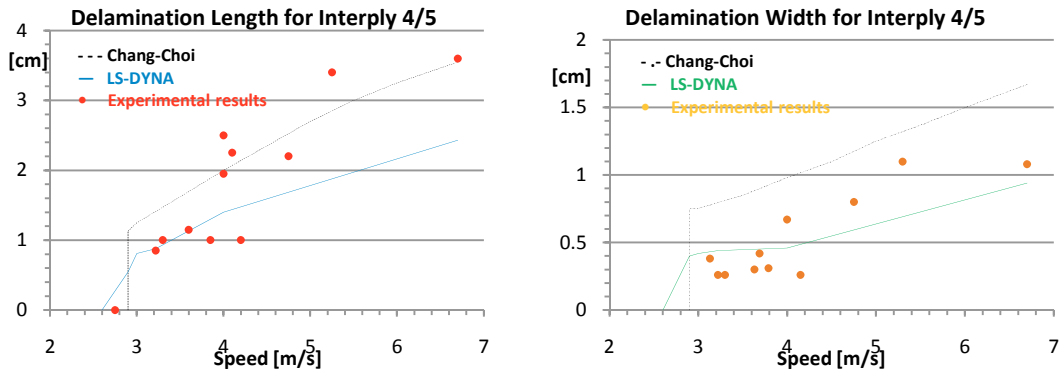

Fig 2.9 – Comparison between FEM results and experimental data

As we can see from the numerical and experimental comparisons in Fig 2.9, our analyses gave general better results than the cited authors for lower values of the velocity of the impactor. In detail we estimated correctly the delamination length for speed values up to 4 m/s, while, for higher values of speed, we underestimated it. Regarding delamination width, we obtained a general better estimation. This was probably due to the use, in our analysis, of a more refined mesh with respect to the one used by Chang and Choi.

2.4 Impacts: experimental and numerical tests.

2.4.1 Test on a carbon/epoxy composite plate.

In this experimental test we considered a woven fabric carbon/epoxy composite plate subject to an impact. We were interested in both the damage evolution and the analysis of the signals gathered by the PWAS sensors bonded on the plate. The signals were produced by the strain waves generated during the impact and propagating from the impact point. For this purpose, a number of piezoelectric disk sensors (PWAS disks of 10mm diameter, PIC-255) were bonded on the upper surface of the plate.

The plate material was RC200T-3k carbon in epoxy matrix, and its dimensions were: 440 x 440 x 3.2 mm; the layup was a symmetric $[0/90]_s$. In Fig. 2.10a we can see an image of the plate instrumented with PWAS.

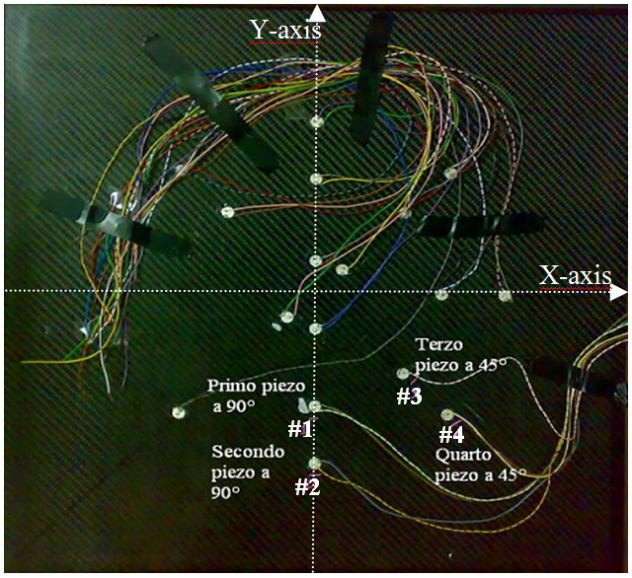

Fig 2.10a – Carbon/epoxy plate used for the impact test

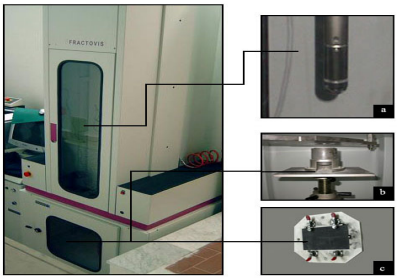

Fig 2.10b – Impact machine CEAST Fractovis

The impact tests were carried out at the Department of Materials Engineering (DIMP) of the University of Naples "Federico II" using the impact machine CEAST Fractovis (Fig. 2.10b), capable to perform impacts involving speeds, in its basic setup, up to 4.6 m/s and involving impact masses up to 70 kg for maximum energies of the order of 700 J.

The plate was impacted at its center and signals were acquired from four PWAS bonded along the negative part of the Y-axis (PWAS #1 and #2) and along the -45° direction with respect to the X-axis (#3 and #4). A number of other PWAS were bonded on the plate for Lamb waves propagation purposes both in the pre and post impact conditions.

In this first test an impact involving penetration was planned for strength characterization since, from the analysis of the behavior of the plate during an impact with penetration, some important features can be extracted: in detail from the time histories of both the contact force and the indentation at the impact location, both recorded during the impact event. The mass involved in the impact test was 8.64 kg and the speed 4.43 m/s, with a resulting kinetic energy, in the first contact instant, of 84.78 J.

Unfortunately the impact caused breakage of the plate due to bending (Fig 2.4b), and not due to local stresses induced only by impact in its location (Fig 2.4a): this caused the failure of the test for material characterization (Fig 2.11). Anyhow the test resulted good for collecting the signals from PWAS during the impact event.

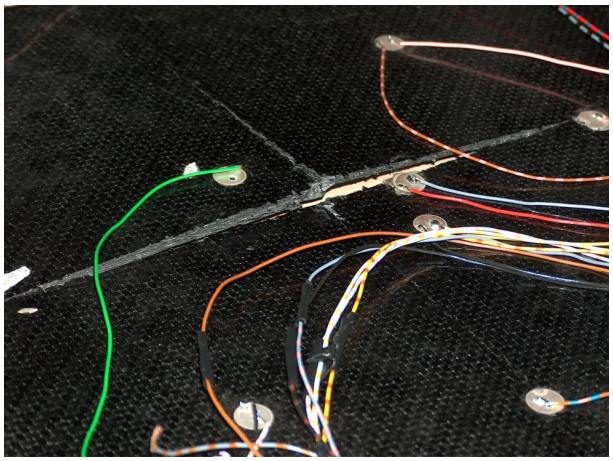

Fig 2.11 – Damage caused by impact of 84.78 J at plate center

The contact force during impact is presented in Fig 2.12.

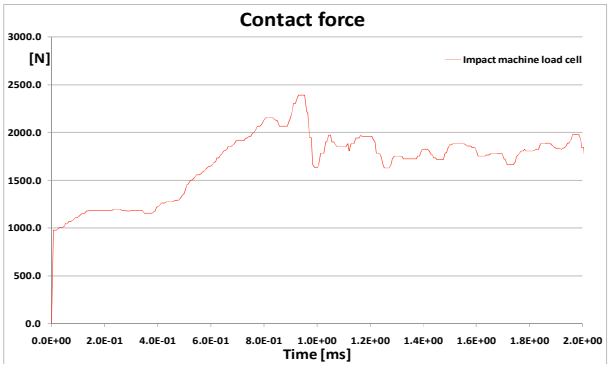

Fig 2.12 – Time history of the contact force during impact

A problem with trigger was found by observing the contact force time history: unfortunately we missed the first part of the curve in the elastic range.
In Fig 2.13 we can see the signals acquired from PWAS during impact, and in Tab 2.3 we can see their coordinates with respect to a reference system having origin at the center of the plate (Fig. 2.10a): the PWAS had distances from the plate center 100mm (#1 and #3) and 150mm (#2 and #4).

Tab 2.3			
PWAS #1 [mm]	PWAS #2 [mm]	PWAS #3 [mm]	PWAS #4 [mm]
{0 , -100}	{0 , -150}	{(√2/2)·100 , -(√2/2)·100)}	{(√2/2)·150 , -(√2/2)·150)}

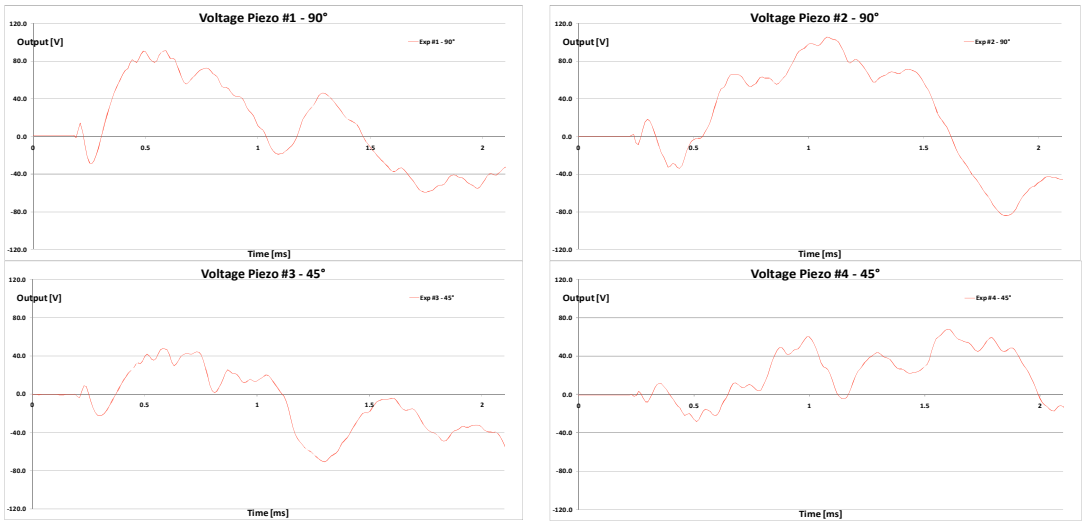

Fig 2.13 – PWAS outputs during impact on carbon/epoxy plate

Since the test for plate's impact strength properties did not give the expected information, we concentrated our attention on the PWAS response, by modeling the same impact experiment with the explicit FEM code LS-Dyna. We only considered the elastic response by using an orthotropic elastic material model (without failure) for modeling composite (Fig. 2.14).

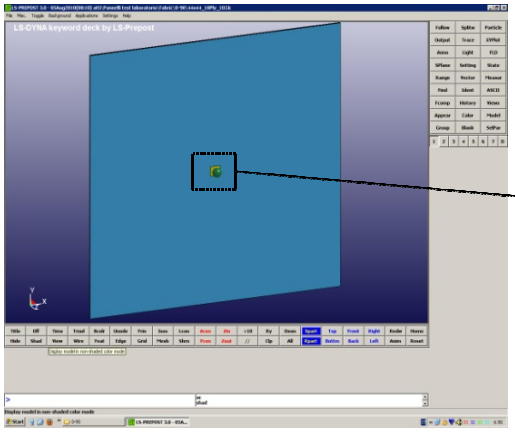

Fig 2.14a – FEM model of the impact event

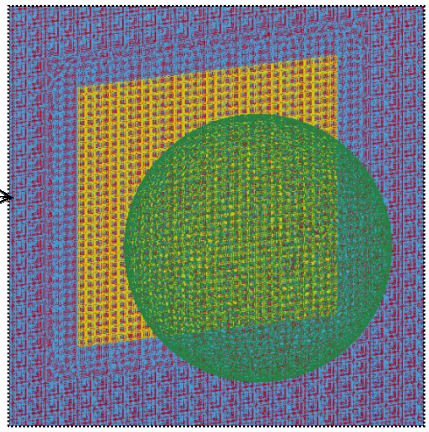

Fig 2.14b – Detail of the impact point

We modeled the plate with 3D brick elements using a non uniform mesh, with smaller elements size at the impact location, and bigger elements size in the regions far away from the plate center (Fig 2.14b); a transition mesh between regions of different refinement levels was designed.

As output from PWAS sensors we considered, in FEM, the same "Numerical Voltage" used for Lamb waves modeling and presented in Par 1.3.3 (Fig. 2.15).

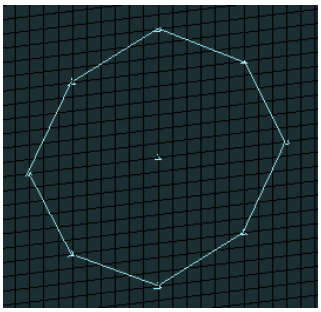

Fig 2.15 – FEM model of PWAS sensor

The results of the FEM analysis, showing the PWAS outputs are presented in Fig. 2.16.

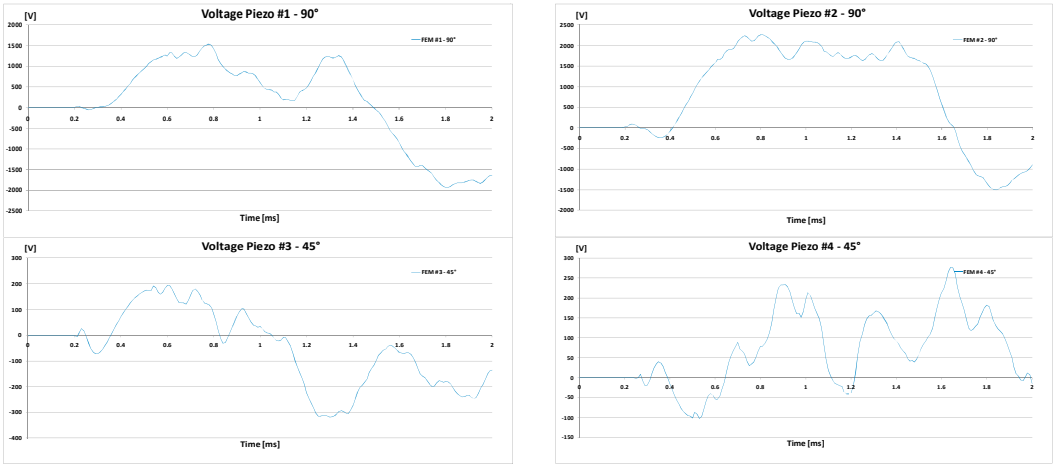

Fig 2.16 – Output of PWAS sensors, from FEM, during impact

The output voltages from FEM were significantly higher than the experimental ones: we then normalized the results, presented in Fig. 2.17.

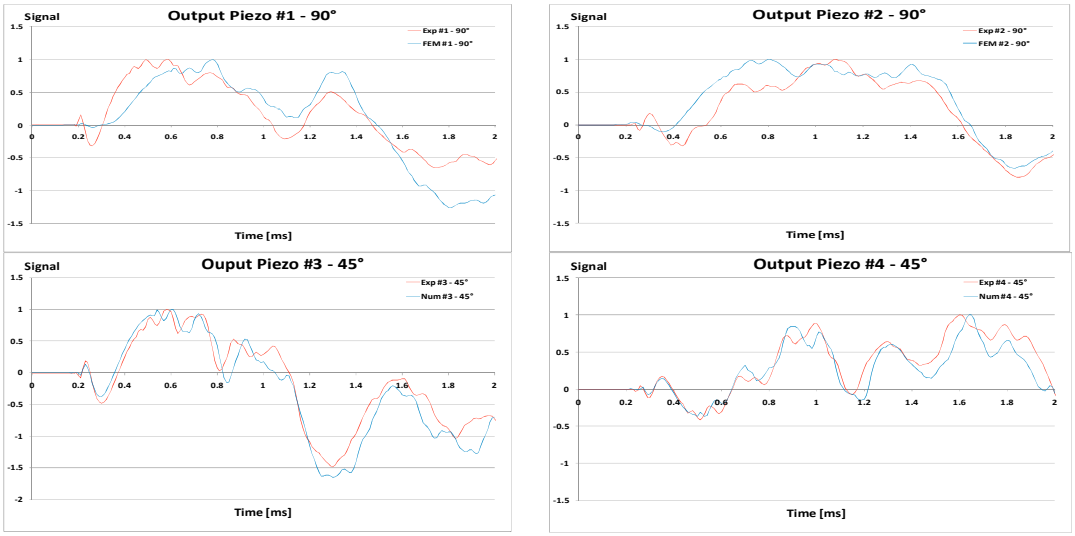

Fig 2.17 – Comparison between experimental acquisitions and FEM from PWAS sensors

From graphs in Fig. 2.17 we can see that the physics of the problem was correctly captured since the output from PWAS in the experiment and from FEM showed the same trend (overlapping curves). The difference in amplitude can be probably attributed to two reasons: firstly the non linearity of the real problem, linearized in our modeling; secondly the PWAS through thickness mode neglected in this first analysis. The reason why we obtained good results using a FEM model that did not include damage could be connected to the time duration of the damage evolution in the experiment, probably higher than the considered time window of 2ms. In our following experiments for PWAS modeling we considered only elastic ranges in the plate dynamics (impacts without failures), plus also taking into account the out-of-plane piezoelectric mode, with significantly better results.

2.4.2 Test on an aluminum plate.

We now present an impact test performed at the 'Laboratory for Advanced Materials and Smart Structures' (LAMSS, University of South Carolina, Columbia SC, USA) led by Prof. Victor Giurgiutiu, known for his advanced studies on piezoelectric materials and Lamb waves propagation [5].

The test involved a 2024-T3 aluminum plate having dimensions: 311 x 610 x 0.82 mm, instrumented with four PWAS sensors (APC-850 disks, diameter 7mm) bonded on the panel. The plate was suspended with elastic copper wires for simulating free boundary conditions (Fig. 2.18).

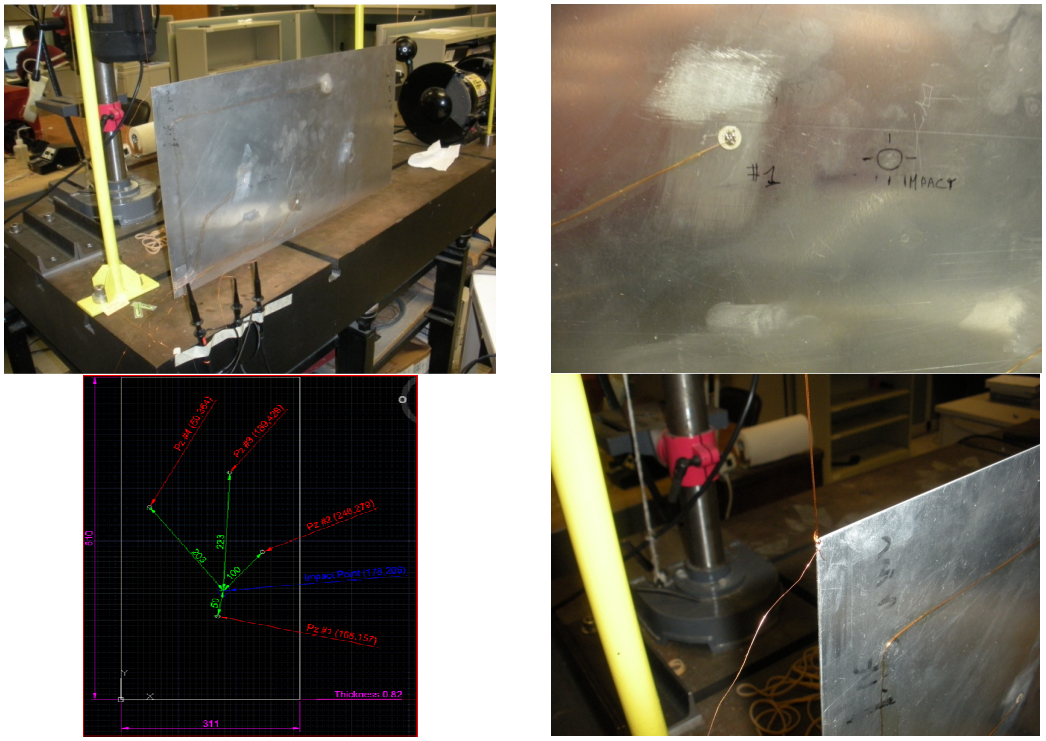

Fig 2.18 – Aluminum plate used for impact test

Fig 2.19 – Impact hammer used for the test: PCB Electronics mod. 086C03

A number of elastic impacts were performed using a PCB Electronics impact hammer, model 086C03 (Fig. 2.19), involving various values of energy, and thus of impact forces. The hammer gave us, as output, the time history of the contact force during impacts, thus allowing us to link the output from PWAS sensors to the applied force. Seven impact tests were performed and the experimental results are presented in Fig. 2.20.

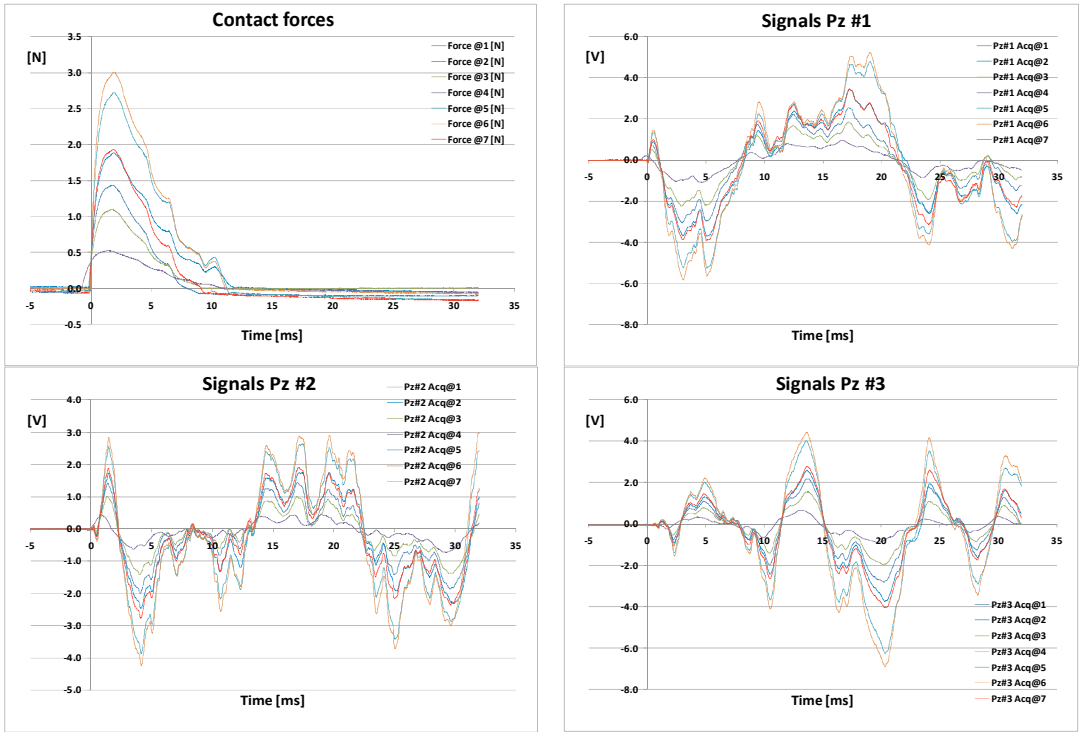

Fig. 2.20 – Experimental results for the impact tests performed on the aluminum plate

As we can see from Fig. 2.20 the contact force ranged from 0.5 to 3 Newtons, so very low energies were involved. The nose of the hammer was made up of soft vinyl (Fig. 2.19), so the stresses induced at the impact location were supposed to be very small with respect to aluminum strength properties: elastic impacts were performed.

Regarding PWAS output, the maximum recorded absolute value was approximately 7 Volts. In Fig. 2.21 we can see the trend of the sensors output with contact force: it was found to be linear with a good approximation.

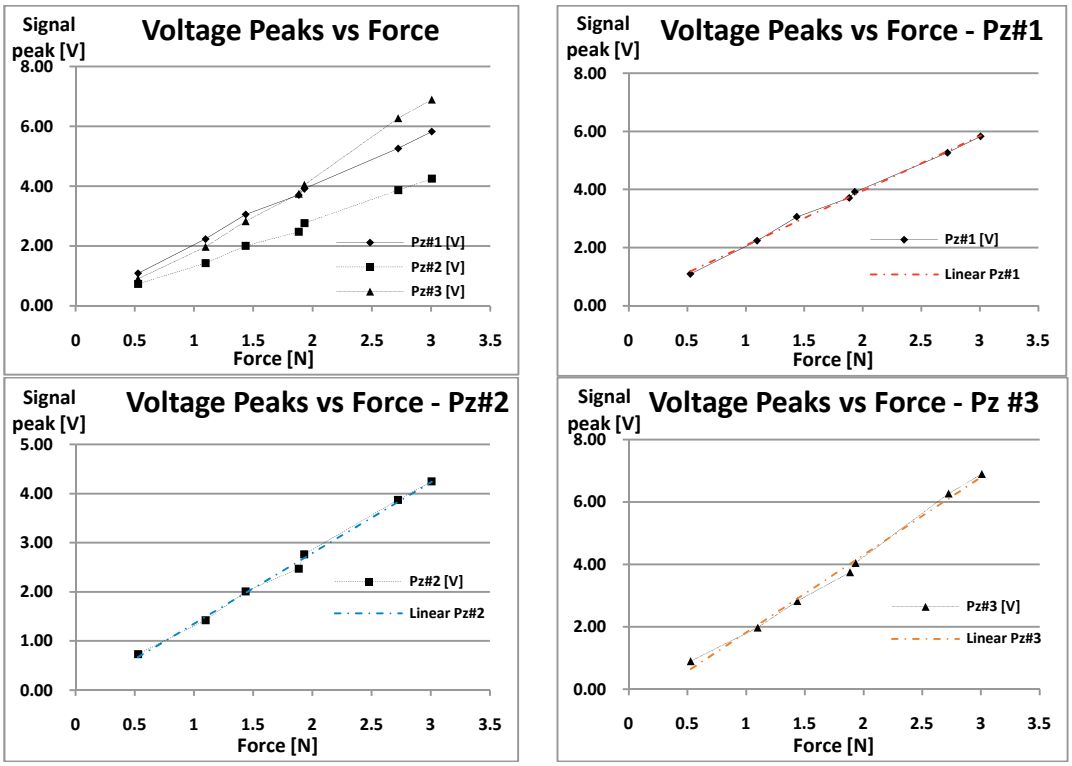

Fig. 2.21 – Maximum values of the signals recorded from PWAS sensors during tests

After performing the experiments, we modeled the aluminum plate with FEM (Fig. 2.22); we used 3D brick elements having dimensions 1x1x0.41 mm^3, thus meshing the plate with 311x610x2 = 379420 brick elements; an isotropic elastic material model was used. The force was applied as a single node vertical load using the curve obtained by the impact hammer during the test number @7 (red curve in Fig. 2.20). The output from sensors was evaluated using the same technique presented in Par. 1.3.3, i.e. modeling a real PWAS with a 2D octagonal surface defined by 8 nodes on the plate, approximating the circular shape of the bonding layer between the plate and the PWAS (Fig. 2.15).

The formula for voltage calculation from FEM is shown here for convenience:

$$\langle 1.16 \rangle \Delta V(t_i) \simeq \frac{th}{2 \cdot d_{31}} \cdot \frac{\Delta A(t_i)}{A_0}$$

In Fig. 2.22b two concentric octagons were defined; it was found they to have, for each time step, substantially the same value of the ratio $\Delta A / A_0$.

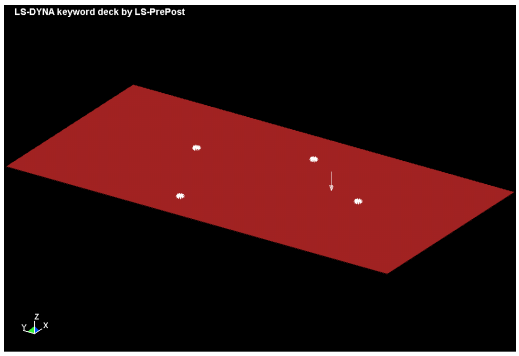

Fig 2.22a – FEM model of the impacted aluminum plate

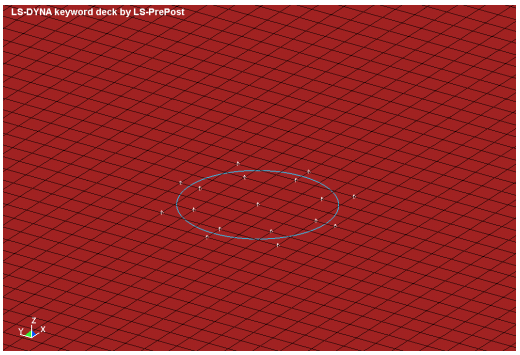

Fig 2.22b – FEM model of PWAS sensors

The time for solution was 2 hours and 20 minutes with a 4-CPU computer (Quad-core AMD Opteron 2GHz, total 32 cores) with 64 Gbytes of RAM; the results for PWAS #1, #2 and #3, after post-processing, are presented in Fig. 2.23.

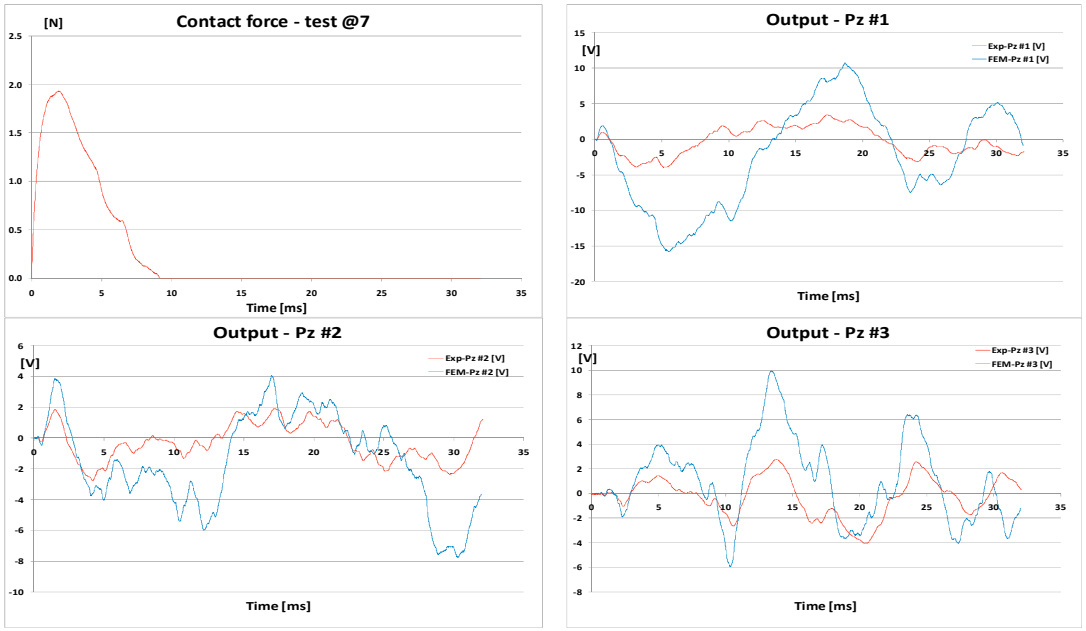

Fig 2.23 – Comparison between experimental acquisitions and FEM solution for the impact on aluminum plate

As in the previous test on carbon/epoxy plate, the waveforms for the three PWAS were correctly captured by the FEM solution, though amplitudes did not match. Let's notice that this time amplitudes were not normalized, and it can be seen a scaling factor approximately equal to 2 between the experimental acquisitions and the FEM solutions: the FEM solution overestimates the experimental acquisitions by a factor two.

We tried this time to better understand why this happened by considering, in addition to the PWAS in-plane deformation: the 'frustum of a cone-like' deformation (due to a difference in the in-plane strains between the upper and lower surfaces of the PWAS

disks), the bending deformation, the through thickness deformation. In order to get this information from FEM we considered a 3D modeling of the actual PWAS disks as we can see in Fig. 2.24.

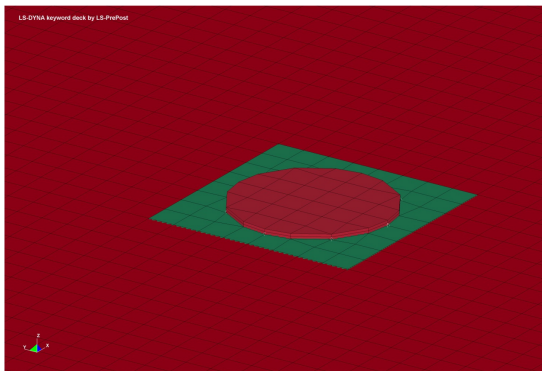

Fig 2.24 – 3D FEM model of a PWAS sensor

All the PWAS elastic material properties were provided by the manufacturer (APC) and we modeled the disks using an orthotropic material model.

Regarding the 'frustum of a cone-like' deformation we considered, in the post-processing phase of the FEM solution, for each time step, the difference between the upper and lower surface area of the modeled PWAS: no considerable difference was measured, so we concluded that the in-plane strains were substantially the same on the lower and upper surfaces.

Regarding bending deformation we evaluated the curvatures of the mid-plane of the disks and they were found to be negligible too. In Fig. 2.25 we can see the trend of curvature radii along X and Y axes for PWAS #1; we can notice that the minimum radius is about 28 meters: very large with respect to the diameter of PWAS disk of 7mm.

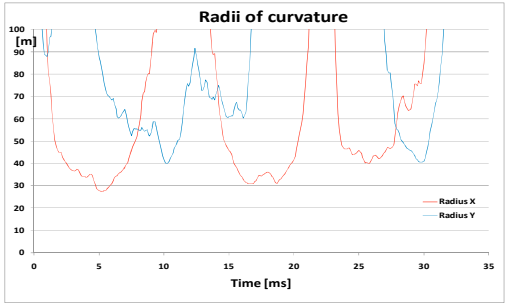

Fig 2.25 – Curvature of the PWAS #1 during impact

On the contrary, regarding through thickness deformation, we found it to be high enough to give an output voltage of the order of Volts! In fact in Fig. 2.26 we can see the time history of the thickness variation (order of nanometers), for PWAS #1, and the corresponding output voltage given by the formula <2.5>:

$$\langle 2.5 \rangle \Delta V_{out-of-plane} = \frac{\Delta th}{d_{33}}$$

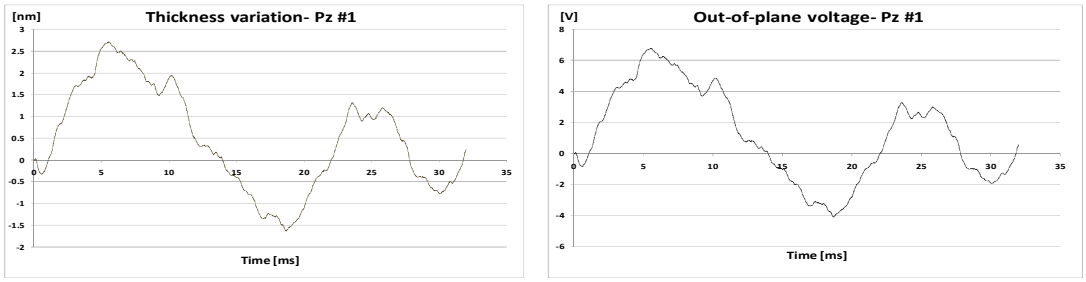

Fig 2.26 – Though thickness-displacement and relative induced voltage for PWAS #1

So the two terms of the total output voltage from sensors, i.e. in-plane and out-of-plane <1.16> and <2.5>, were found to be of the same order of magnitude. We then considered them both as output from FEM and the results are presented in Fig. 2.27.

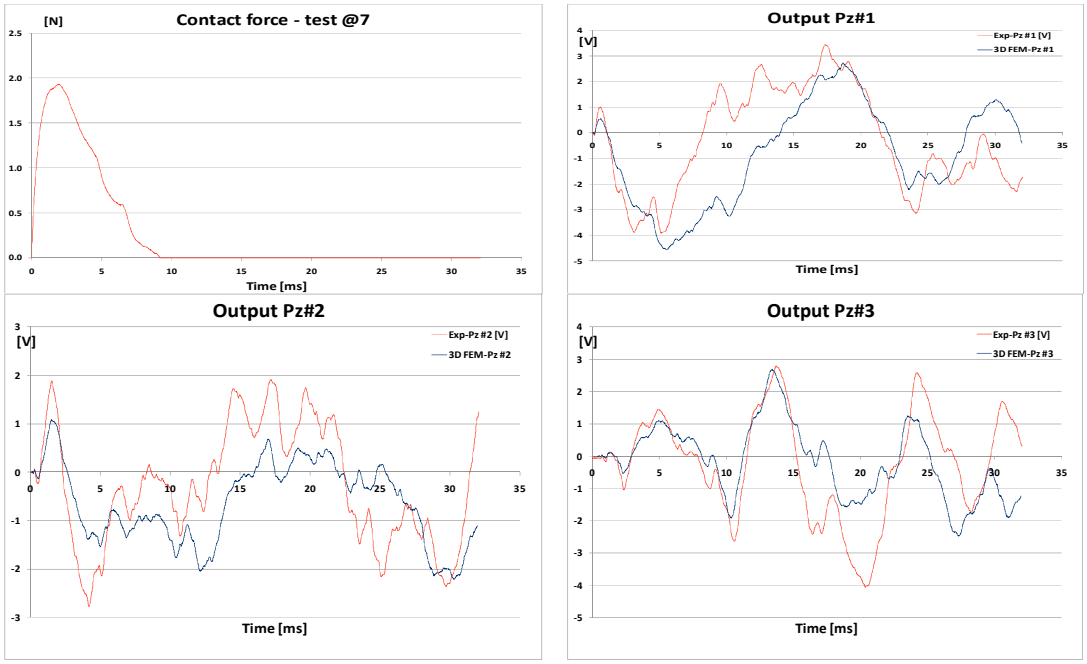

Fig 2.27 – Comparison between the experimental acquisition and the FEM solution for the impact event

As Fig. 2.27 shows now both the trends and amplitudes of the signals from PWAS match with a very good agreement. We then concluded that, for low energy elastic impacts, this zero-order piezoelectric sensors modeling worked fine. We were able to obtain this results with very small computational costs: of the order of some hours. Performing the same analysis involving coupled electromechanical elements, and thus using implicit FEM codes, would have taken probably some weeks.

2.4.3 Test on a fiberglass plate.

The third presented impact test was also performed at LAMSS, USC. The test involved a Norplex-Micarta 'NP130' epoxy/fiberglass plate having dimensions 925x925x3.2 mm^3; some of the material elastic properties (Tab 2.4) were directly evaluated through both tensile tests and ultrasonic waves propagation tests. Note: the value of G_{12} presents a little difference from Par. 1.3.5.

Tab 2.4		
E_1 = 21.05 GPa	E_2 = 22.6 GPa	E_3 = 4.32 GPa
G_{12} = 5.6GPa	G_{13} = 2.8 GPa	G_{23} = 2.95 GPa
ν_{12} = 0.15	ν_{13} = 0.38	ν_{23} = 0.4

The impact tests were performed, as for the aluminum panel in Par 2.4.2, involving the impact hammer (PCB Electronics, model 086C03) and relatively low values of energy, in order to excite only elastic responses of the plate. A large number of PWAS sensors (Steminc SM412, 7mm diameter disks) were bonded onto the structure for Lamb waves propagation purpose but, in this test, only seven of them were used: #1 to #7 (Fig. 2.28).

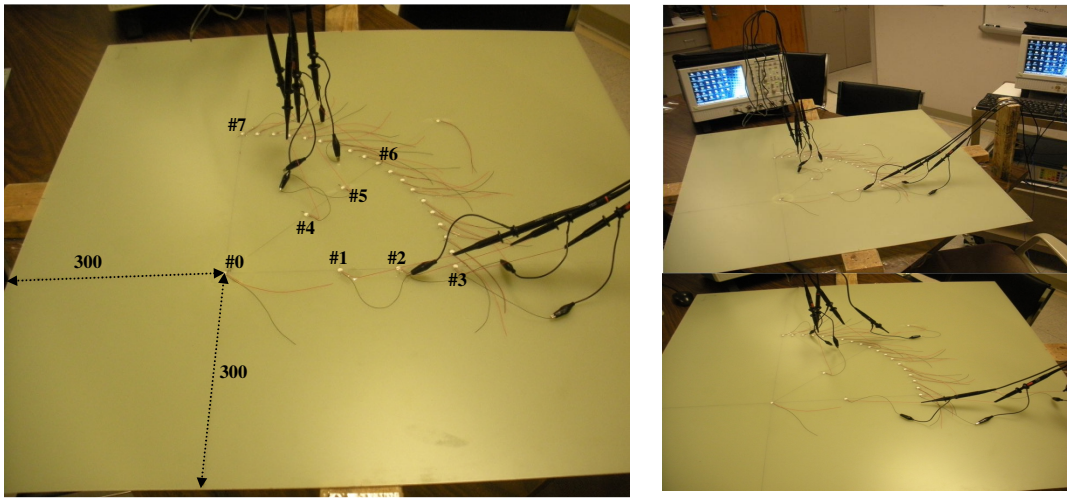

Fig 2.28 – NP130 fiberglass plate used for the impact test

A system of Cartesian axes was defined on the plate: the origin of the X-Y axes was chosen to be coincident with the position of PWAS #0 which is bonded, with respect to the lower-left corner of the plate, at a distance of 300 mm from both the two edges (Fig. 2.28). The impact point was chosen very close to PWAS #0: on +45° direction at 20mm. The PWAS sensors #1, #2 and #3 were bonded on the positive X axis at 150mm, 225mm and 300mm, respectively; PWAS #4, #5 and #6 were bonded on the +45° direction at distances from origin 150mm, 225mm and 300mm; PWAS #7 was bonded on positive Y axis at distance 300mm.

A total of 21 impact tests (from @0 to @20) were performed involving various values of energy; in Fig. 2.29 both the contact forces and the outputs from three sensors are presented, for ten of the impact tests; the corresponding curves 'Force-Max Voltage' in Fig. 2.30 were obtained by considering the first 5 ms of the time histories.

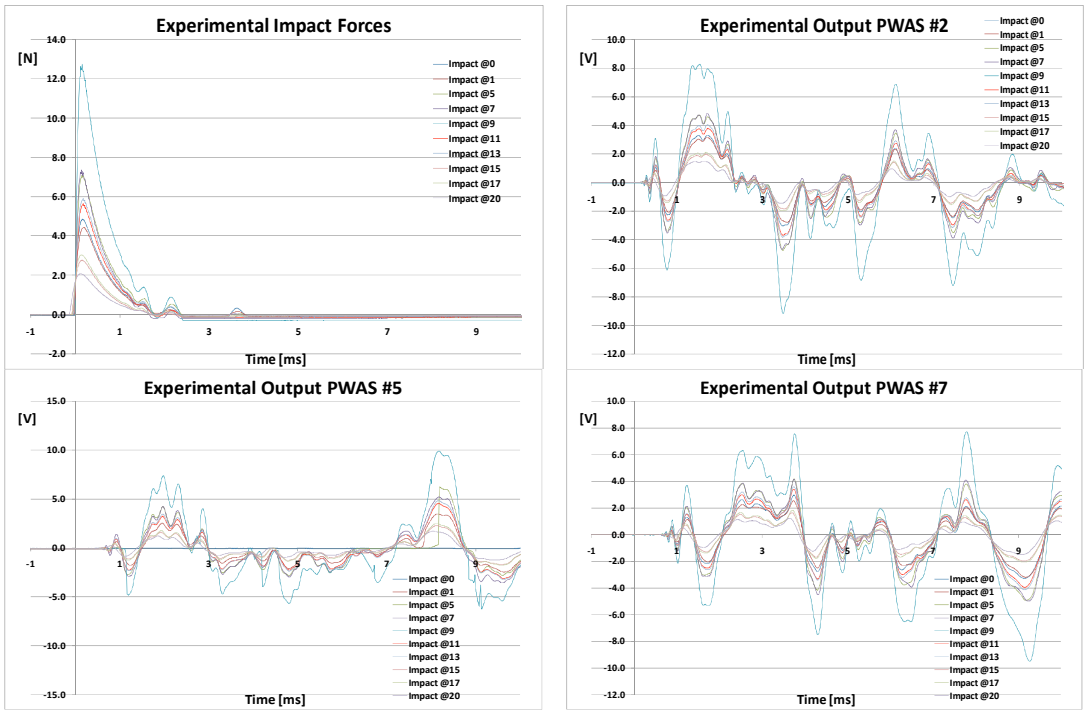

Fig 2.29 – Experimental results for impact on NP130

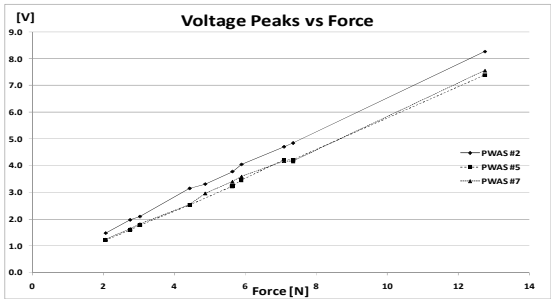

Fig 2.30 – Max output from PWAS sensors versus contact force

After performing the experiments we modeled with FEM the same impact event using the same technique as for the aluminum plate (Par. 2.4.2), i.e. by exciting the plate with the contact force curve from test @11 (red curve in Fig. 2.29). The plate was modeled using 3D brick elements having dimensions 2x2x1.6 mm^3, the PWAS were modeled with a non uniform mesh (Fig. 2.31).

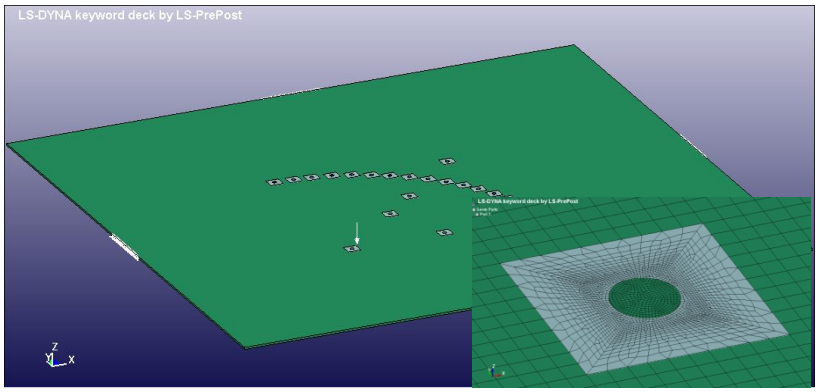

Fig 2.31 – FEM model of the NP130 plate used for the impact tests

By post-processing the FEM results we obtained the PWAS output voltage, presented in Fig. 2.32.

Fig 2.32 – Comparison between experimental data and FEM solution for the impact test on the NP130 plate

As we can see in the graphs in Fig. 2.32 all the general trends of the experimental curves were captured by the FEM, showing a good approximation also for the amplitudes: the numerical solution only seems to slightly underestimate the real output voltage. We can then conclude that we have an excellent technique for simulating output from PWAS disk sensors, during impacts, with a very small computational cost.

3. STRUCTURAL HEALTH MONITORING WITH LAMB WAVES.

3.1 Introduction.

In plate like structures almost all kind of damage such as cracks, holes, material losses and, specifically for composites, delaminations, fiber fractures and breakages, matrix cracking and interfacial debondings are identifiable by Structural Health Monitoring (SHM) strategies involving the Lamb waves [5] [7] [15]. The general concept is that an ultrasonic wave, traveling in thin walled structures, propagates undisturbed as long as no obstacles are present on its path, whereas, if any of the above-mentioned damage appears, it is typically reflected, diffracted, and also mode conversions might occur. The obstacle or discontinuity can also be represented by a structural component that is part of the structure, such as a rivet hole, a stiffener or a change in thickness. By the theoretical point of view, any kind of damage can be detected by the ultrasonic technique involving Lamb waves, through the choice of the correct frequency for the specific case. Typically the size of a damage correctly localized through Lamb waves is comparable with the wavelength which is, for frequencies in the hundreds of kHz, of the order of centimeters using S_0 (zero order symmetric Lamb waves) and of the order of millimeters using A_0 (zero order antisymmetric). Indeed the wavelength of an S_0 wave propagating in an aluminum plate of 1mm thickness, at a frequency of 125kHz, is about 4cm, while for an A_0 wave, at the same frequency, is about 9mm. Various studies on the appropriate excitation frequency can be found in literature [8] [5].
Since Lamb wave based SHM was introduced, several approaches have been developed in this area. A first classification can be carried out by considering the methodology for Lamb wave exciting and sensing. In the area of contact tomography, which involves the use of standard ceramic piezoelectric transducers for both exciting and receiving guided waves, a further division can be made by considering the methods of diagnosis for damage identification, each of them exploiting different aspects of the interaction between Lamb waves and the damage itself. All these methodologies can be grouped in three main categories: 'Time of Flight' techniques [17], 'Propagation Paths' techniques [7] [18] and 'Echo' techniques [19]. Of course the distinction is not clear and there may be hybrid approaches.

3.2 Damage localization techniques.

3.2.1 Time of Flight technique.

For the Time of Flight (T-o-F) technique a non linear system of equations, one for each sensor, is considered involving: the sensor positions, the speeds of waves, and time intervals derived from the analysis of the acquired signals. Substantially, for each sensor, a time interval is defined as the difference between the arrival time of the Lamb wave directly traveling from the actuator to the sensor, and the eventual arrival time of the wave reflected from the damage (Fig. 3.1).

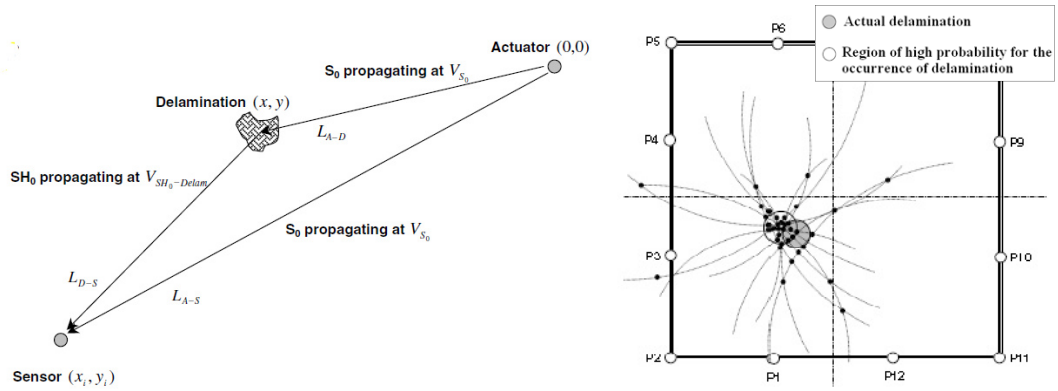

Fig 3.1 – Time of Flight damage localization method

The system of equations, geometrically represented by the curves in Fig. 3.1, is given by:

$$\langle 3.1 \rangle \left(\frac{L_{A-D}}{V_{S_0}} + \frac{L_{D-S}}{V_{SH_0-Delamin}} \right) - \left(\frac{L_{A-S}}{V_{S_0}} \right) = \Delta T_{1-i} \quad (i = 2,3,...,n_{sens})$$

Since the system <3.1> is not linear and moreover overdetermined, the solution is not unique: a region of high probability of presence of damage is derived (Fig. 3.1).
The main advantage of this technique is that we can localize with high precision, of course depending on the number of sensors, the damage and eventually its extension. Conversely the limits of such a technique are essentially two. The first problem concerns the eventual presence, in the time series, of reflections due to factors different from damages, i.e. edges and/or other structural components anchored onto the structure. Another problem is due to multimodal behavior of the Lamb waves: for values of frequency-thickness from 0.01 to 0.5 MHz*mm the symmetric and antisymmetric Lamb wave modes coexist, plus presenting different propagation speeds. Because of this it is difficult to understand if the waves arriving at a sensor location include reflections, or if they are expression of the multimodal nature of Lamb waves. To overcome this problem a number of studies have been carried out on frequency tuning: i.e. using the "sweet spot" frequency [8].

3.2.2 Propagation Paths technique.

A second class of methods considers the perturbation that a damage, eventually present along the propagation paths of the Lamb waves, induces on the signals registered at sensors locations. Two sets of acquisitions are involved in the analysis: one performed in the pre-damage condition, and the other one in the post-damage condition; from the comparison between these two sets of signals, areas with high probability of presence of damage are eventually identified [7]. In detail a Damage Index (***DI***) is defined involving the two sets of signals, $\boldsymbol{Y_{pre}}^{\boldsymbol{k}}$ and $\boldsymbol{Y_{post}}^{\boldsymbol{k}}$, acquired, for every actuator-sensor path, in pre and post damage conditions. The ***DI*** can be defined both in time or frequency domains, and a typical form is represented by Eq. <3.2>:

$$\langle 3.2 \rangle \; DI^k = \left| 1 - \frac{\left\| Y^k_{post} \right\|}{\left\| Y^k_{pre} \right\|} \right|, \; k = 1..N; \; N \text{ number of actuator-sensor paths}$$

The intersection of paths presenting highest values of ***DI*** identifies the damage position (Fig. 3.2).

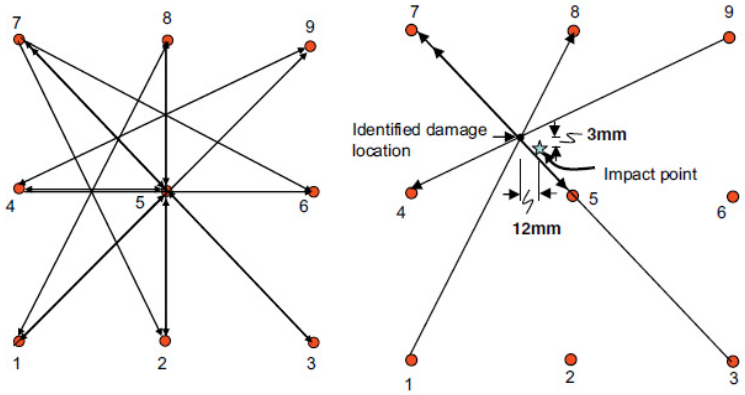

Fig 3.2 – Propagation paths damage localization method

A significant advantage of this technique regards its insensitivity to the conditions on the edges, and to components anchored on the surface of the panel. Conversely a delicate point of such a technique is related to the ability to purify as much as possible the signals from background noise, which, for reasons inherent in the methodology, is a strong source of disturbance.

3.2.3 Echo technique.

The last class of techniques uses every single transducer both as actuator and sensor at the same time. From the time required by the ultrasonic wave to return to the starting point, after being reflected by the damage, a circumference is defined for each sensor. From intersection of these circumferences, one for each transducer, the damage is localized.

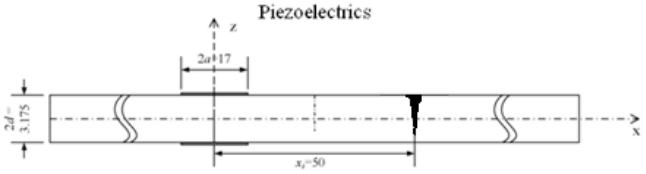

Fig 3.3 – Echo technique for damage localization

A summary of the presented techniques is shown in Tab. 3.1.

Tab. 3.1	Advantages	Disadvantages
Time of Flight	Accurate localization of damage	Problems with edges and other structural components anchored on the plate; problems due to multimodality of Lamb waves
Propagation Paths	Insensitivity to boundary conditions	Background noise strongly penalizing for accuracy of damage localization
Echo	Simple data elaboration	Problems with edges

3.3 Test on an aluminum panel.

3.3.1 Phased array technique.

We now present a numerical-experimental test for damage localization on an aluminum plate. The experiment was first modeled using FEM, for then performing experimental acquisitions and post-processing of the data for identifying a damage present on the plate [28]. For damage localization we used a technique involving two sets of Lamb waves acquisitions: the first set of acquisitions were performed in the safe condition (without damage), while the second set in the damaged condition. The processing of data consisted in the introduction of a Damage Index (***DI***) for comparing the two plate conditions: pre- and post-. The introduced DI, <3.3>, highlights the difference between two signals in the frequency domain, and it has a null value if the two signals are identical; on the contrary the higher is the difference of the two signals, the higher is the value of ***DI***:

$$\langle 3.3 \rangle \; DI = \left| 1 - \frac{\sum_{f_k} \left\| Y_{Post-damage}\left(f_k\right) \right\|}{\sum_{f_k} \left\| Y_{Pre-damage}\left(f_k\right) \right\|} \right| \; ; \; Y\left(f_k\right) \text{ Coefficients of the discrete Fourier transform}$$

As experimental setup we considered a 6061-T6 aluminum plate, having dimensions 1000x1000x1 mm^3, instrumented with a number of PWAS transducers for Lamb waves generation and acquisition; a hole with edge cracks was drilled to simulate a damage.
For damage localization with Lamb waves we used the phased-array technique, i.e. through the generation of a beam of waves that allowed us to scan the plate as a radar. The operating principle of phased array is based on constructive-destructive interference between the ultrasonic waves generated by different actuators that enables to generate and direct the beam. This is achieved through an appropriate time-shifting of the exciting signals sent to the various PWAS actuators. The time-shift of the exciting signal sent to the m-th PWAS disk actuator, for a 1D-linear phased array, is directly linked to the angle of the beam through the relation <3.4> [5]:

$$\langle 3.4 \rangle \; \Delta_m = m \frac{d}{c} \cos\left(\phi_0\right) \; ; \; m = 1..\left(M-1\right)$$

with $\boldsymbol{M}$ total number of PWAS actuators, $\boldsymbol{d}$ center-to-center distance between PWAS, $\boldsymbol{c}$ wave speed, and $\boldsymbol{\phi_0}$ steering angle of the beam (Fig. 3.4).

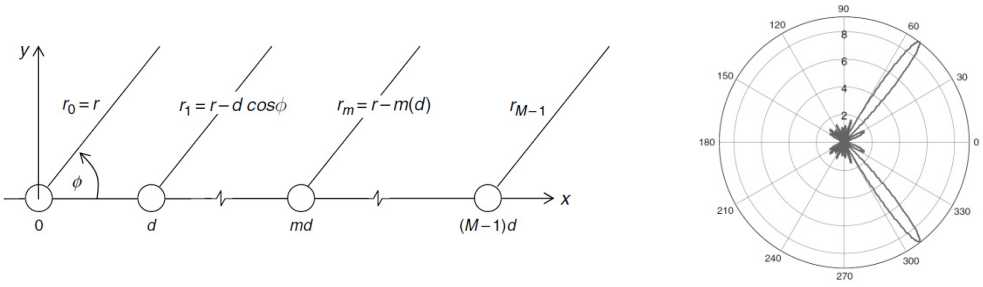

Fig 3.4 – Phased array for Lamb waves beam forming

Let's notice that, using a 1D-linear PWAS phased array (Fig. 3.4), two wave lobes are present: at $\pm\ \boldsymbol{\phi_0}$.

3.3.2 FEM modeling.

Before performing the test on the real 6061-T6 aluminum plate, we previously modeled a similar experiment with FEM. A 1D-linear array of 9 PWAS disks of diameter 10mm (PI Ceramic, PIC-255), located at plate's center, was modeled using FEM, for beamforming of Lamb waves; other 9 PWAS sensors were modeled close to boundaries. The distance between two PWAS of the array was $\boldsymbol{d}$ = 12mm (Fig. 3.4), the distance of the PWAS sensors from edges was $\boldsymbol{d_{edges}}$ = 80mm, while the distance between them was $\boldsymbol{d_{sensors}}$ = 105mm (Fig. 3.5); 4.5 sine cycles curve with Hanning window (Fig. 1.6) at frequency 225kHz was chosen as exciting signal, thus obtaining a phase velocity of the generated S_0 wave packet: $\boldsymbol{c_{ph}}$ = 5347m/s ≈ $\boldsymbol{c_g}$ = 5340m/s. The FEM modeling of the plate involved 3D elements (bricks) and the analysis was performed using the explicit code LS-Dyna. The plate was modeled using 2000x2000x4 = 16 millions of elements, since the bricks dimensions were: 0.5x0.5x0.25 mm^3; the simulations were carried out involving various steering angles of the beam: 30°, 45°, 60°, 75° and 90°.

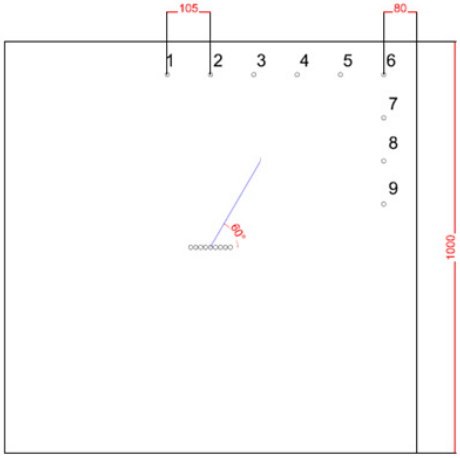

Fig 3.5a – Sketch of the aluminum plate

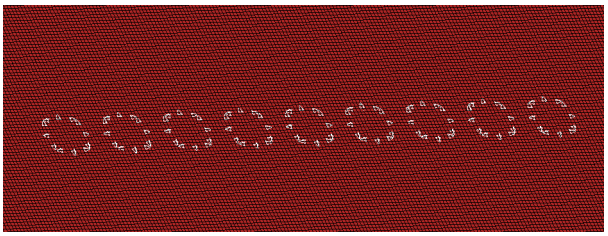

Fig 3.5b – FEM modeling of the PWAS phased array

The plate was firstly modeled in its intact condition, and Lamb waves propagation simulations were performed at the various steering angles by time-shifting the loads at actuators locations (Fig 3.5b); the signals from the PWAS sensors were then post-processed. After this a new FEM analysis was performed in the damaged condition by modeling a crack on the plate: it consisted in a 5mm hole with two notches of 7mm on two sides (Fig. 3.6.b) located, with respect to phased array, at an angle of 60° and distance s_{crack} = 250 mm (Fig. 3.6.a); the crack was oriented perpendicularly to the line connecting it and the phased array center. The geometry of the damage considered simulates a rivet hole from which two side cracks are developed.

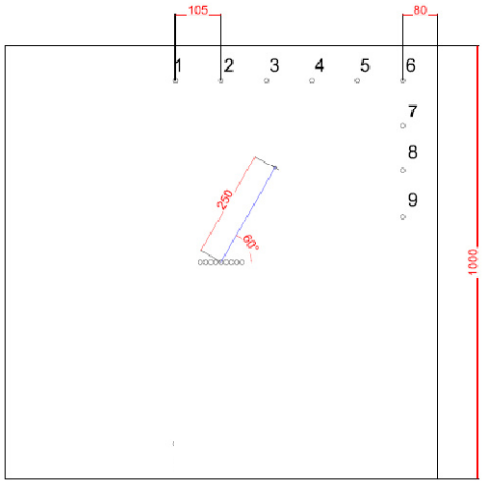

Fig 3.6a – Position of the crack on the aluminum plate

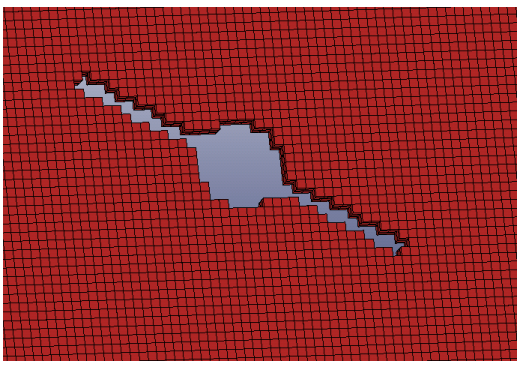

Fig 3.6b – FEM modeling of the crack

In Fig. 3.7 we can see a contour plot of the Von-Mises stresses (FEM solution), for the damaged plate, with beam's steering angle of 60°: the Lamb waves beam encounters the crack.

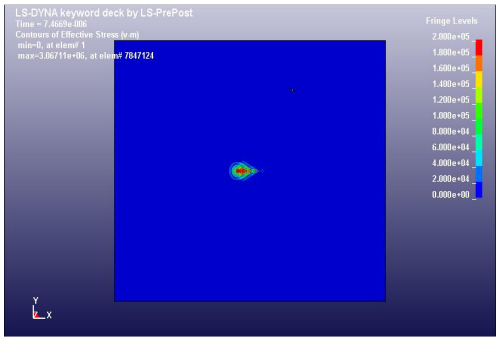

Time = 7.5 μs

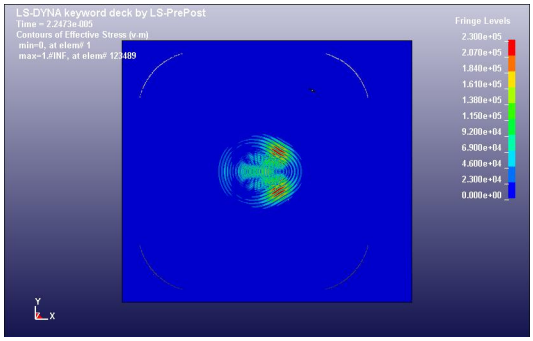

Time = 22.5 μs

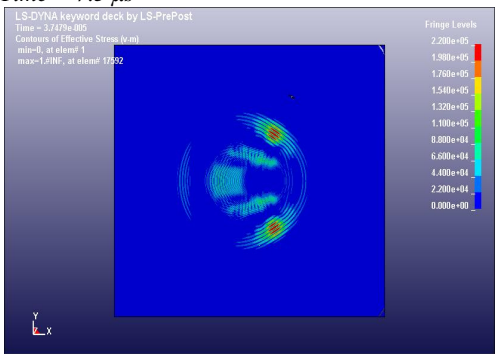

Time = 37.5 μs

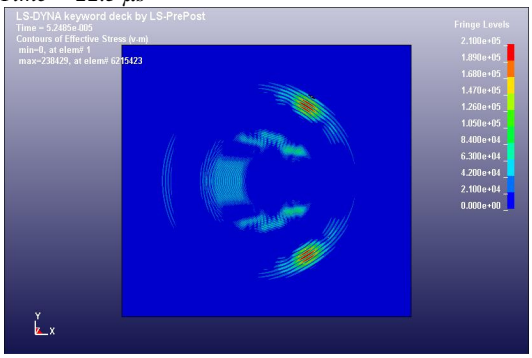

Time = 52.5 μs

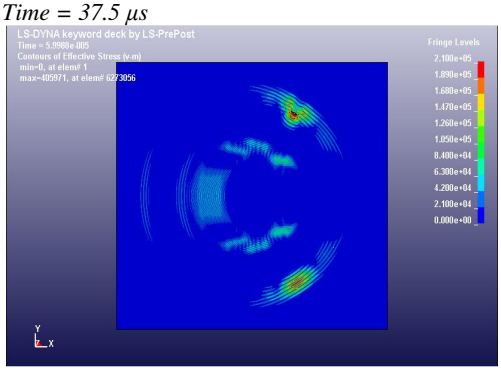

Time = 60 μs

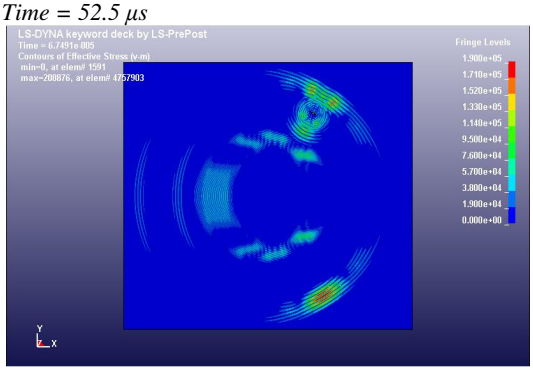

Time = 67.5 μs

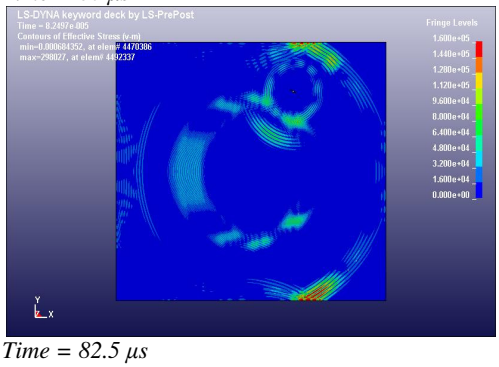

Time = 82.5 μs

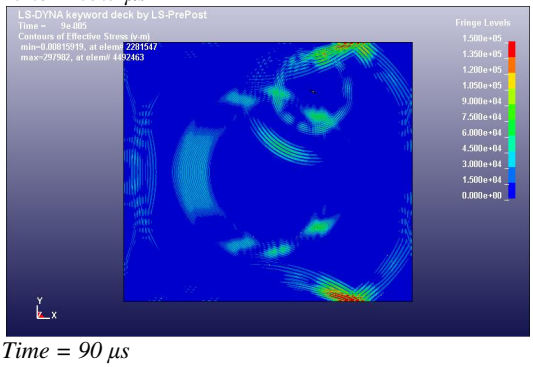

Time = 90 μs

Fig 3.7 – Contour plots of Von Mises stresses from the FEM solution

As we can see both in Fig. 3.7 and 3.8a, part of the beam is reflected back and propagates toward the PWAS array; reflections are also visible at plate's edges (Fig. 3.8b).

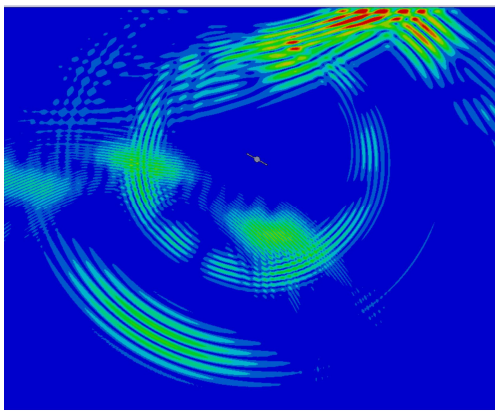

Fig 3.8a – Stresses distribution around the crack

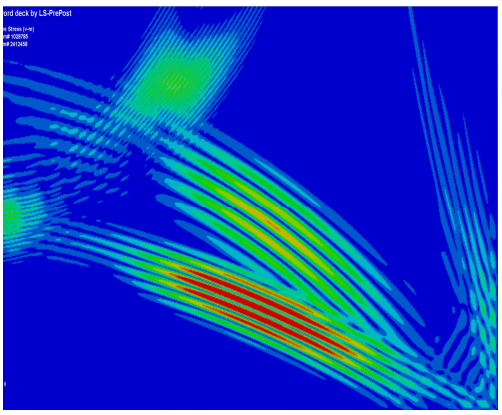

Fig 3.8b – Reflections at edges of the plate

From the arrival time of the reflected beam, sensed by the PWAS array (transducers used as sensors in this case), we can measure the distance of the crack as the propagating speed is known, whereas from the signals acquired by sensors close to the edges we can calculate its angular position. The distance of the crack from the center of the array can be calculated through the relation:

$$\langle 3.5 \rangle \; d_{crack-FEM} \simeq \frac{1}{M} \sum_{m=1}^{M} \left(\frac{c}{2 \cdot \Delta t_m^{\text{t-o-f}}} \right)$$

where $\Delta t_m^{\text{t-o-f}}$ is the time-of-flight of the beam, measured by the m-th PWAS disk. Time-of-flight was calculated through a wavelet analysis of the signals: $\boldsymbol{d_{crack\text{-}FEM}}$ was found to be 251 mm, so very close to the exact value $\boldsymbol{s_{crack}}$ = 250mm. Regarding the angular position of the crack we introduced the signal energy definition, or "Intensity" (***I***), of the PWAS signals from the FEM, for the sensors nearby the edges:

$$\langle 3.6 \rangle \; I_k = \sum_i \left[\left(\Delta A_i^k \right)^2 \cdot \Delta t_i \right]$$

with ΔA_i^k variation of the area of the ***k***-th 'sensor-octagon' (Par 1.3.3), for ***i***-th time-step. Let's consider that the introduced parameter $\boldsymbol{I_k}$ defined by <3.6>, through <1.16>, can be linked to voltage simply by multiplying it by a constant involving geometry and electromechanical properties of the PWAS disks.
In Fig. 3.9 we can see the values of the Intensity ***I*** at all sensors positions, for the various steering angles, for both cracked and un-cracked plate.

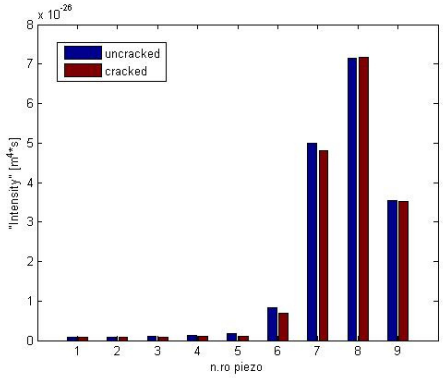

Steering angle: 30°

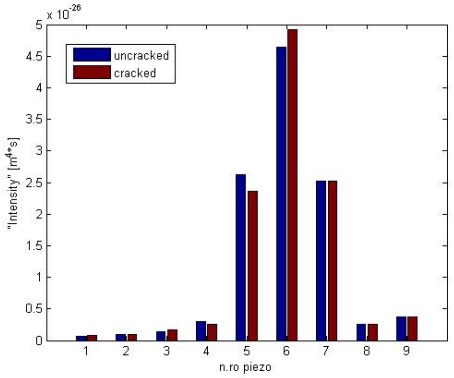

Steering angle: 45°

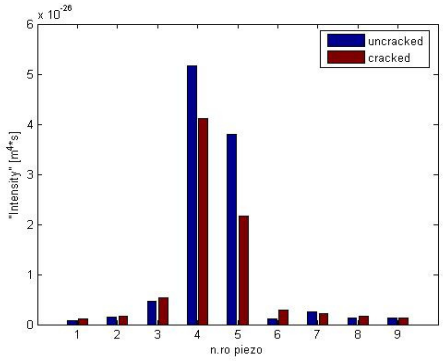

Steering angle: 60°

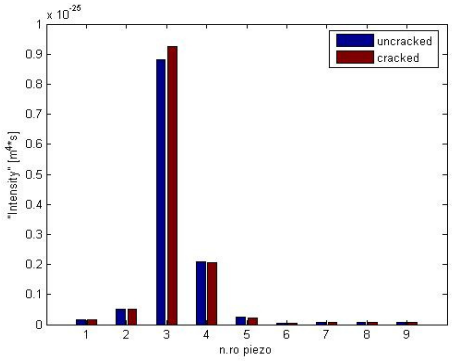

Steering angle: 75°

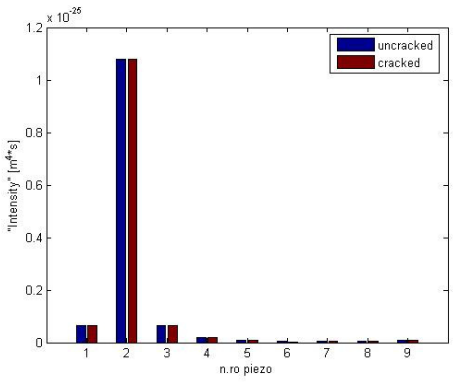

Steering angle: 90°

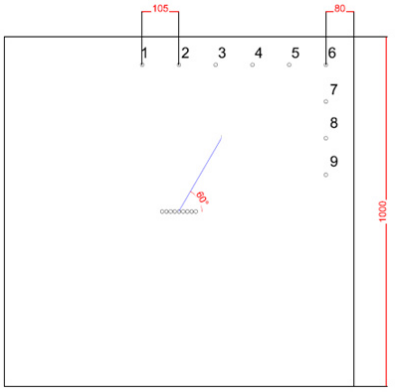

Panel's sketch.

Fig 3.9 – Intensity evaluation at sensors positions, for the various steering angles

By considering the Damage Index (***DI***) defined by the relation:

$$\langle 3.7 \rangle \; DI_k = \left| 1 - \frac{I_k^{Post}}{I_k^{Pre}} \right| \;\; ; \;\; k = 1..9$$

we obtained the results presented in Fig. 3.10.

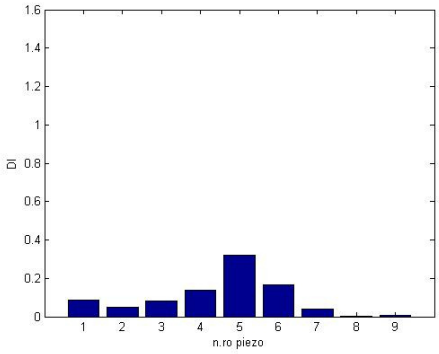

Steering angle: 30°

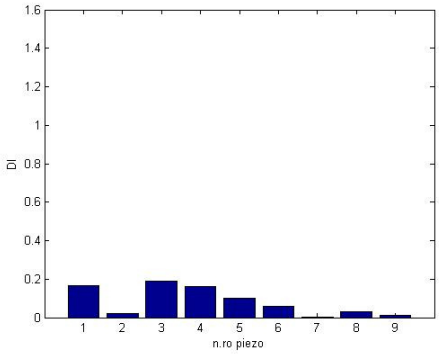

Steering angle: 45°

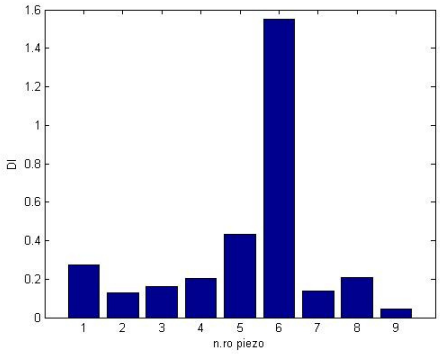

Steering angle: 60°

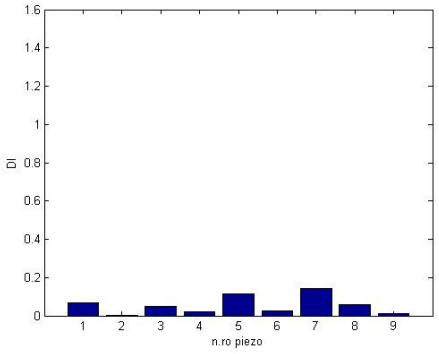

Steering angle: 75°

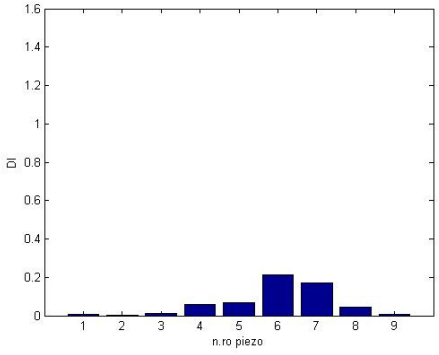

Steering angle: 90°

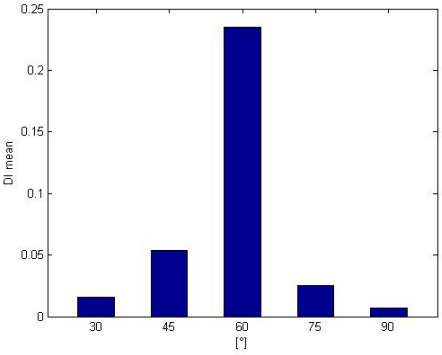

DI mean value at the various steering angles.

Fig 3.10 – Damage Index evaluation at the various steering angles

From graphs in Fig. 3.10 we can see that highest values of ***DI***, registered at sensors locations, corresponded to the steering angle of 60°, which is the angle of the line connecting the PWAS array and the damage: this is clear in the last graph of Fig. 3.10 where main values of ***DI*** at the various angles are shown.

3.3.3 Experimental setup.

After setting up the technique for crack localization using FEM, we passed to experiment involving the real aluminum plate (Fig. 3.11), for validating the obtained results.

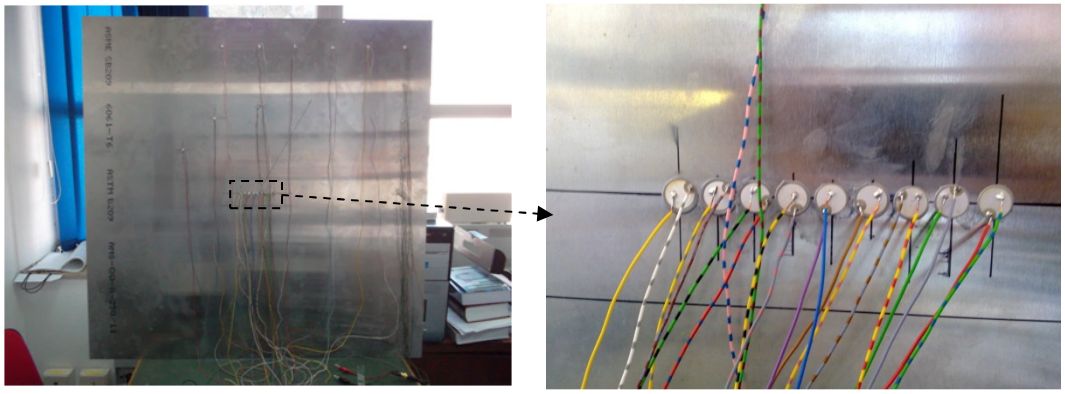

Fig 3.11 – Aluminum plate used for the damage localization test

We considered a 6061-T6 aluminum plate, 1000x1000x1 mm^3, and we bonded, at its center, a 1D-linear PWAS array with the same properties as in FEM model: 9 disks of diameter 10mm (PI Ceramic, PIC-255) with 12mm the center to center distance between them (Fig. 3.11). Nine sensors, as in FEM, were also placed nearby edges, precisely at distance 105mm between them and 80mm from plate's borders (Fig 3.12). As exciting signal we considered the 4.5 sine cycles curve with Hanning window at 225kHz.

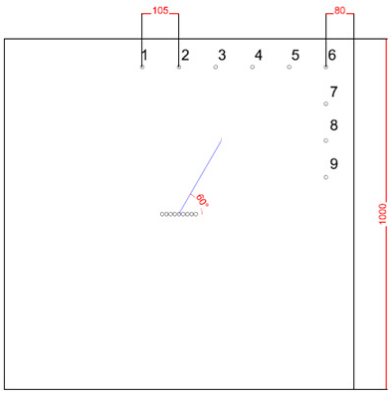

Fig. 3.12 – Sketch of the aluminum plate

For simulating the time-shifts of the signals sent to the various PWAS actuators, in order to simulate the Lamb waves beam forming, we used a Round Robin technique [5], substantially using a superposition principle:

1) we excited one by one the PWAS of the array and collected all the signals at sensors positions;
2) we then combined the collected signals, for each one of the sensors, by adding the appropriate time-shift in the sum process;

After registering all the Lamb waves signals in the pre-damage condition of the plate, we drilled a hole at a distance of 250mm from PWAS array, and angle 60°: the hole was 10mm long and 3mm wide (Fig. 3.13).

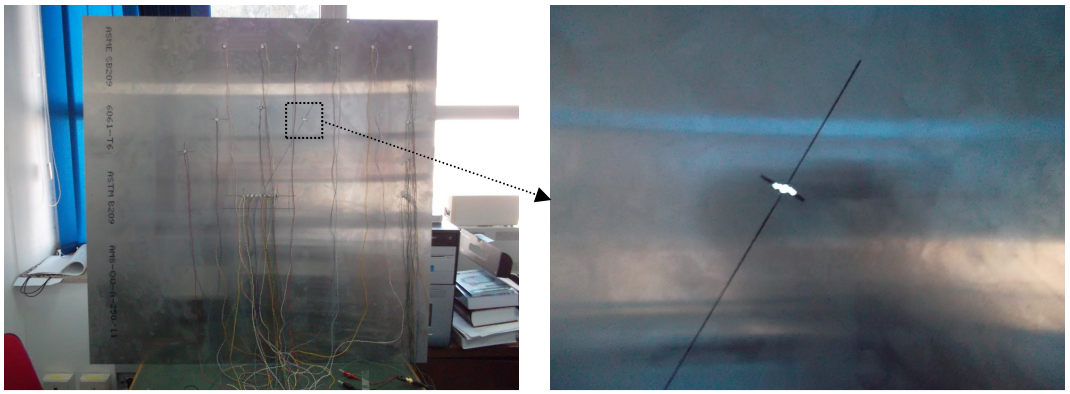

Fig 3.13 – Aluminum plate in the damaged condition: a hole was drilled

After performing a new acquisition in the damaged condition we carried out the same analysis as in the FEM simulation, i.e. by introducing the intensity $\boldsymbol{I_k}$ of signals:

$$\langle 3.8 \rangle \; I_k^{(V)} = \sum_i \left[\left(V_i^k \right)^2 \cdot \Delta t_i \right]$$

As Damage Index ***DI*** we used the same as in FEM modeling:

$$\langle 3.7 \rangle \; DI_k = \left| 1 - \frac{I_k^{Post}}{I_k^{Pre}} \right| \quad ; \quad k = 1..9$$

In Fig. 3.14 and 3.15 the results of the analysis of the experimental data are shown.

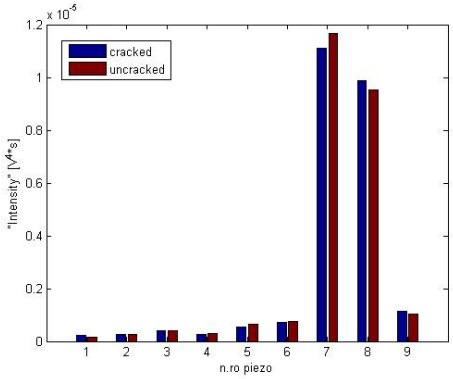

Steering angle: 30°

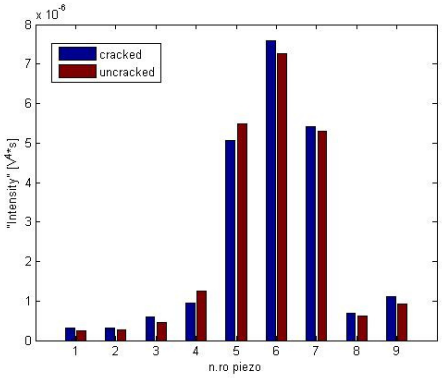

Steering angle: 45°

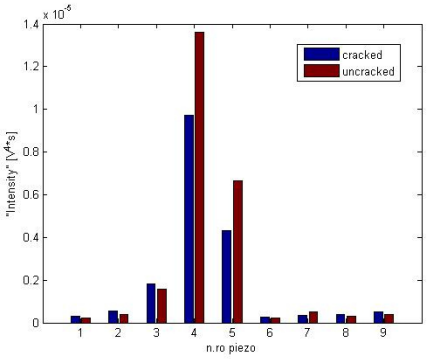

Steering angle: 60°

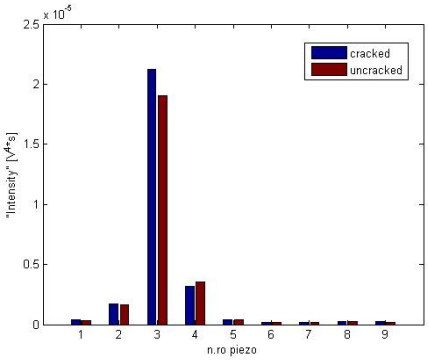

Steering angle: 75°

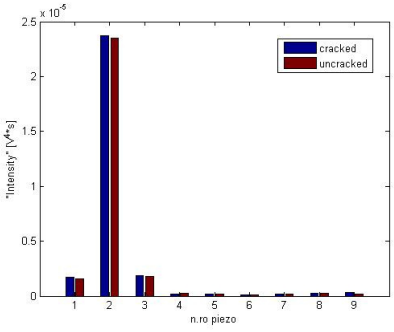

Steering angle: 90°

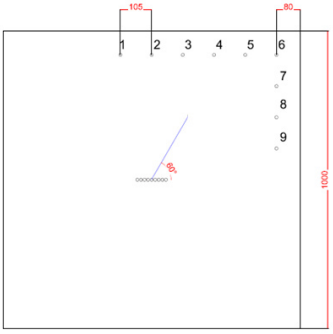

Panel's sketch

Fig 3.14 - Intensity evaluation at sensors positions, for the various steering angles (note: there is a typo on Y axes: V^2*s)

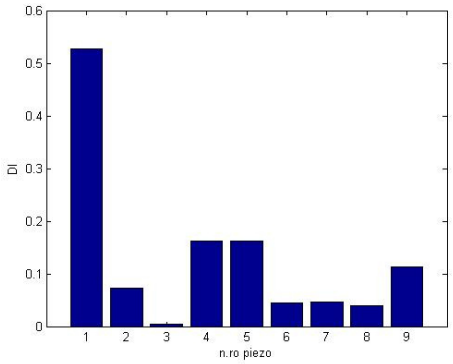

Steering angle 30°

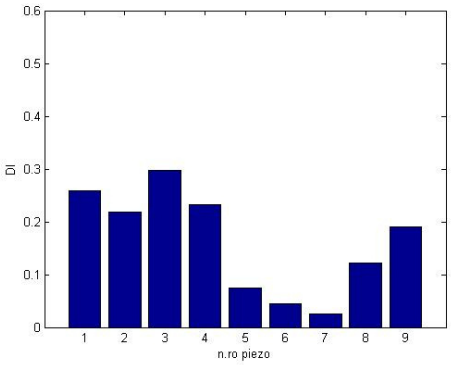

Steering angle 45°

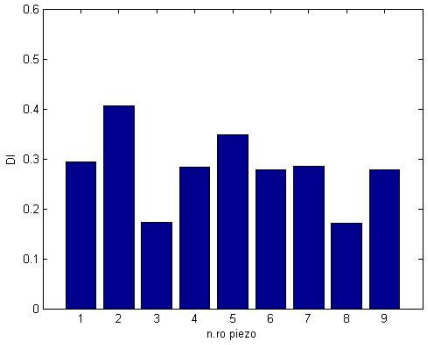

Steering angle 60°

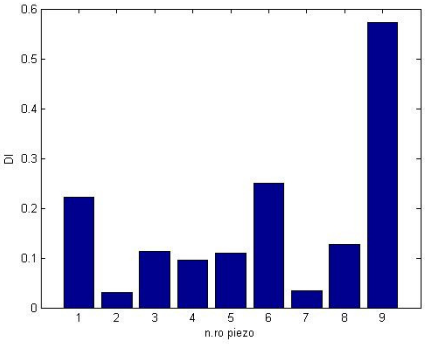

Steering angle 75°

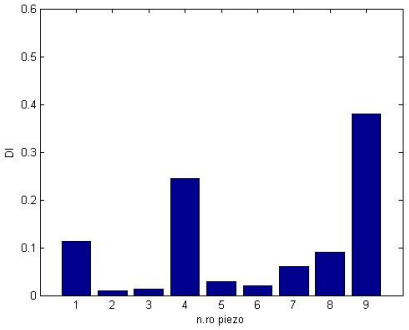

Steering angle 90°

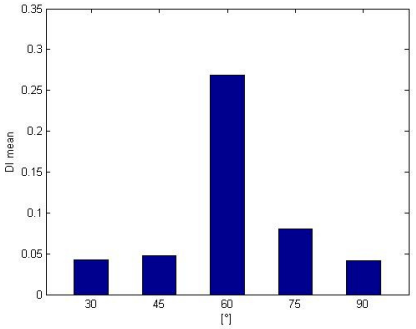

Mean values of DI for the various steering angles

Fig 3.14 - Damage Index evaluation at the various steering angles

We can clearly see, from Fig. 3.14, that we obtained the highest values of ***DI*** for the steering angle 60°, angular position of the crack. We then also measured the distance of the hole using the relation <3.6> and we found a distance of $\boldsymbol{d_{hole}}$ = 248mm, so very close to the correct value $\boldsymbol{s_{hole}}$ = 250mm:

$$\langle 3.6 \rangle \, d_{hole} \simeq \frac{1}{M} \sum_{m=1}^{M} \left(\frac{c}{2 \cdot \Delta t_m^{\text{t-o-f}}} \right)$$

Conclusions

Our analyses demonstrated that a good modeling of both Lamb waves propagation and low velocity impacts events, involving PWAS transducers, can be obtained, through the use of an explicit FEM code (direct analysis in time domain), with a low order technique. Same good results were obtained both on aluminum and composite plates and all the numerical results were validated with experimental data. The damage detection test in an aluminum plate, through the use of the phased array technique, also demonstrated the capability of the employed technique to be used for Structural Health Monitoring testing involving Lamb waves. The great advantage of such a technique is related to the possibility of carrying out accurate studies on the dynamics of the interaction of Lamb waves with the various kinds of damage, such as holes, cracks, delaminations, etc., through the use of a simple, computationally low cost tool.

References

[1] Horace Lamb, "On Waves in an Elastic Plate", Proc. R. Soc. Lond. A 1917 93, 114-128, doi: 10.1098/rspa.1917.0008

[2] Viktorov, I. A. "Rayleigh and Lamb Waves: Physical Theory and Applications", Plenum Press, New York, 1967.

[3] Achenbach, J.D. 1999. "Wave Propagation in Solids", North-Holland.

[4] Joseph L. Rose, "Ultrasonic Waves in Solid Media", Cambridge University Press, 1999.

[5] Victor Giurgiutiu, "Structural health monitoring with piezoelectric wafer active sensors", Academic Press, 2008

[6] B C Lee and W J Staszewski, "Modelling of Lamb waves for damage detection in metallic structures: Part I. Wave propagation", Smart Materials And Structures **12** 804–814, 2003

[7] S. Banerjee et al., "A wave propagation and vibration-based approach for damage identification in structural components", Journal of Sound and Vibration, 2008, doi:10.1016/j.jsv.2008.11.010

[8] Victor Giurgiutiu, "Tuned Lamb Wave Excitation and Detection with Piezoelectric Wafer Active Sensors for Structural Health Monitoring", Journal Of Intelligent Material Systems And Structures, Vol. 16, April 2005

[9] Giurgiutiu and Zagrai, "Characterization of Piezoelectric Wafer Active Sensors", Journal Of Intelligent Material Systems And Structures, Vol. 11 – December 2000

[10] A. H. Meitzler and E. K. Sittig, "Characterization of Piezoelectric Transducers Used in Ultrasonic Devices Operating Above 0.1 GHz", Journal of Applied Physics **40**, 4341 (1969); doi: 10.1063/1.1657196

[11] Mal, A. K., ''Wave Propagation in Layered Composite Laminates Under Periodic Surface Loads'' Wave Motion, **10**, pp. 257–266, 1988.

[12] Mal, A. K., and Lih, S. S., ''Elastodynamic Response of a Unidirectional Composite Laminate to Concentrated Surface Loads, Parts I & II,'' ASME Journal of Applied Mechanics, **55**, pp. 878–892, 1992.

[13] Lih, S. S., and Mal, A. K., ''Response of Multilayered Composite Laminates to Dynamic Surface Loads'', Composites, Part B, 27B, pp. 633–641, 1996.

[14] Guo, D., Mal, A. K., and Ono, K., ''Wave Theory of Acoustic Emission in Composite Laminates,'' Journal of Acoustic Emission, **14**, S19–S46, 1996.

[15] B C Lee and W J Staszewski, "Modelling of Lamb waves for damage detection in metallic structures: Part II. Wave interactions with damage", Smart Materials And Structures, **12** 815–824, 2003

[16] W J Staszewski et al, "Fatigue crack detection in metallic structures with Lamb waves and 3D laser vibrometry", Measurement Science And Technology **18** 727–739, 2007

[17] Z Su et al, "A built-in active sensor network for health monitoring of composite structures", Smart Materials And Structures, **15** 1939–1949, 2006

[18] Wang D et al., "Probability of the presence of damage estimated from an active sensor network in a composite panel of multiple stiffeners", Composites Science and Technology, 2008, doi:10.1016/j.compscitech.2008.11.005

[19] A Raghavan and C E S Cesnik, "Guided-wave signal processing using chirplet matching pursuits and mode correlation for structural health monitoring", Smart Materials And Structures **16** 355–366, 2007

[20] Chang F K, "Smart layer: built-in diagnostics for composite structures", Proceedings of 4th European Conference on Smart Materials and Structures, 1998

[21] Serge Abrate, "Impact on Composite Structures", Cambridge University Press, 1998

[22] Serge Abrate, "Impact on Laminated Composite Materials", Applied Mechanics Reviews, Volume 44, Issue 4, 155 doi:10.1115/1.3119500

[23] P T Coverley and W J Staszewski, "Impact damage location in composite structures using optimized sensor triangulation procedure", Smart Material Structures **12**, 2003 795 doi:10.1088/0964-1726/12/5/017

[24] Richardson and Wisheart, "Review of low-velocity impact properties of composite materials", Composites Part A **27A**, 1996

[25] Hyung Yun Choi and Fu-Kuo Chang, "A Model for Predicting Damage in Graphite/Epoxy Laminated Composites Resulting from Low-Velocity Point Impact", Journal of Composite Materials vol. 26 no. 14 2134-2169, December 1992

[26] H. Hertz, "Über die berührung fester elastischer Körper" (On the contact of rigid elastic solids). J. fur Reine und Angewandte Mathematik, 1982

[27] S Tancredi, F Ricci, E Monaco, L Lecce, S Banerjee, A K Mal "Lamb waves propagation for low velocity impact damages analysis in carbon fibers reinforced plates: experimental and numerical experiences". 5th European Workshop on Structural Health Monitoring, Sorrento 2010.

[28] F. Ricci, E. Monaco, S. Tancredi, S. Banerjee, A. K. Mal "Damage detection techniques in composite structures using ultrasonic guided waves". 8th International Workshop on Structural Health Monitoring Stanford University, Palo Alto 2011.

Acknowledgements

Thanks to my tutor Prof. Ricci and to Eng. Ernesto Monaco for their precious help and support.
Thanks to Chairman of the Ph.D. School Prof. Antonio Moccia for his help and for the possibility he gave me to spend a period at LAMSS (USC, Columbia SC, USA) for my research activities.
Thanks to all the people in my department for their help and human support.
Thanks to all undergraduates and graduates that worked or that are now working at DIAS.
Thanks to Dr. Mal and Dr. Banerjee for their friendship, help and support.
Thanks to Dr. Giurgiutiu and Dr. Yu for accepting me at LAMSS and supporting in everything.
Thanks to all people at LAMSS for their help and "spiritual" support.
Thanks to my family and to all my friends for having accompanied me on this journey.
Thanks to God for having invented Lamb waves.

Appendix: 3-D Costitutive Equations

(a) General Anistropic Material with no plane of material symmetry
According to the generalized Hook's law it is possible to express the 3D constituve equation in the form stress-strain or strain-stress.
The stress-strain equation is given by:

$$\sigma_i = C_{ij} \cdot \varepsilon_j$$

with **i**, **j**=1,2,3,4,5,6 or in matrix for as:

$$\begin{Bmatrix} \sigma_1 \\ \sigma_2 \\ \sigma_3 \\ \tau_4 \\ \tau_5 \\ \tau_6 \end{Bmatrix} = \begin{bmatrix} C_{11} & C_{12} & C_{13} & C_{14} & C_{15} & C_{16} \\ C_{21} & C_{22} & C_{23} & C_{24} & C_{25} & C_{26} \\ C_{31} & C_{32} & C_{33} & C_{34} & C_{35} & C_{36} \\ C_{41} & C_{42} & C_{43} & C_{44} & C_{45} & C_{46} \\ C_{51} & C_{52} & C_{53} & C_{54} & C_{55} & C_{56} \\ C_{61} & C_{62} & C_{63} & C_{64} & C_{65} & C_{66} \end{bmatrix} \cdot \begin{Bmatrix} \varepsilon_1 \\ \varepsilon_2 \\ \varepsilon_3 \\ \gamma_4 \\ \gamma_5 \\ \gamma_6 \end{Bmatrix}$$

With 6x6=36 unknowns. The inverse strain-stress relation is:

$$\varepsilon_i = S_{ij} \cdot \sigma_j$$

with **i**, **j**=1,2,3,4,5,6 or in matrix form as:

$$\begin{Bmatrix} \varepsilon_1 \\ \varepsilon_2 \\ \varepsilon_3 \\ \gamma_4 \\ \gamma_5 \\ \gamma_6 \end{Bmatrix} = \begin{bmatrix} S_{11} & S_{12} & S_{13} & S_{14} & S_{15} & S_{16} \\ S_{21} & S_{22} & S_{23} & S_{24} & S_{25} & S_{26} \\ S_{31} & S_{32} & S_{33} & S_{34} & S_{35} & S_{36} \\ S_{41} & S_{42} & S_{43} & S_{44} & S_{45} & S_{46} \\ S_{51} & S_{52} & S_{53} & S_{54} & S_{55} & S_{56} \\ S_{61} & S_{62} & S_{63} & S_{64} & S_{65} & S_{66} \end{bmatrix} \cdot \begin{Bmatrix} \sigma_1 \\ \sigma_2 \\ \sigma_3 \\ \tau_4 \\ \tau_5 \\ \tau_6 \end{Bmatrix}$$

The matrices **C** and **S** are called Stiffness and Compliance matrix, respectively. This is sometime confusing as, despite their initials, the Compliance matrix is S and the Stiffness matrix is C. It is possible to demonstrate using energetic arguments (i.e. the definition of the strain energy) that both the constitutive matrices **C** and **S** are symmetric, i.e. $\mathbf{C_{ij}=C_{ji}}$ and similarly $\mathbf{S_{ij}=S_{ji}}$.
Because of the symmetry of the $\mathbf{C_{ij}}$ matrix, for a generic anisotropic material the number of unknowns in the constitutive equations is 21 (= 6x7/2).

(b) Specially Orthotropic Materials with 3 mutually perpendicular planes of material symmetry

For this class of materials the constitutive equation can be written as:

$$\begin{Bmatrix}\sigma_1\\ \sigma_2\\ \sigma_3\\ \tau_4\\ \tau_5\\ \tau_6\end{Bmatrix}=\begin{Bmatrix}C_{11} & & & & & \\ C_{21} & C_{22} & & & \text{Symm} & \\ C_{31} & C_{32} & C_{33} & & & \\ 0 & 0 & 0 & C_{44} & & \\ 0 & 0 & 0 & 0 & C_{55} & \\ 0 & 0 & 0 & 0 & 0 & C_{66}\end{Bmatrix}\begin{Bmatrix}\varepsilon_1\\ \varepsilon_2\\ \varepsilon_3\\ \gamma_4\\ \gamma_5\\ \gamma_6\end{Bmatrix}$$

and the number of unknowns is reduced to 9. There are some special features characterizing this type of materials:

1. there is no interaction between normal stresses (σ_1, σ_2, σ_3) and shear strains (γ_4, γ_5, γ_6). Normal stresses acting along principal material directions produce only normal strains;
2. there is no interaction between shear stresses (τ_1, τ_2, τ_3) and normal strains (ε_4, ε_5, ε_6). Shear stresses acting on principal material planes produce only shear strains;
3. there is no interaction between shear stresses and shear strains on different planes. Shear stresses acting on a principal plane produces only a shear strain on that plane;

(c) Transversely Isotropic Material

An orthotropic material is called transversely isotropic when one of its principal plane is a plane of isotropy. At every point on this plane, the mechanical properties are the same in all the directions:

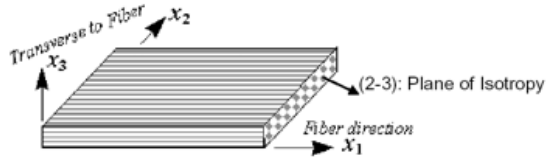

$$\begin{Bmatrix}\sigma_1\\ \sigma_2\\ \sigma_3\\ \tau_4\\ \tau_5\\ \tau_6\end{Bmatrix}=\begin{Bmatrix}C_{11} & & & & & \\ C_{21} & C_{22} & & & \text{Symm} & \\ C_{31} & C_{23} & C_{22} & & & \\ 0 & 0 & 0 & \frac{C_{22}-C_{23}}{2} & & \\ 0 & 0 & 0 & 0 & C_{55} & \\ 0 & 0 & 0 & 0 & 0 & C_{66}\end{Bmatrix}\begin{Bmatrix}\varepsilon_1\\ \varepsilon_2\\ \varepsilon_3\\ \gamma_4\\ \gamma_5\\ \gamma_6\end{Bmatrix}$$

For a transversely isotropic material the number of unknowns in the constitutive equation is 5.

It is worth to note that a unidirectional ply is transversely isotropic. The axis of symmetry, usually denoted as x_1, is the axis parallel to the direction of the fibers, as in the above figure.

Although each lamina is anisotropic, usually orthotropic, some laminates may have isotropic in plane properties and are referenced as transversely isotropic in that plane. Let **n** (n≥3) be the number of plies in the laminate; if the angle between any two adjacent plies is **π/n** the laminate is transversely isotropic in the laminate plane. Example of transversely isotropic are **π/3** and **π/4** laminate with a lay-up:

π/3 laminate → [0°/60°/-60°] **π/4** laminate → [0°/+45°/-45°/90°]

or for symmetric cases

π/3 laminate → $[0°/60°/-60°]_s$ **π/4** laminate → $[0°/+45°/-45°/90°]_s$

The main difference between symmetric and non symmetric laminates is that for the symmetric case the entire laminate behaves with similar features of the case (b), i.e. there is no interaction between in-plane forces and out-of-plane curvature.

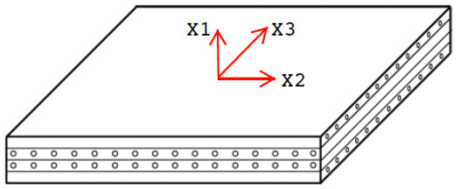

Transversely isotropic materials find several applications in many engineered structures. When defining the coordinate system, the x_1 axis is generally the axis of symmetry (i.e. x_2-x_3 is the plane of isotropy), as in the above figure. Moreover, is it useful to express the coefficient $\mathbf{C_{ij}}$ of the stiffness matrix in terms of the elastic modules. For a transversely isotropic material we have:

$$C_{11}=\frac{1-\nu_{23}\cdot\nu_{32}}{E_2\cdot E_3\cdot\Delta} \qquad C_{12}=\frac{\nu_{21}+\nu_{13}\cdot\nu_{23}}{E_2\cdot E_3\cdot\Delta} \qquad C_{22}=\frac{1-\nu_{13}\cdot\nu_{31}}{E_1\cdot E_3\cdot\Delta} \qquad C_{23}=\frac{\nu_{32}+\nu_{12}\cdot\nu_{31}}{E_1\cdot E_3\cdot\Delta} \qquad C_{33}=\frac{1-\nu_{12}\cdot\nu_{21}}{E_1\cdot E_2\cdot\Delta}$$

$$C_{13}=\frac{\nu_{13}+\nu_{12}\cdot\nu_{23}}{E_1\cdot E_2\cdot\Delta}$$

$$C_{44}=G_{23} \qquad C_{55}=G_{13} \qquad C_{66}=G_{12}$$

where:

$$\Delta=\frac{1}{E_1\cdot E_2\cdot E_3}\begin{vmatrix} 1 & -\nu_{21} & -\nu_{31} \\ -\nu_{12} & 1 & -\nu_{32} \\ -\nu_{13} & -\nu_{23} & 1 \end{vmatrix}$$

Moreover, for a transversely isotropic material we have (x_2- x_3 plane of isotropy):

$$E_2=E_3$$
$$G_{12}=G_{13}$$

$\nu_{12} = \nu_{13}$

$$G_{23} = \frac{E_2}{2 \cdot (1 + \nu_{23})}$$

(d) Isotropic Material

When a material has infinite number of planes of material symmetry through any point, it is referred as isotropic. For this class of materials the constitutive equation can be written as:

$$\begin{Bmatrix} \sigma_1 \\ \sigma_2 \\ \sigma_3 \\ \tau_4 \\ \tau_5 \\ \tau_6 \end{Bmatrix} = \begin{bmatrix} C_{11} & & & & & \\ C_{12} & C_{11} & & & \textit{Symm} & \\ C_{12} & C_{12} & C_{11} & & & \\ 0 & 0 & 0 & \frac{C_{11} - C_{12}}{2} & & \\ 0 & 0 & 0 & 0 & \frac{C_{11} - C_{12}}{2} & \\ 0 & 0 & 0 & 0 & 0 & \frac{C_{11} - C_{12}}{2} \end{bmatrix} \cdot \begin{Bmatrix} \varepsilon_1 \\ \varepsilon_2 \\ \varepsilon_3 \\ \gamma_4 \\ \gamma_5 \\ \gamma_6 \end{Bmatrix}$$

and the number of unknowns is reduced to 2.